TÉCNICO
LISBOA

Radiation environment and its effects on the Martian surface and underground

Pedro Miguel Silva de Magalhães

Thesis to obtain the Master of Science Degree in

Engineering Physics

Supervisors: Prof. Dr. Patrícia Serrano Gonçalves
Dr. Maria Luísa Ferreira da Gama Velho Arruda

Examination Committee

Chairperson: Prof. Dr. Maria Teresa Haderer de la Peña Stadler
Supervisor: Prof. Dr. Patrícia Carla Serrano Gonçalves
Members of the Committee: Prof. Dr. Jorge Miguel Brito Almeida Sampaio
Prof. Dr. Pedro Jorge dos Santos Assis

April 2016

Acknowledgments

Firstly, I would like to thank my supervisor, Prof. Dr. Patrícia Gonçalves and my co-supervisor, Dr. Luísa Arruda, for their guidance in the development of this work and their availability.

Getting through my dissertation required more than just academic support, and I have many people to thank for, having to tolerate me over these past months, for I know sometimes I'm not easy to deal with. I cannot begin to express my gratitude and appreciation towards my friends, for their true friendship. If it were not for all those crazy laughters and a few tragedies along the way, I would not be the person I evolved into. I will be forever grateful to my family, namely my parents and my little brother, without whom I would never be able to study and reach where I am now.

I know that my namesake Grandfather, altough existing only inside my heart, is and will be forever proud of me. I just know!

Resumo

Esta tese de mestrado consiste na análise do ambiente de radiação em Marte, na superfície e a várias profundidades no solo, de forma a estudar as implicações para formação e evolução de vida, nomeadamente a possibilidade de existência e ou sobrevivência de micro-organismos no seu subsolo.
Apesar de ser um planeta rochoso, marte tem uma atmosfera e, mais importante ainda, água, que torna o estudo em vigor ainda mais interessante.
O conjunto de simulações ocorreram num ambiente semelhante à Cratera de Gale, sítio onde o Curiosity aterrou a 7 de agosto de 2012. Resultante destas simulações, são calculados e apresentados a transferência linear de energia e o fluxo de partículas geradas em função da energia a diferentes profundidades, tanto para radiação cósmica galáctica (protões e alfas), como para partículas solares energéticas. Tudo isto em dois níveis de atividade solar distintos, no mínimo e no máximo. As simulações foram feitas usando o dMEREM, modelo detalhado do ambiente de radiação energética, desenvolvido no LIP. Esta tese levou à evolução do dMEREM no sentido de ser possível simular ambientes de radiação não só à superfície, mas também a diferentes profundidades no solo Marciano. O modelo é baseado em Geant4 (Geometry and Tracking), que é uma ferramenta que permite a simulação da passagem e respetiva interação de partículas pela matéria, desenvolvido no CERN.

Palavras-chave: GCR, SEP, LET, dMEREM, ADN, Marte

Abstract

This master's thesis consists of the analysis of Mars' radiation environment at its surface and at different soil depths, in order to evaluate the implications for the formation and evolution of life, namely, the possibility of the existence or survival of microorganisms at its subsoil.

In spite of being a rocky planet, Mars has an atmosphere and, more important than that, it has water, which makes it interesting for the current study.

This simulation framework will take place at the Gale Crater, site where Curiosity landed at August 7th, 2012. As a result, the Linear Energy Transfer and the particles' flux as a function of energy is calculated at different soil depths, for GCR (protons and α particles) and for SEP. Both are simulated on two different solar activity levels, on a minimum and on a maximum. This is achieved using dMEREM, a detailed Mars Energetic Radiation Environment Model, developed at LIP. This thesis expanded dMEREM, since it made possible the simulation of the radiation environment not only at the surface, but also at different depths into the Martian soil. It is a Geant4 (Geometry and Tracking) based model, which is a toolkit for simulating the passage of particles through matter, developed at CERN.

Keywords: GCR, SEP, LET, dMEREM, DNA, Mars

Contents

List of Tables

List of Figures

Nomenclature

Abbreviation	Definition
α radiation	alpha radiation
γ radiation	gamma radiation
ADE	Ambient Dose Equivalent
BER	Base-excision repair
dMEREM	detailed Mars Energetic Radiation Environment Model
DNA	Deoxyribonucleic acid
DSB	Double-strand break
eMEREM	engineering Mars Energetic Radiation Environment Model
ESA	European Space Agency
FLUKA	Fluktuierende Kaskade
Geant	Geometry and Tracking
GCR	Galactic Cosmic Radiation
HEP	High energy physics
HR	Homologous recombination
HZE ion	High-charge/high-energy ion
ICRU	International Commission on Radiation Units & Measurements
IST	Instituto Superior Técnico
LET	Linear Energy Transfer
LIP	Laboratório de Instrumentação e Física Experimental de Partículas
MSL	Mars Science Laboratory
MarsREM	Mars Energetic Radiation Environment Model
NASA	National Aeronautics and Space Administration
NHEJ	Non-homologous end joining
RAD	Radiation Assessment Detector
RBE	Relative Biological Effectiveness
ROS	Reactive oxygen species
SEP	Solar Energetic Particles
SPENVIS	Space Environment, Effects, and Education System
SSB	Single-strand break

Chapter I

Introduction and Motivation

I.1 Motivation

Astrobiology is the study of the origin, evolution, distribution and future of life in the universe [1], incorporating the pursuit of habitable environments either within our Solar System or outside. Therefore, the study of Mars' radiation environment and exploitation of the possibility of life under such conditions appears as a natural topic for this Master thesis since it is a direct application of this branch of Physics to a mission that is still being planned and evaluated to our nearest neighbour planet.

Since a long time ago, human civilization dreams about making a journey to Mars, both for gradual exploitation of the Solar system and to defy the human limits. Among all the discoveries that humankind made from this planet, there is one that excels, which is the presence of liquid water that may still be conserved. Water is vital to life as we know it, so if there is water, the likelihood that Mars has or had life on its surface or subsurface is quite strong! The work in this thesis includes the simulation and study of the radiation environment, both at the surface and at different depths of the subsurface, in order to analyze the implications for the formation and evolution of life. This was achieved using Geant4, which stands for Geometry and Tracking, and it is a toolkit for simulating the passage of particles through matter, using Monte Carlo methods and developed at CERN, which is freely available from the project web site [2]. An example of a result of the outcome of a simulation is depicted at Figure I.1. So the continuous development of simulation tools, namely to predict the radiation field in both free space and on planetary surfaces, is extremely important for the planning of a manned mission to Mars, and to other planets as well.

Mars Exploration Program is a NASA program which aims to discover if Mars is potentially a habitable planet and to study the geophysical processes that were responsible for its formation and evolution to the planet as it is now. Curiosity is the largest planetary rover ever sent to Mars, with a mass of approximately 900 kg, 2.9m by 2.7m and 2.2m tall, is part of NASA's Mars Science Laboratory mission [4]. It all began at August 7th, 2012, when the Curiosity rover landed on Mars at the Gale Crater site .[1] This was the first day in the history of mankind that measurements of cosmic rays and solar energetic

[1] a Crater on Mars, located at the Northwestern part of the Aeolis quadrangle at 5.4°S 137.8°E [5].

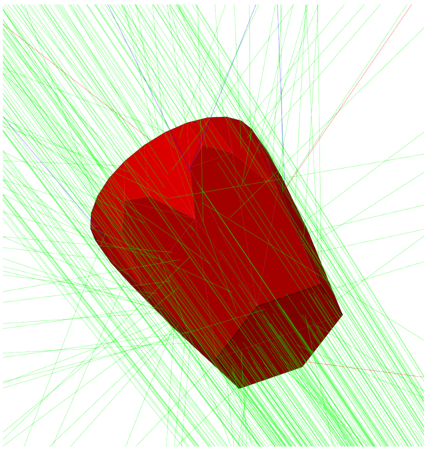

Figure I.1: Visualization of a simulation performed using GEANT4, where the red object is a detector and the lines denote the trajectory of positive (blue), negative (red) and neutral (green) particles. [3]

particles at Mars' surface took place. These measurements occurred over 300 days during the maximum solar activity, not only at Mars' surface, but also during the ship's trip from Earth, with the Mars Science laboratory installed in its the interior.

The European Space Agency (ESA) has established the ExoMars programme, which aims to investigate for past and present life, searching for biosignatures, such as the presence of methane, as well as other trace atmospheric gases that could be signatures of active [6]. It is scheduled to arrive at Mars on October, 2016, and consists of a Trace Gas Orbiter (TGO), responsible for the detection of the biosignatures, and also by an entry, descent and landing demonstrator module, which basically aids the landing of this apparatus, since the execution of the entry, descent and landing sequence may become somewhat complicated, for it will enter the Martian atmosphere at 21 000 km/h [7].

I.2 Mars

I.2.1 Radiation in Mars

Due to the increasing interest in the operation of equipment on Mars, driven by the will to send crewed missions there, the study and comprehension of the interplanetary radiation environment and its effects, not only on crews during the duration of the mission, but also on the equipment, is crucial.

The radiation environment in space is a complex mixture of energetic charged particles that poses a major health concern for astronauts on long-duration missions. The space radiation environment consists of three broad categories (National Council on Radiation Protection and Measurements, 1989, 2000), which are trapped particle radiation, solar particle radiation and galactic cosmic radiation (GCR), with protons being the most abundant particle type.

Since Mars lacks a global magnetic field, its radiation environment is mostly constituted by both Galactic Cosmic Rays and Solar Energetic Particles, which affect the evolution of the climate of Mars, the operation of satellites, and the human exploration of the planet [8].

GCR

According to the ICRU (International Commission on Radiation Units & Measurements), cosmic radiation is the ionizing radiation consisting of high energetic particles, primarily nuclei of extraterrestrial origin, and the particles they generate due to their interaction with an atmosphere and other crossed matter [9]. These nuclei are originated mostly within our galaxy, but outside our solar system. It is important to note that this radiation, while entering Mars' atmosphere, produces secondary particles, even though its density is approximately 1% of the Earth's atmosphere. So, taken into account its origin, it is natural to comprehend that it is essentially an isotropic radiation, since Mars lacks a global magnetic field. Although every natural chemical element is part of this radiation, around 87% are protons and roughly 12% are alpha particles. These particles are predominantly accelerated in the Milky Way. At very high energies, the particles are actually assumed to be originated from powerful astrophysical accelerators, such as supernova explosions or quasars, located outside of the Milky Way [10].
Figure I.2 shows at a more detailed level the elements' relative abundance in GCR and in the Solar system [11].

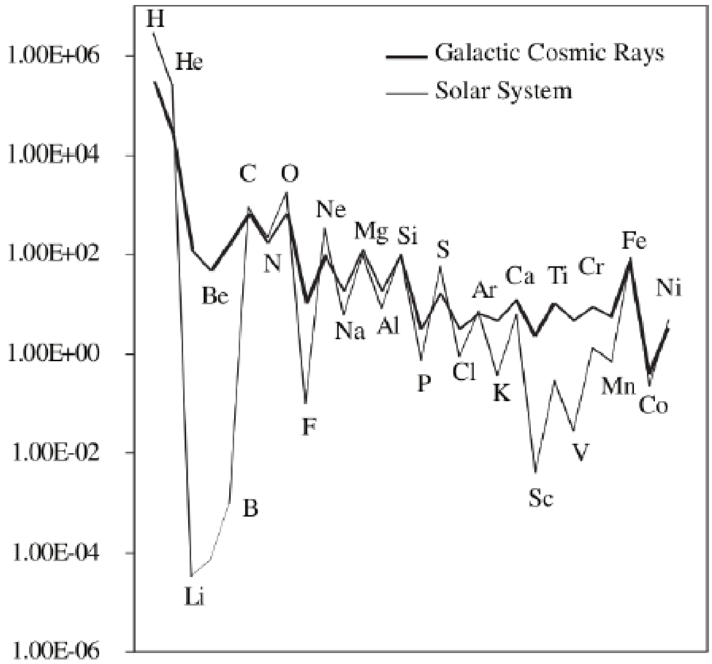

Figure I.2: Relative abundance of elements in galactic cosmic rays and in the solar system.

Their flux is influenced by the background level of solar activity, thus having seasonal effects. At higher solar activity level, lower energy particles from the incident radiation will be removed, due to the complex interplanetary magnetic fields [12], thus decreasing its flux. This effect is known as solar modulation effect and it can be seen in Figure I.3, which shows the GCR differential flux spectrum at solar activity minimum (a) and maximum (b) at the Solar Cycle 23 for hydrogen, helium, lithium and iron [13].

For energies higher than 1 GeV, the solar modulation effect is not quite relevant. Although cosmic rays' energy may reach values up to 10^{20} eV, as can be seen in Figure I.4(a), most of its hazardous effects

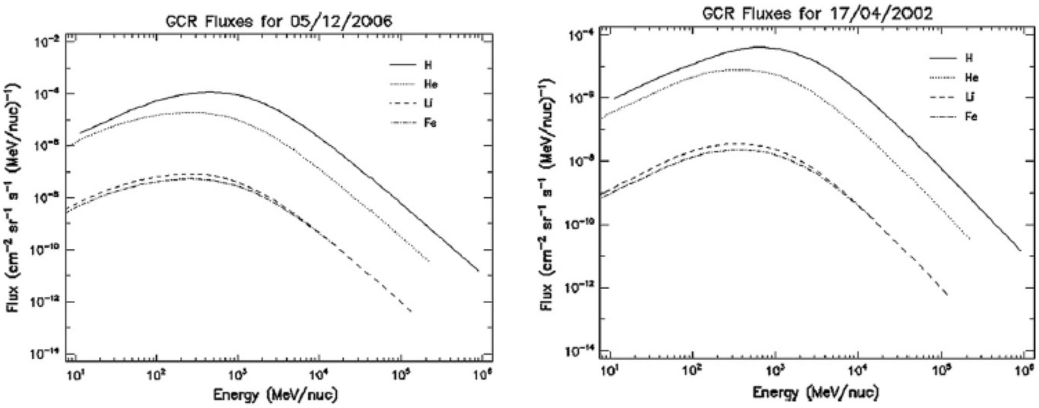

(a) (b)

Figure I.3: Differential GCR flux spectrum as a function of energy at solar minimum (a) and solar maximum (b) for solar cycle 23.

are associated within the range of nuclei with energies between several hundred MeV and a few GeV (Guetersloh et al., 2011), since the flux decreases exponentially with energy (note that both axis are in logarithmic scale) .

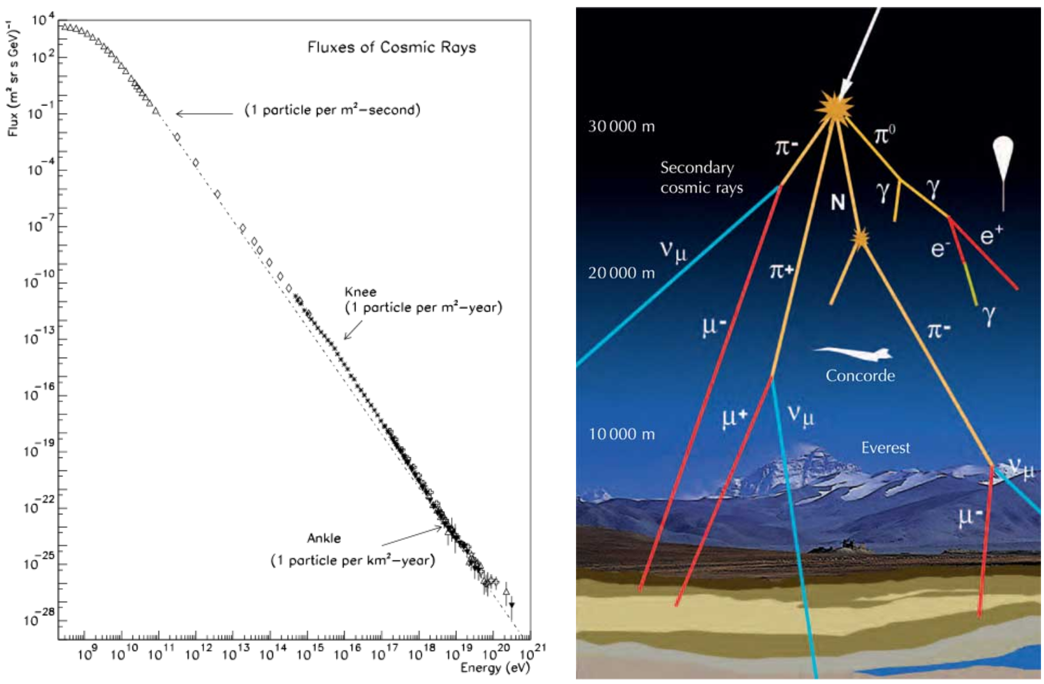

(a) (b)

Figure I.4: GCR energy spectrum (a) and a sketch of a cascade produced by an incident cosmic particle within the Earth's atmosphere (b).

Because of their high energies, GCR are difficult to shield against and can penetrate a few meters into the Martian soil [14]. Figure I.4(b) shows a diagram illustrating the cascade of secondary particles produced within the Earth's atmosphere, consequence of a primary particle interaction with the medium. This happens with quite frequency at Mars, not only at its atmosphere, but mainly at the soil, which will be explored further in this Thesis. These interactions between particles and atmosphere produce a large amount of secondary particles, which themselves may also produce further cascades of extra secondary particles, giving rise to a high particle flux, which increases with depth until a maximum is reached, known as the Pfotzer Maximum [15], after which, particles will have insufficient energy left to produce new secondary particles, causing a decrease of the flux. On the Earth, this maximum is reached at the atmosphere, at an altitude of approximately 15 km. However, on Mars, since the atmosphere is around 1% of ours, the Pfotzer Maximum occurs below the surface. This means that the first centimeters of its soil are probably even more inhospitable than the surface.

SEP

The first detection of solar particles belongs to Forbush, in 1946, which led to the term ‘solar cosmic rays’. It started due to the increase in the cosmic ray intensity measured with ionization chambers on February 28th and March 7th, 1946, as can be seen in Figure I.5 [16]. Initially, Lange and Forbush

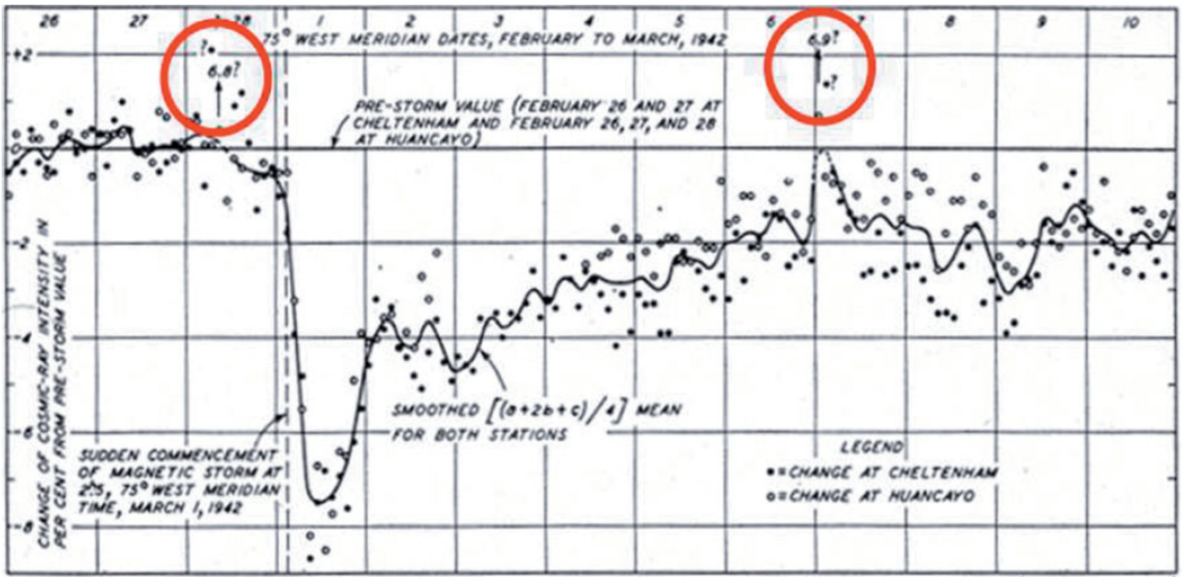

Figure I.5: Sketch of the cosmic radiation intensity between February 26th and March 10th, 1946.

thought that these uncommon increases (of around 7%) were due to magnetic effects of a ring current on GCR trajectories. It was only at July 25th of the same year, when another event was observed, that Forbush linked these 3 odd events to solar flares. A few months later he wrote a paper marking the official birth of the field of SEP physics. Solar flares and coronal mass ejections are the source of these particles, existing a correlation between the flux of these particles and the solar activity, namely the occurrence of a solar eruption. They are mostly composed of protons, with the remaining being around 10% He and less than 1% heavier elements [12], and can be highly accelerated, having energies up to some GeV per nucleon. The detection of solar neutrons is quite rare, since their half life time is around 11.7 minutes, so most of them already decayed before reaching Mars’ and Earth’s surface.

SEP events are sporadic and their flux may vary by several orders of magnitude, hence difficult to predict, with durations that spans from a few hours to days. SEP with energy higher than 10 MeV per nucleon are considered hazardous to personnel involved in extravehicular activity at the surface of Mars [12]. Protons, regardless of being GCR or SEP descendant, with a kinetic energy less than $\simeq$ 150 MeV shall

not be able to reach the surface, assuming an atmospheric depth column of 20g/cm^{-2} [14].
There are some effects that are important in respect to SEP events at Mars, namely the existence of a shadowing of the planet, cutting approximately half of the SEP primary particle flux. The second is the attenuation of SEP flux due to Mars' atmosphere, shielding primary particles of relatively low energies, and last but not least, these particles interact with the Martian soil creating many secondary particles, mostly neutrons, contributing to the deposited dose rates.

I.2.2 Martian atmosphere

The Martian atmosphere is mostly (around 96%) composed of carbon dioxide (CO_2) and has many trace gases, such as water, methane (CH_4) and potentially sulphur dioxide (SO_2) and nitrous oxide (N_2O). It may contain many more which remain undetected due to their low concentrations. The detection of trace gases would not only provide a good understanding about the chemistry of Mars' atmosphere, but would also serve as indirect tracers of geological and biological activity [17].
The atmospheric pressure on Mars' surface at mean radius is around 626 Pa, which is about 0.6% of Earth's atmospheric pressure at the mean sea level, with a scale height of 11.1 km and a total mass of approximately 2.5×10^{26} kg, having a density of 20 gm^{-3} [18].
At August 7th, 2012, the first day in history when humankind actually measured GCR and SEP fluxes at the surface of Mars [19], dose rates were measured, varying between 180 and 225 μGy/day, which is shown in Figure I.6. This variation is not only due to seasonal changes at Gale Crater, but also to the variation of the atmospheric pressure. Figure I.7 shows the anti-correlation between the dose rate and atmospheric pressure, which is related to the mass of atmosphere above the ground.

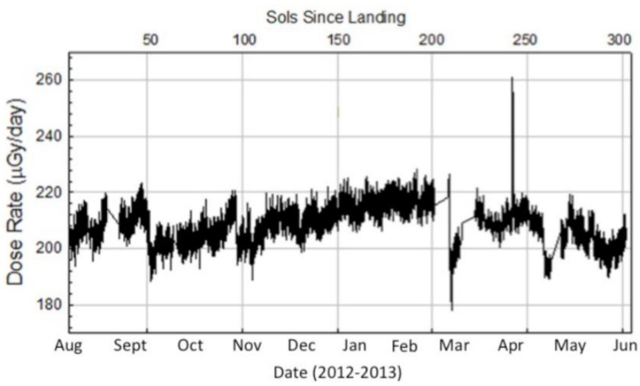

Figure I.6: Radiation dose during the first 300 sols on the Martian surface near the maximum of Solar Cycle 24.

There is also a variation of the dose rate during the day, which happens due to the existence of temperature gradients at the atmosphere, caused by the solar heating, giving rise to thermal tides, ultimately causing a variation in the atmospheric mass distribution. This effect is shown in Figure I.8, where the ups and downs of the dose rate are notoriously registered. When a GCR interacts with an atmospheric nucleus, nucleons, gamma radiation and energetic mesons are produced (red Dartnell, Modelling), where the decay time of the latter is short, producing muons gamma rays and electrons. Hence the air shower will have a large component of electromagnetic cascades.

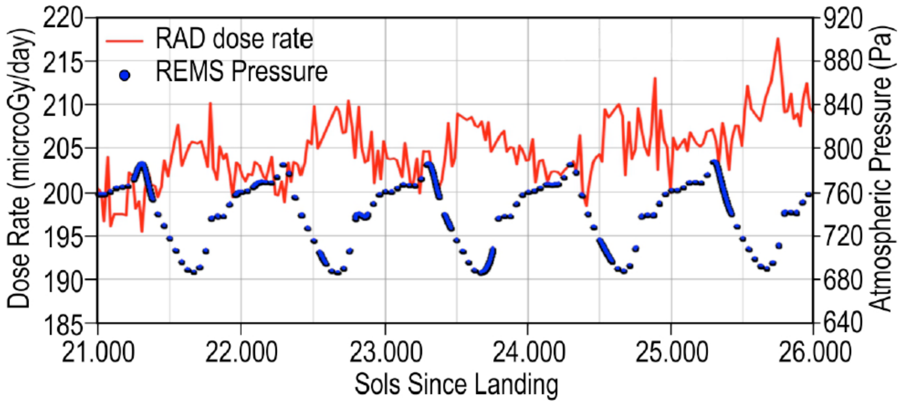

Figure I.7: Dose rate and atmospheric pressure, both plotted along 5 sols.

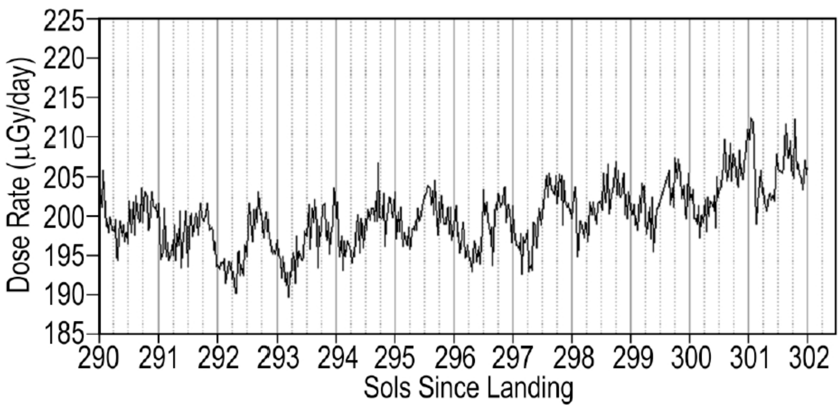

Figure I.8: Plot showing the variation in dose rate during a sol.

I.2.3 Martian soil

The Martian soil composition is an important aspect to take into account, since the interaction of radiation with the soil will logically depend on the existing elements. So, when evaluating the albedo radiation from the Martian surface, which is the reflected radiation, one must consider its composition. In our Solar System two kinds of surface composition are dominant, namely a silicatic rocky composition of the inner planets (from Mercury to Mars), and an icy composition of the outer planets, from Jupiter to Pluto. Neutron backscattering is far more important to be taken into account in a planet with a silicatic soil than a planet with an icy soil [20].

The Mars Odyssey spacecraft went into orbit on October 24th, 2001. One of its main goals was to analyze the elemental composition of the Martian soil, using a germanium gamma-ray spectrometer [21]. Figure I.9 shows the detected spectrum, resulting from an accumulation of 39.5 h. Some lines occur at well-known gamma ray energies, namely from standard radioactive sources (^{60}Co peaks of 1.1732 MeV and 1.3325 MeV, for example) or from the decay chains of the natural radioactive isotopes: ^{40}K, ^{232}Th and ^{238}U. On Mars, several secondary particles are created, namely neutrons. The reaction responsible for their production, as well as some other particles, which arises from the interaction of the cosmic rays with the nuclei of the atmosphere, is spallation [22]. A fast neutron (kinetic energy above 20 MeV) loses its energy mostly through elastic scatterings, where it will be slowing down. Remember that in an elastic scattering collision between a particle and a nucleus, the energy lost by the former corresponds to the

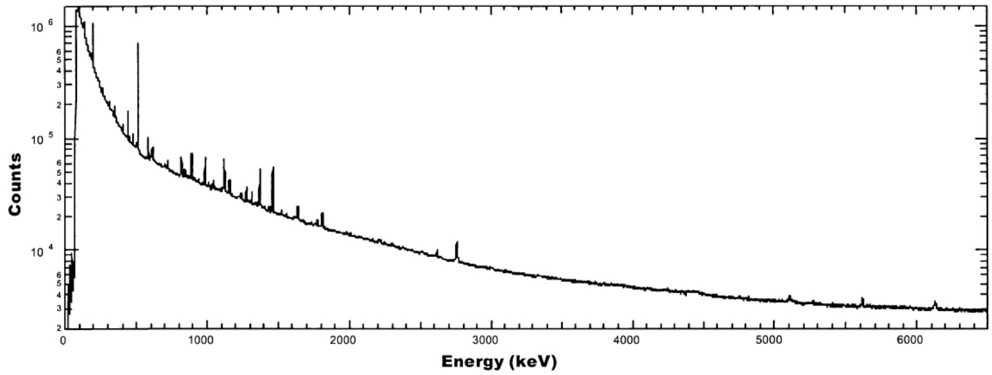

Figure I.9: Mars Odyssey cruise spectrum.

kinetic energy of the nucleus' recoil, contrasting with an inelastic collision where the nucleus absorbs part of the particle's energy and is left in an excited state, which causes it to emit some kind of radiation to bring it back down to a stable or ground state. As the neutron loses its energy, it will undergo several random elastic collisions, increasing the probability of it to be captured. Hydrogen is widely used in Earth to 'cool down' energetic neutrons created in reactors, due to the increased cross section of interaction. Hence, on Mars, hydrogen is associated with water, therefore regions with larger content of water in the soil are associated with lower fluxes of energetic neutrons, and, correspondingly, higher flux of thermal neutrons. Figure I.10 shows a map of the weight percentage of water in the Martian soil, computed by the results measured by a GRS [23]. The Neutron Spectrometers on GRS directly detect scattered neutrons, and the Gamma Sensor detects the gamma rays. This neutron die-away technique has been used in the oil and gas exploration industry since the decade of 1960.[24]

The soil composition used in this thesis is presented in table II.1, at chapter II, where bulk is a mixture

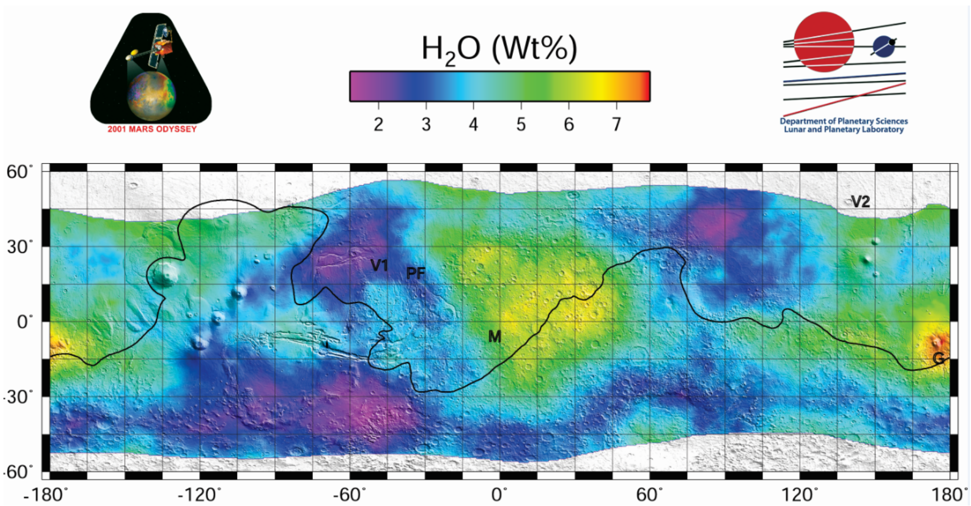

Figure I.10: Percentage of water in the Martian soil, measured by a GRS [23].

of Al_2MgCa, Na_2 and K_2O_3. To be more complete, this thesis' work should contain other soil types. Instead, this soil composition was chosen, since it came from *in situ* measurements by the Curiosity rover, in Gale Crater.

I.2.4 Phobos & Deimos

Mars has two moons, Phobos and Deimos, discovered in 1877 by Asaph Hall and are named after the Greek characters with the same name. Both are twins and sons of Ares, God of War, where, in the Greek mythology, the former is the personification of Fear and the latter is the personification of Panic. The

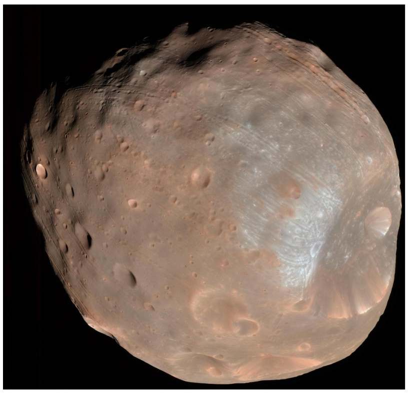

(a) Phobos

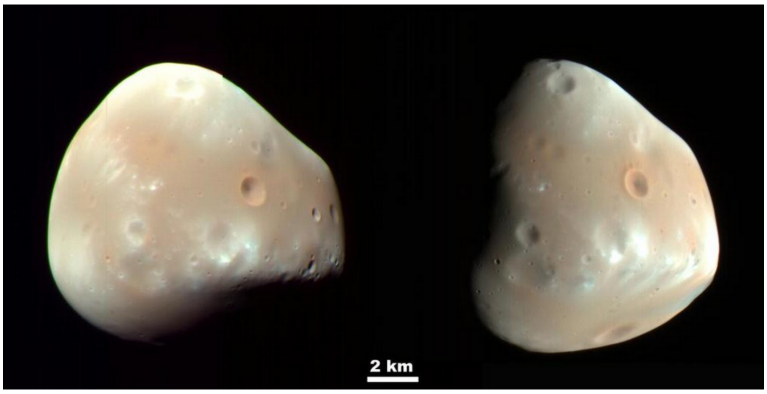

(b) Deimos

Figure I.11: Phobos and Deimos pictures taken by the High Resolution Imaging Science Experiment (HiRISE) camera on NASA's Mars Reconnaissance Orbiter.

characteristics of these two moons are shown in table I.1, Phobos being the larger one, almost double of Deimos' size, and the closer one in respect to the Martian surface, revolves around Mars three times one Martian day. The moons appear to have surface materials similar to many asteroids in the outer asteroid belt, which leads most scientists to believe that Phobos and Deimos are captured asteroids, and both are considered to be about 2 billion years old [25].

Table I.1: Phobos & Deimos.

	Phobos	Deimos
Mean distance from Mars (km)	9377	23436
Orbital period (Mars days)	0.32	1.26
Major axis (km)	26	16
Minor axis (km)	18	10
Mass ($\times 10^{15}$kg)	10.8	1.8
Mean density(gcm^{-3})	1.90	1.75

Due to their relatively low density and high porosity, they may hold a large amount of ice, being a potential resource to be explored [26].

I.3 Radiation quantities and effects

Since the risks associated with radiation exposure cannot be measured directly, what is really measured is the dose. Radiation dosimetry deals with a quantitative estimation of energy deposited in a given medium by radiation, whether it is directly or indirectly ionizing. Some quantities have been defined, whereas the most commonly used ones are described in this section.

I.3.1 Flux

Flux is a rather simple concept throughout physics and mathematics describing the flow of a physical property in space. The word flux comes from the Latin *fluxus* which means flow. Thus, particle flux is the rate which a number of particles cross a given area, so its IS unit is $m^{-2}s^{-1}$.

I.3.2 Fluence

The particle fluence is the flux integrated in time, where this time corresponds to an interval of interest. For example, the duration of a space ship travelling from Earth to Mars, giving the total number of particles per unit of area that have crossed the sip. The IS unit of fluence is then m^{-2}. In the computation, since a perpendicular area in respect to the incident beam is considered, this quantity is independent of the incident angle. The planar particle fluence is the number of particles that crosses a plane per unit area, henceforth depending on the particle's angle of incidence.

I.3.3 Absorbed, equivalent and effective dose

The unit of absorbed dose is Grey, which corresponds to 1 Joule of radiation absorbed by 1 kilogram of a given material, measuring the loss of radiation in a tissue, for example. This may be a two stepped process, since indirectly ionizing radiation is also taken into account, where, at a first step, this radiation transfers kinetic energy to secondary charged particles, and at the second step, these charged particles transfer some of their energy to the medium.
However, this quantity does not take into account that each kind of radiation has a different impact on human tissue, meaning that two different types of radiation may cause a completely different impact. Gamma radiation is weakly ionizing, contrasting with protons or high-charge/high-energy (HZE) ions, which are highly ionizing and deposit their energy in a dense track, leading to clusters of multiple breaks in the DNA molecule, hence hazardous to cellular survival [27]. This is why equivalent dose is used, for this quantity already takes into account each type of radiation, assigning each one of them with a weighting factor, and the unit is now Sievert, Sv, which is still energy per unit mass. So basically, the equivalent dose is the absorbed dose multiplied by the respective weighting factor, summed over all types of radiation:

$$H_T = \sum_R \omega_R D_{T:R} \tag{I.1}$$

For example, the weighting factor of γ-radiation is 1 and for α-particles it is 20. Which means that for an absorbed dose of 1 Gy, the equivalent dose for the former is 1 Sv and for the latter it is 20 Sv. An example of some particle weighting factors are shown in the table I.2 [28].

This factor for neutrons has not remained the same. According to ICRP Publ. 103 a new set of radiation weighting factors was set, which is shown in equation I.2.

Table I.2: Examples of radiation weighting factors.

Radiation type	Radiation weighting factor (ω_R)
Photons	1
Electrons & muons	1
Protons & charged pions	2
α particles, fission fragments and heavy ions	20
Neutrons	Continuous energy-dependant fuction from 2.5 to 20

$$\omega_R = \begin{cases} 2.5 + 18.2 \exp^{-[\ln(E_n)]^2/6} & E_n < 1 \text{ MeV} \\ 5 + 17 \exp^{-[\ln(2E_n)]^2/6} & 1 \text{ MeV} \leq E_n \leq 50 \text{ MeV} \\ 2.5 + 3.25 \exp^{-[\ln(0.04E_n)]^2/6} & E_n > 50 \text{ MeV} \end{cases} \tag{I.2}$$

Now one may argue that each tissue of the human body has different sensibility and resistance to radiation. This is rectified by the effective dose, where a weighting factor is now allocated to each tissue. It is trivial to understand that this is computed by multiplying the equivalent dose by the respective tissue weighting factor, summed over all tissues I.3.

$$ED = \sum_T \omega_T H_T \tag{I.3}$$

where all these tissue weighting factors are normalized (equation I.4). An example of the weighting factors of some organs are shown in the table I.3 [29].

Table I.3: Examples of tissue weighting factors.

Tissue	Tissue weighting factor (ω_T)	Sum of ω_T values
Bone marrow (red), colon, lung, stomach, breast, other †	0.12	0.72
Gonads & muons	0.08	0.08
Bladder, oesophagus, liver, thyroid	0.04	0.16
Bone surface, brain, salivary glands, skin	0.01	0.04
Total	-	1.00

†Adrenals, extra thoracic region, gall bladder, heart, kidneys, lymphatic nodes, muscle, oral mucosa, pancreas, prostate (♂), small intestine, spleen, thymus, uterus/cervix (♀).

$$\sum_T \omega_T = 1 \tag{I.4}$$

Figure I.12 is a set of charts showing the relative contributions of different particles to the absorbed dose and dose equivalent, in the case of GCR and SEP, with a polythene shielding of 1 gcm^{-2} for exposure at the eye [30].

Figure I.13 gives more insight about the order of magnitude of these radiation doses, comparing them to familiar radiation exposures, such as a CT scan, on a logarithmic scale. We see that there is a factor of a 100 between the average annual cosmic radiation at sea level and a 180-day transit to Mars, but only a factor of $\simeq 4$ between the latter and an ordinary CT scan.

It is relevant to note that the time duration at which these doses are absorbed by our tissues is also a

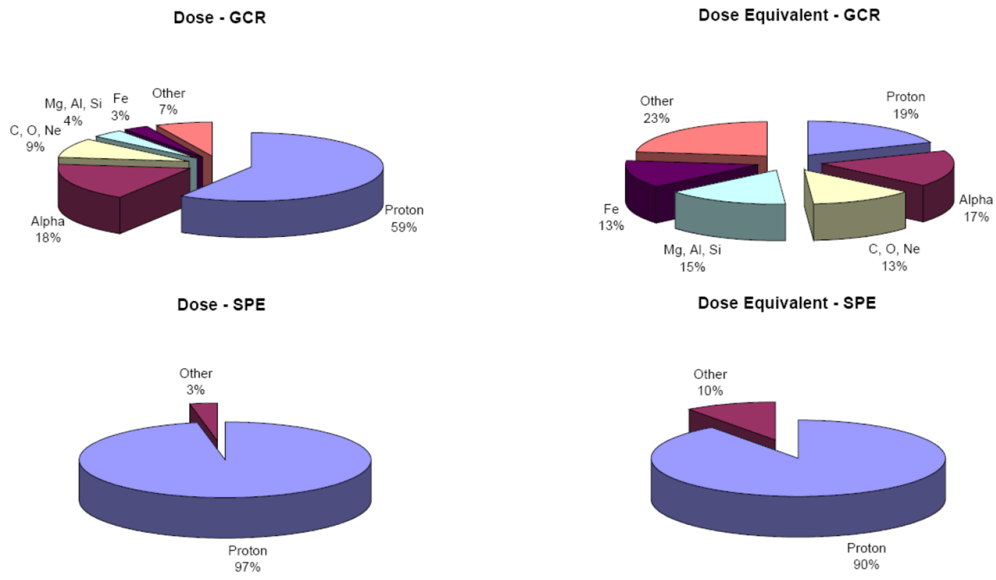

Figure I.12: Relative contributions of different particles to the absorbed dose and dose equivalent.

factor to be taken into account, for the shorter the exposure time for the same absorbed dose, the more hazardous it shall be to our body.

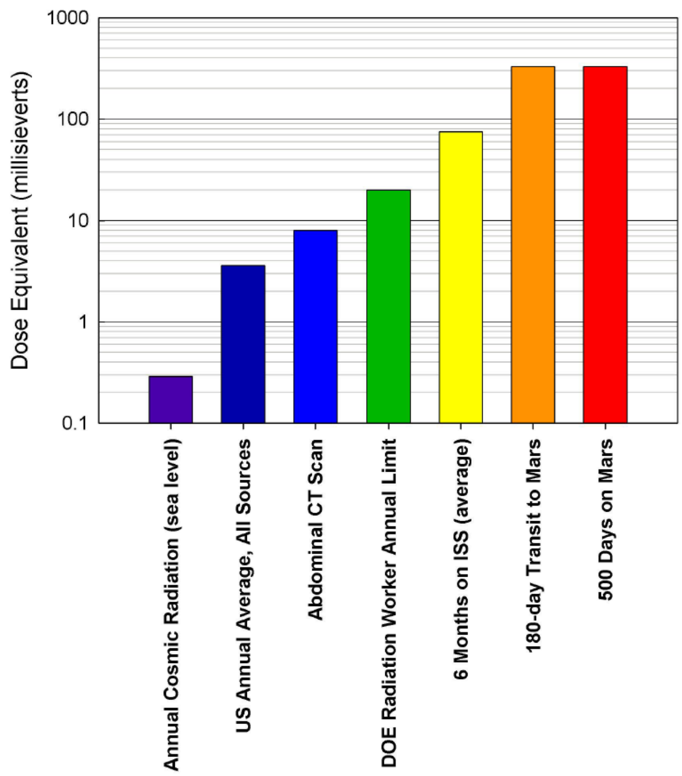

Figure I.13: Order of magnitude of radiation doses in different daily basis scenarios.

I.3.4 Ambient dose equivalent

The ambient dose equivalent H*(10) at a given position in a radiation field is the dose equivalent which would be generated in the associated oriented and expanded radiation field at a depth of 10 mm of the

ICRU sphere which is oriented opposite to the direction of the incident radiation [31]. Since determining effective dose requires knowing the doses delivered to all the major organs in the body, it is not a practical dose quantity to attempt to evaluate. Instead, alternate quantities have been devised such the ambient dose equivalent that is used in instrumental measurements, being useful since it is simpler to measure or calculate because it avoids the complexities associated with phantoms or patient anatomy [32].

I.3.5 RAD's Dose measurements

The Radiation Assessment Detector (RAD) was incorporated in the Curiosity with the purpose of measuring high energy radiation on the Martian surface, including not only radiation from space, but also secondary radiation due to the interaction of the primary radiation with the Martian atmosphere and surface [33]. Table I.4 shows the GCR dose rate and dose equivalent rate, and the SEP dose and equivalent dose measured bot during the Mars Science Laboratory (MSL) cruise and during approximately 300 days at the surface, where the SEP doses are per event since a poor statistics was obtained, for only 5 events were observed during the cruise and only 1 was at the surface. Table I.5 shows the GCR dose and

	GCR Dose Rate (mGy/day)	**GCR Dose Equiv. Rate (mSv/day)**	**SEP Dose (mGy/event)**	**SEP Dose Equivalent (mSv/event)**
MSL Cruise (Zeitlin et al. 2013) (22)	0.464	1.84	1.2-19.5[a]	1.2-19.5
Mars Surface	0.210	0.64	0.025[b]	0.025

Table I.4: Measurements of the RAD's GCR and SEP dose and dose rates both during the MSL cruise and at the Martian surface.

dose equivalent rates measurements, which correspond to state of the art dose knowledge of the Martian surface. With the knowledge of these dose rates, it is now possible to predict more accurately the doses inside the soil, which is also presented at the table.

Depth below Surface	**Effective Shielding mass (g/cm^2)**	**GCR Dose Rate (mGy/yr)**	**GCR Dose Equiv. Rate (mSv/yr)**
Mars Surface (RAD)	0	76	232
-10 cm	28	96	295
-1 m	280	36.4	81
-2 m	560	8.7	15
-3 m	840	1.8	2.9

Table I.5: Measurements of the RAD's GCR dose and estimation at four different depths of the Martian soil.

I.3.6 Linear Energy Transfer

The linear energy transfer, LET, is defined as the energy deposited by an ionizing particle in matter per unit length of its trajectory (dE/dx), so it is measured in J/m. Division by the absorbing medium's density allows the LET to be density-independent, so the LET profile does not change much from medium to medium. There are two types of linear energy transfer: collision and radiative. The former outcomes from the interaction of the incident radiation with the atomic orbital electrons of the medium, while the latter results from the interaction of charged particles with the atomic nuclei, causing them to change their direction and acceleration. These particles will then, in this latter situation, radiate *Bremsstrahlung* photons.

The energy losses by a charged particle while interacting with the medium, where quantum mechanics is taken into account, was firstly computed by Bethe and Bloch (1932) (eq I.5):

$$-\frac{1}{\rho}\frac{dE}{dx} = kz^2\frac{Z}{A}\frac{1}{\beta^2}\left[\log\left(\frac{2m_ec^2\beta^2\gamma^2T_{max}}{I^2}\right) - 2\beta^2 - \delta - 2\frac{C}{Z} + zL_1 + z^2L_2\right] \mathrm{MeV/(g/cm^2)} \qquad \text{(I.5)}$$

where $k = 2\pi N_A r_e^2 m_e c^2 = 0.1535$ MeV/(g/cm^2), $r_e = 2.817 \times 10^{-13}$ cm is the classical electron radius, $m_e = 0.511$ MeV/c^2, $N_A = 6.023 \times 10^{23}$, ρ is the density of the material, z is the charge of the incident particle, Z is the atomic number of the material, A is the material's mass number, I is the mean excitation energy, which is a mean value of all ionization potentials of an atom of the absorbing material, $\beta = \frac{v}{c}$ is the particle's velocity, $\gamma = \frac{1}{\sqrt{1-\beta^2}}$ is the Lorentz factor, δ is the density correction, accounting for the reduction of the Coulomb Force exerted on a fast charged particle by distant atoms as a result of the polarization of the medium, and T_{max} is the maximum energy transferred in the collision, which for $M \gg m_e$ we have $T_{max} \sim 2m_ec^2\beta^2\gamma^2$.

Stopping power for positive muons in copper is plotted in Figure I.14 as a function of $\beta\gamma = \frac{p}{Mc}$ [34].

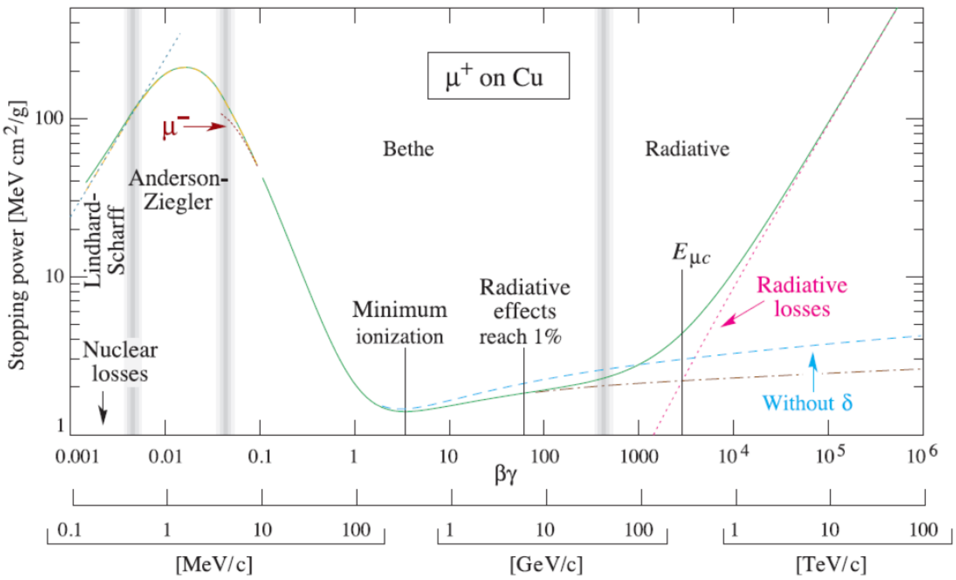

Figure I.14: Stopping power for positive muons on copper.

The first two regions ($\beta\gamma < 0.05$) are not described by the Bethe-Bloch formula. The third region, until the minimum ionization, corresponds to the non relativistic case, where $\beta\gamma < 3.5$ or $\beta < 0.96$. In this case, the Bethe-Bloch equation may be approximated by

$$-\frac{1}{\rho}\frac{dE}{dx} \simeq \frac{1}{\beta^2} \tag{I.6}$$

while the particle is slowing down, the energy loss per unit distance becomes greater, forming a Bragg peak, extremely useful in radiotherapy.

For $\beta\gamma > 3.5$ the particle is now considered ultra relativistic, since $\beta > 0.96$, so the energy loss is dominated by the $\log(\beta\gamma)$ term and is practically constant, forming the Fermi plateau.

Another aspect of interest is that the stopping power does not depend on the particle's mass, but rather on its charge, thus a particle with twice the charge will experience four times the stopping power, in a given medium, with the same velocity, for example, an alpha particle versus a proton.

I.3.7 Biological effects of radiation

Ionizing radiation may have biological effects, ergo affecting human life, whether the source comes from therapeutic and medical diagnosis or it is a natural resource, and whether it is a small or large dose of radiation.

The biological effects of radiation start at the small scale and then may impact at a larger scale. This means that at the very beginning of the chain is the interaction of the radiation with the atoms of the human body (or any other animal), possibly causing its ionization. This ionization, while making an impact on the atoms, may impact the whole body, since the ionization of an atom may affect the surrounding molecule, which may impact the normal cell's activity, leading to the possibility of affecting the tissue, which may affect an organ, thus affecting the whole body [35] .

There are two major classes in which radiation can affect the cells, which are called the direct and indirect effects.

It is referred to as a direct effect, any radiation that interacts with the DNA molecule's atoms or some other structure critical to the survival and to the normal function of the cell. When a cell is exposed to radiation, the probability that it actually interacts with the DNA molecule is very small, due to the fact that the cross section of this interaction is very small, since these critical components occupy a really small part of the cell, which is mostly composed by water. Therefore, it is highly likely that the radiation will interact only with the water in the cell. When this happens, the radiation may break the chemical bonds that hold the water together, producing hydrogen (H) and hydroxyls (OH). These fragments will likely interact with other ones, with ions or even with one another, forming compounds, such as water, thus not harming the cell. However, they may also combine to form toxic substances, such as hydrogen peroxide (H_2O_2), which can contribute to the cell's destruction. This is a good example of an indirect effect of radiation. It is not hard to imagine that these indirect effects, although less dangerous in general, happen more frequently than the direct ones. The direct effects are predominant for radiation with higher LET, such as neutrons, protons and alpha particles.

There are four possibilities that can occur when radiation interacts with the DNA, depicted in Figure I.15. The first, being the least worrying case, is when the cell completely repairs the damage inflicted by the radiation. If the damage is strong enough, the cell dies. In some occasions, the cell may resist

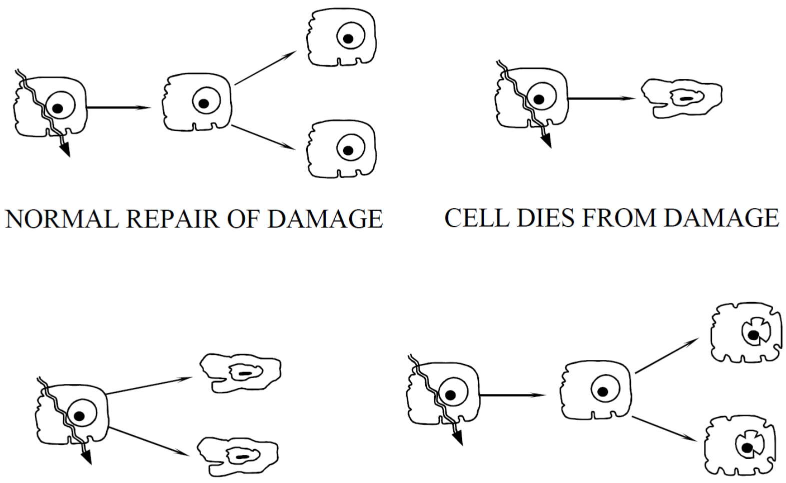

Figure I.15: Sketch of possible outcomes of radiation interaction with DNA.

the damage and is able to replicate itself, but the daughter cells die, due to the lack of some critical component. The last scenario, but not the least, being in fact the most dangerous of all the scenarios above, is when a cell is affected in a way that it does not die, but becomes mutated, while not losing its ability to reproduce, thus extending the mutation to its daughter cells. This could be the origin of a malign tumor, leading ultimately to cancer [35].

Main types of DNA damage and repair

The most common DNA lesions are base lesions, single strand breaks (SSB) and double strand breaks (DSB), with the latter being the most toxic form of lesion, since the repair efficiency is lower and, when not repaired, the cell dies or chromosome aberrations arise [36]. Figure I.16 illustrates the differences between the three reported lesions. The top and bottom lines present the DNA's sugar-phosphate backbones (SP), while the middle lines represent the base pairs (B). The red 'x' indicates the damage position in the DNA. According to the definition, damage in the sugar-phosphate backbones is a strand break, while a damage in the base pairs is considered a base lesion [37]. The DSB is defined as two SSB on opposite strands separated by ten or less base pairs. A complex DSB is a DSB accompanied by another SSB within ten base pairs. If there are two DSB separated by less than 10 base pairs, it is defined as being a DSB^{++}.
A general view of the DNA repair mechanisms, according to the damage suffered, is depicted in figure I.17. The SSB and base damages are almost always repaired through the base-excision repair (BER) mechanism. where, after de damage site is identified, the surrounding region is excised. The missing piece is then resynthetized using the opposite strand as a template [38]. Either one or up to ten nucleotides are synthetized. Figure I.18 illustrates this process [39], having in mind that there are four nucleobases - cytosine (C), guanine (G), adenine (A) and thymine (T) - and that the possible connections are A-T and C-G. So, if the base of the opposite strand where the lesion occurred is guanine, then its correct pair would be cytosine. DSB, however, are more likely to result in cellular death or chromosome aberrations, that is

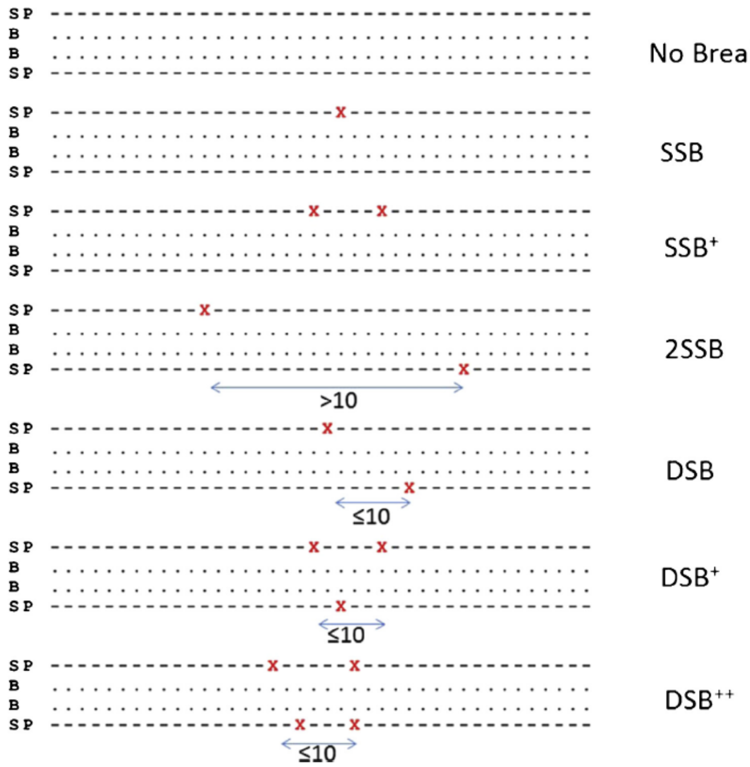

Figure I.16: Model of DNA damage.

Table I.6: Cell cycle phases

quiescent/ senescent	Gap 0	A resting phase where the cell has left the cycle and has stopped dividing.
Interphase	Gap 1	Cells increase in size in Gap 1. The G1 checkpoint control mechanism ensures that everything is ready for DNA synthesis.
	Synthesis	DNA replication occurs during this phase.
	Gap 2	During the gap between DNA synthesis and mitosis, the cell will continue to grow. The G2 checkpoint control mechanism ensures that everything is ready to enter the mitosis phase and divide.
Cell division	Mitosis	Cell growth stops at this stage and cellular energy is focused on the orderly division into two daughter cells. A checkpoint in the middle of mitosis (Metaphase Checkpoint) ensures that the cell is ready to complete cell division.

why they are more toxic. The basis of the choice of DSB repair mechanism is not fully understood, but the more complex cells tend to opt the non-homologous end joining (NHEJ) one [40]. While homologous recombination (HR) is quite important in cells in late S/G2 phase, NHEJ is important in all cell cycle phases. The former is a slow repair process, when compared to the latter. Table I.6 summarizes the different phases of the cell cycle.

The DNA damage is different for sparsely (lower LET) and densely (higher LET) ionizing radiation. In general, the greater the LET of the incident radiation, the more hazardous it becomes, since more densely ionizing radiation give rise to clusters, which are closely spaced lesions. Ionization of local water molecules will give rise to reactive oxygen species (ROS) that may also reach with the backbone and with the bases and generate more DSB in the proximity. While low LET radiation may cause the same spectrum of lesions, these will be more widely spaced, having a smaller number of nearby crosslink or

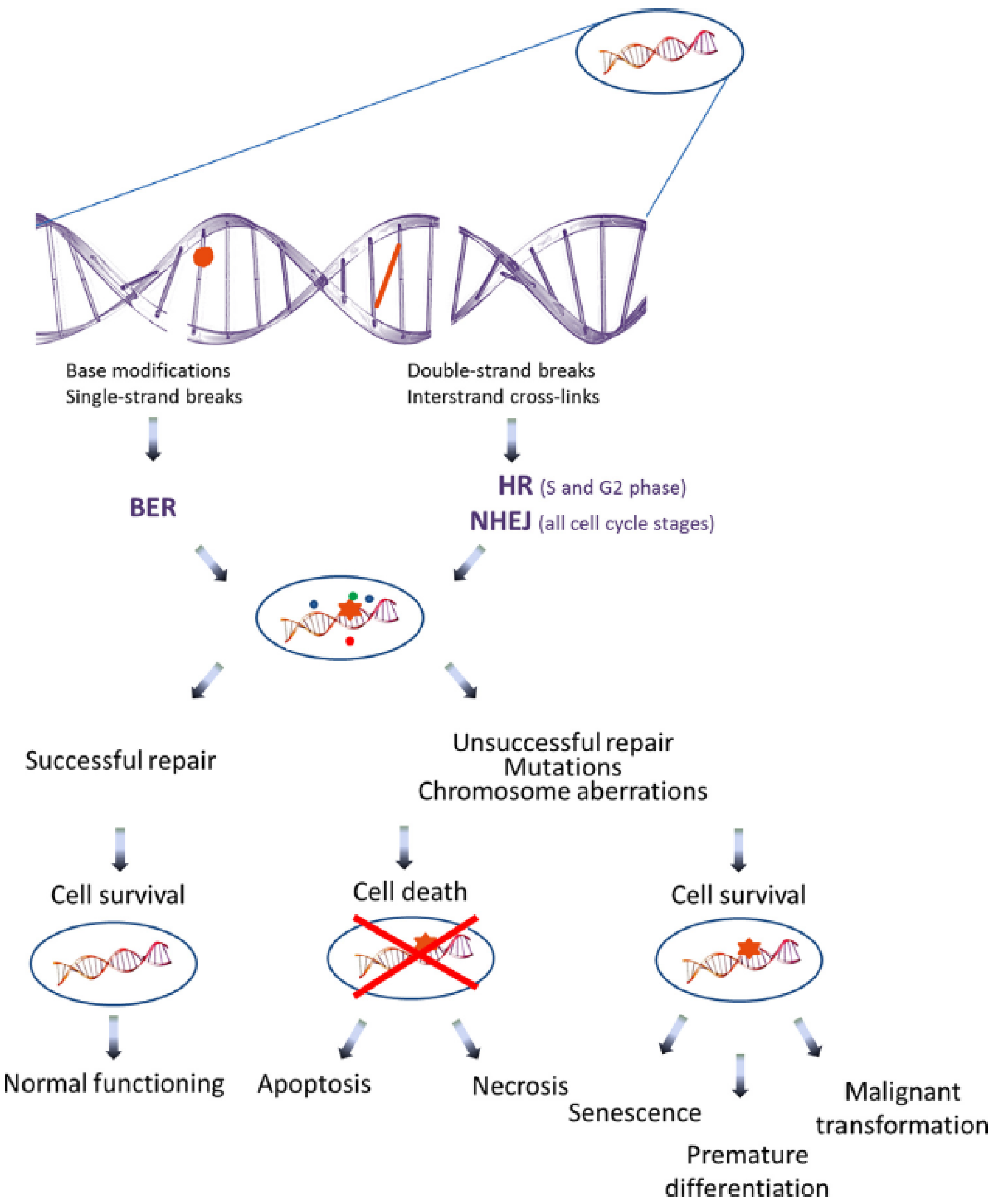

Figure I.17: Model representing the DNA repair mechanisms.

base damages, as depicted in figure I.19 [41].

High LET radiation may not only cause more damage, but also activate different response mechanisms. This helps to understand why lesions induced by higher LET radiation are known to have slower repair rate and more genetic mutation frequency [41].

Relative Biologic Effectiveness

If one wants to make the most realistic experiment possible, one has to irradiate a sample of bacteria and estimate the survival and mutation times. It is not economically feasible, though, to generate all the different types of radiation that reaches the Martian surface, nor would be completely safe, since some quantity of radioactivity would be present. For these reasons, it is necessary to have a different and, at

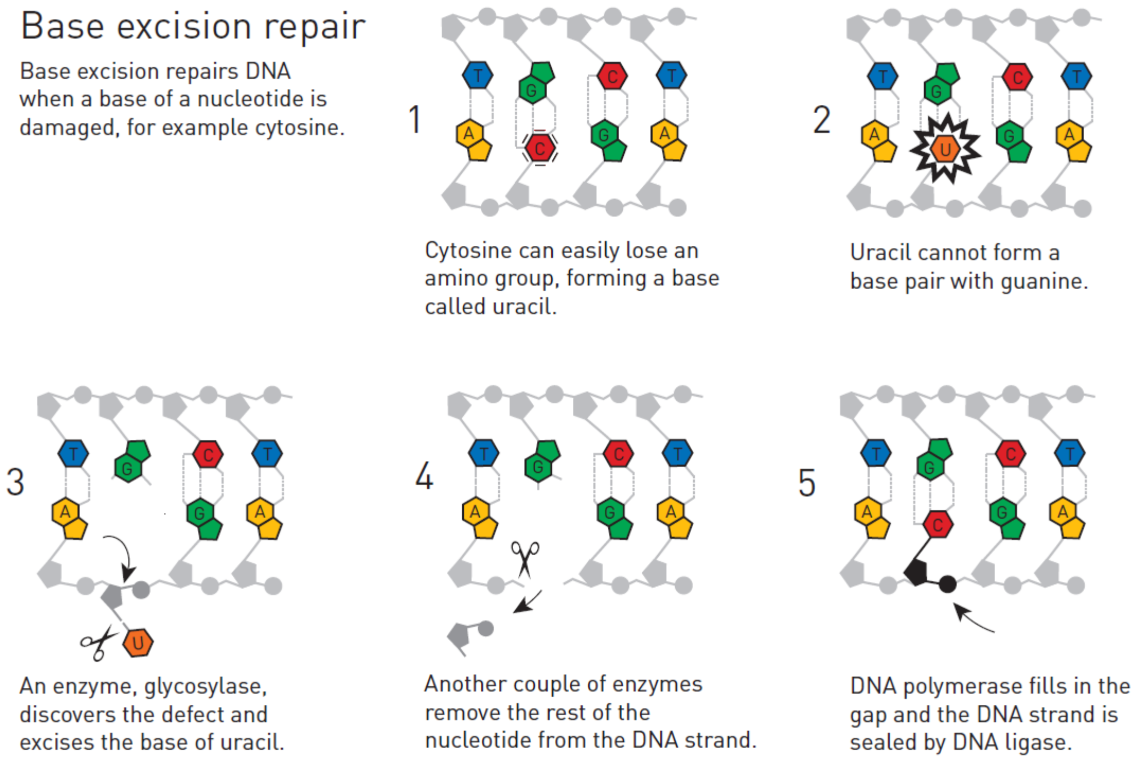

Figure I.18: Base-excision repair model.

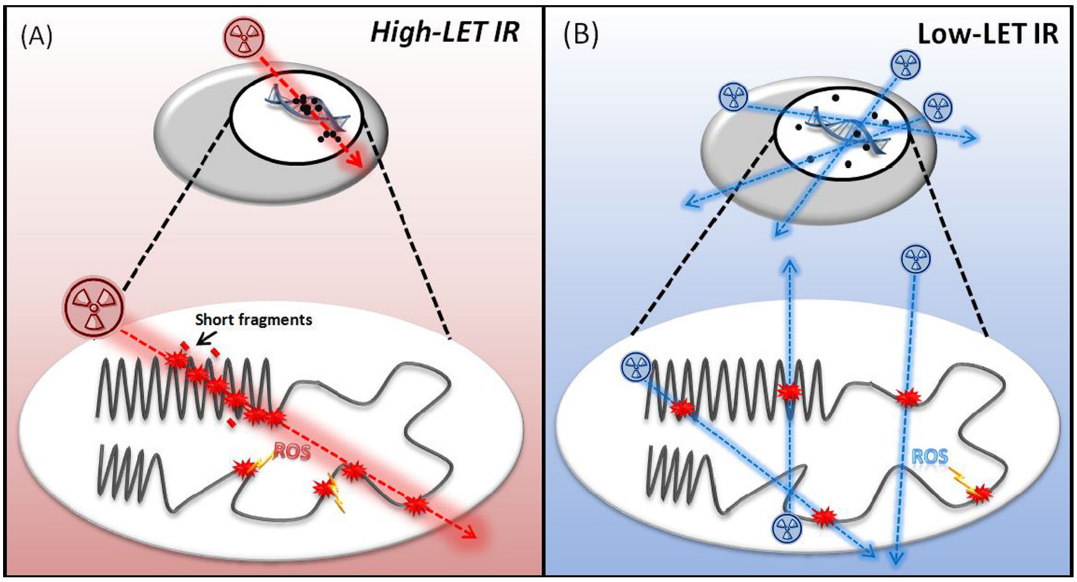

Figure I.19: Model representing the DNA repair mechanisms.

the same time, reasonable approach. The Relative Biologic Effectiveness (RBE) of some test radiation **r** compared with x-rays, according to the National Bureau of Standards in 1954, is defined as being the ratio D_X/D_r, where D_X and D_r are, respectively, the doses of x-rays and the test radiation required to produce the same biological effect. In order for this quantity to make sense, one shall choose a biological system in which the effects of radiation may be evaluated quantitatively [42]. For the purpose of an example, let us consider the lethality of plant seedlings. In order to measure the RBE, it is necessary to have a reference radiation, 250 kV x-rays, and a test radiation, 15 MeV neutrons. So, the next step would be to have two groups of these seedlings, one being irradiated by the x-rays and the other with the neutrons. At the end of the observation, it is possible to compute the dose of the former and the latter radiation type that induced a death of half of the seedlings, designated by LD_{50}. The ratio of these two doses will give the value of the neutron's RBE. Supposing that the LD_{50} for the x-rays is 6 Gy and for the neutrons is 4 Gy, their RBE will be 1.5. So, in general, the greater the RBE, the more hazardous the test radiation will be.

Relation between RBE and LET

RBE and LET are related quantities. Figure I.20 shows the dependency of RBE with LET for mammalian cells of human origin, with the first, the second and the third curve representing survival levels of 0.8, 0.1 and 0.01, respectively. It can be seen that the RBE does not exclusively depend on the radiation, but also depends on the level of biological damage and, therefore, on the dose level [43]. One thing in common, though, is that in all three cases RBE increases slowly until 10 keV/μm, and then it starts increasing rapidly with LET, where the maximum of RBE is registered at 100 keV/μm. Beyond this value, RBE starts to decrease to lower values.

The optimal LET for biological damage is, thus, around 100 keV/μm. This happens because, at this

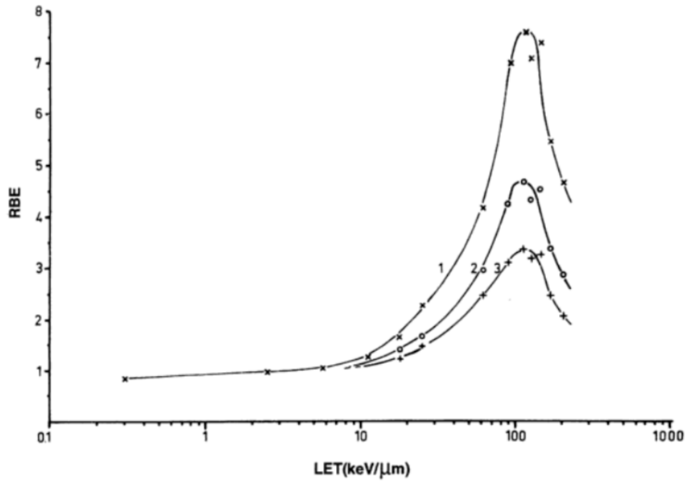

Figure I.20: RBE as a function of LET for survival of mammalian cells of human origin [43].

density of ionization, the separation of two events coincides with the diameter of the DNA double helix, which is approximately 2 nm. So, radiation which has a mean separation of events that coincides with the DNA double helix is more likely to cause DSB, hence is more hazardous to life, since the exchange-type aberration due to the interaction of two double-strand breaks is the basis of most biologic effects [42].
Due to their high resistance in hazardous environments, *Bacillus* endospores are one of the model systems most used in Astrobiology [44]. Figure I.21 shows the RBE values of the inactivation and mutation induction as a function of LET for *Bacillus subtilis* spores, since the former values are relative to X-ray exposure. The white bars represent the inactivation, while the gray bars represent rifampicin resistance, $\mathrm{Rif}^{\mathbf{R}}$, mutation induction. As one can see, RBE values for both inactivation and mutation induction increase with LET, for its maximum value corresponds to a LET value of 200 keV/μm. Altough different subjects were studied, the RBE-LET relation is similar in both cases.

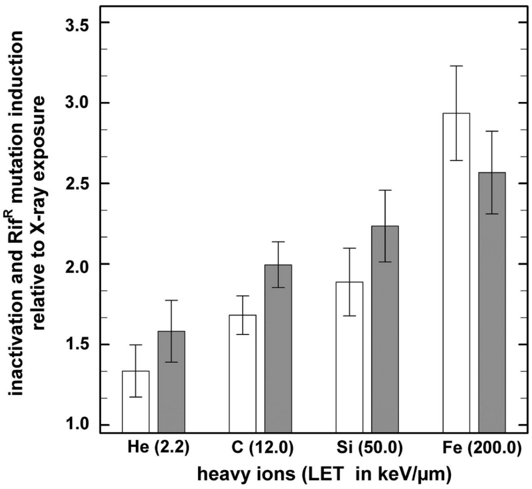

Figure I.21: RBE as a function of LET for *Bacillus subtilis* spores. The white bars represent the inactivation, while the gray bars represent Rif$^{\mathbf{R}}$ mutation induction [44].

The current state of the art of LET at Mars is the Curiosity's measurement at the surface, which is shown in Figure I.22 [19]. The same figure also shows the LET measurement inside the Mars Science Laboratory (MSL) spacecraft during its journey from Earth to Mars. This LET was computed in water,

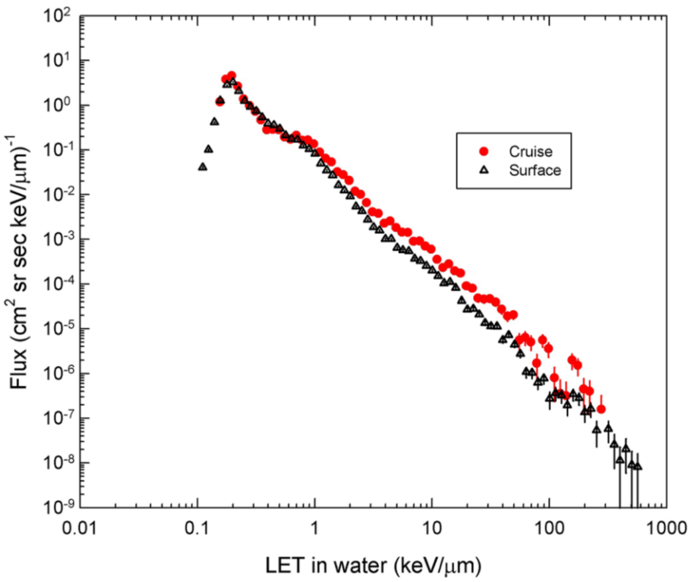

Figure I.22: LET spectrum comparison between the measurement during the cruise journey inside the MSL spacecraft (red) and the surface of Mars (black).

since it represents the major composition of known life. As one can see, the flux corresponding to a 100 keV/μm LET is significantly low (around 10^{-6} particles per cm^{2}sr sec keV/μm), and the majority of the LET flux is located around 0.2 keV/μm, which has an RBE value around 1.

Low-dose and low-dose-rate exposures cannot be entirely predicted from the results of high-dose studies (Amundson et al., 2003) since the biological effects are much more complex than predicted by the linear non-threshold model (LNT). This model assumes that the biological damage caused by ionizing radiation is proportional to the dose, without taking into account dose rates, meaning that radiation is always considered to be harmful, since the sum of several small exposures are considered to have the same effect as one larger exposure, thus no threshold is set. This model was established in the 1960s. As the scientific understanding of radiation and its hazardous effects has improved, some modification to this LNT model have occurred, shown in Figure I.23 [45], where the relative risk as a function of the dose is plotted.

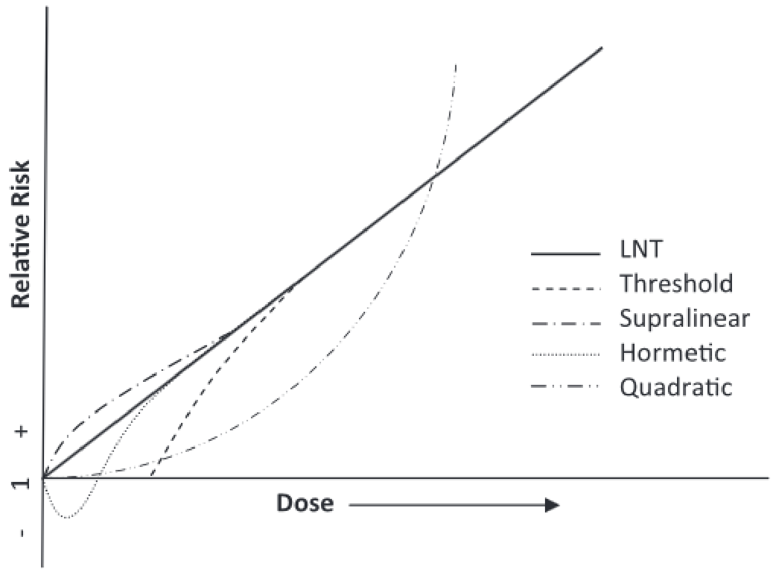

Figure I.23: Various response models to low doses.

The biological effects of this low-dose radiation depend on several factors, including the DNA repair capacity, delayed genomic instability and induction of signal transduction molecules (Nam et al., 2010; Neumaier et al., 2012; Park et al.,2013). Thus, cells exposed to low-dose radiation may develop adaptive resistance to subsequent high-dose radiation-induced gene mutation, DNA damage and cell death (Shiraishi et al., 2005; Mitchel et al., 2008; Liang et al., 2011; Kalantari et al., 2014). Although several mechanisms have been proposed, insufficient data is currently available to fully understand the impacts of low-dose and low-dose-rate radiation on biological tissues.

I.4 Geant4

Geant stands for Geometry and Tracking, which is an object-oriented toolkit for the simulation of the passage of particles through matter, using Monte Carlo methods [2]. It is written in C++ programming language and it is based on an object oriented design. The Geant4 source code is available at its web page and it is available for the main operating systems.

Initially, Geant's main target was high energy physics (HEP). Now it is used in other areas, such as nuclear experiments, medical, accelerator and space physics studies, providing a treatment of particles interactions from the hundreds of eV to the PeV, as well as thermal energies for neutrons.

In the design of such a large and powerful software system, the partition into smaller logical units becomes essential, making it well organized and easier to develop. Although it evolved during time, its basic structure has remained the same, and the class category diagram designed for Geant4 is presented in Figure I.24.

Categories at the bottom of the diagram are used by all other categories, being the foundation of the toolkit, which are the *Global* category, for it is responsible for handling the system of units, constants and random number generation, *Materials*, *Particles*, *Graphical representations*, *Geometry*, providing all the volumes of the 'world', including the detector, and *Intercoms*, which basically provides a means to interact with Geant4 through the user interface. Above these categories exists the ones responsible for tracking the particles and to describe the physical processes they suffer. The *Track* category contains, naturally, classes for tracks and steps, used by *Processes* which encompasses implementations of these models of physical interactions. Additionally, a process called *transportation*, as the name suggests, is the responsible for the transport of the particles throughout the geometry and, optionally, allows the triggering of the parameterisations of processes, which is basically a fast simulation, where a fast algorithm is implemented. For example, a typical use case is the shower parameterisation, where several thousand steps per GeV computed in the detailed simulation are replaced by a few tens of energy deposits. They usually take place in an envelope, which is typically the mother volume of a detector and may be applied to specific particles and energy range. All these processes may be summoned by the *Tracking* category. Over these, the *Event* category manages, also like its name suggests, events in terms of their tracks and the *Run* manages groups of events that share a common beam and detector. So, an event is the primary unit of an experimental run, taking into account everything that happened to each primary. A more basic unit is the track. It consists of a set of primary particles and a set of detector responses to these particles. So one run consists of N events, each one of them has associated 1 or more tracks.

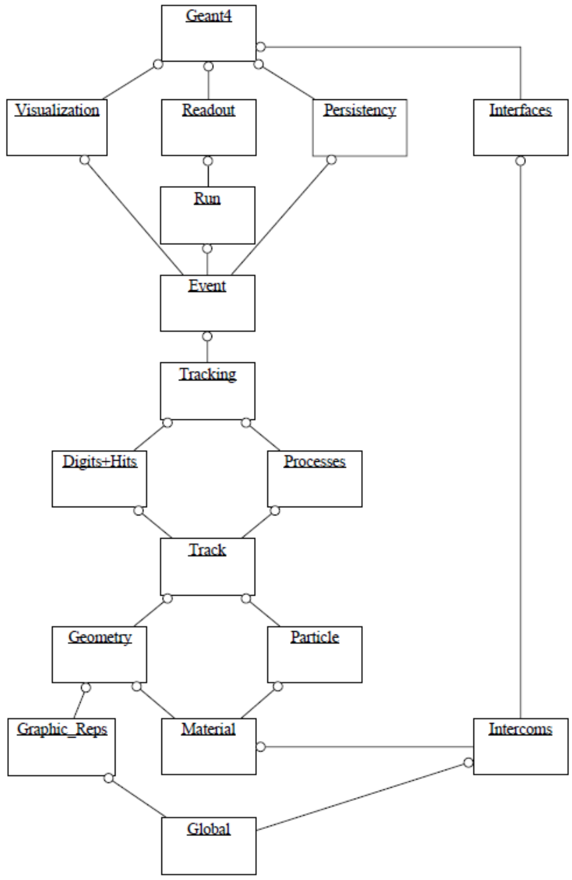

Figure I.24: Diagram of Geant4's classes.

The *Readout* category allows the handling of 'pile-up'. Finally, capabilities that use all of the described above and connect to facilities external to the toolkit are provided by the *Visualization*, *Persistency* and *Interface* categories.

Chapter II

Description of the simulation

II.1 Goal

Since the damaging effects of ionizing radiation on biological structures, such as cells, is one of the greatest limiting factors on the survival of life, the aim of this thesis is to analyze the radiation environment, not only at the surface of Mars, but also at regular depths of its soil. These simulations will take place on two different scenarios, both related to weather scenarios modulated by the sun, namely at solar activity minimum and maximum. For the latter, two different kinds of radiation will be simulated: GCR, and SEP, whereas for the former only protons and α particles coming from GCR will be simulated, since the probability of having an SEP increases with solar activity. Plots of particle flux (primary and secondary particles) as a function of energy of the primary and as a function of the LET will be analyzed. This LET is calculated in water, since it represents the major component of life as we know it. All this information combined will make possible the understanding of preservation limits of organic matter in the Martian soil.

A schematic representation of all parties involved in the simulation framework is shown in figure II.1.

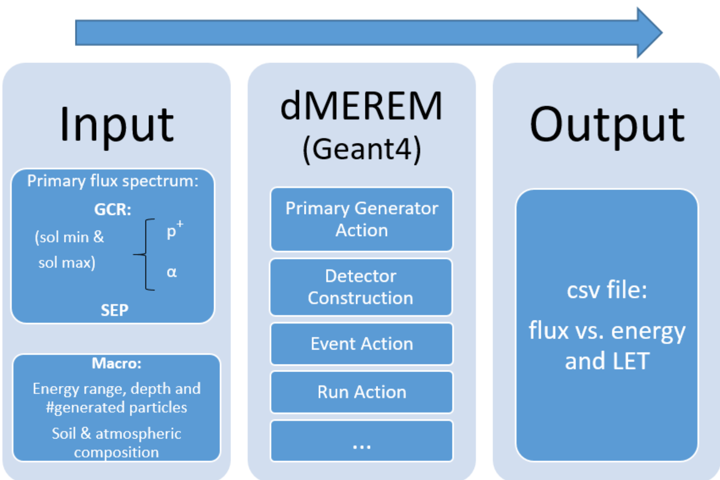

Figure II.1: Representation of the simulation framework

II.1.1 Particles input

dMEREM receives an incident energy-flux spectrum as input, in this case by SPENVIS, which stands for Space Environment Information System [46]. Using this webpage, the user can control the incident particle spectra, choosing which model and database to use. Figure II.2 shows the SPENVIS parameter page, allowing the user to define the

- epoch of study;
- latitude, longitude and altitude (km above the surface) or depth (g/cm^2 below the surface);
- area of the geometry to be used, also in km;
- soil composition and density, which can both be user defined;
- source type, where SEP, GCR or X rays can be selected;
- number of primary particles to be generated, spanning from 10^2 to 10^5;
- physics scenario, where the user can make a *quid pro quo* between simulation time and precision.

Figure II.2: SPENVIS parameter input page.

The input file to be read by dMEREM is a two-column csv file (comma-separated values), containing the energy and the respective flux. The input spectra for proton and α-like GCR, for solar minimum and maximum, are plotted in figure II.3. The simulations took place under solar cycle 24, with the minimum corresponding to January 30th, 2009, and with the maximum corresponding to January 30th, 2014. Since SEP are sporadic events, only the worst case scenario will be analyzed, with the respective input spectrum in II.4. All these spectra are in section A.1 in table format.

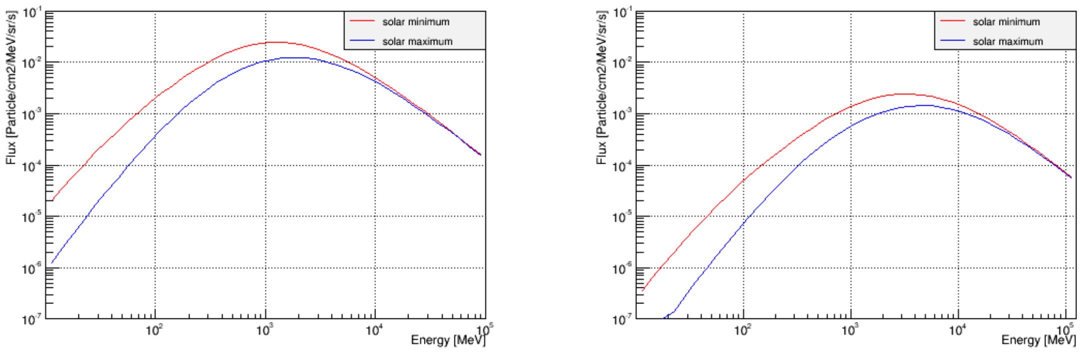

(a) (b)

Figure II.3: GCR flux spectrum as a function of energy for protons (a) and for alpha particles (b), as input to dMEREM.

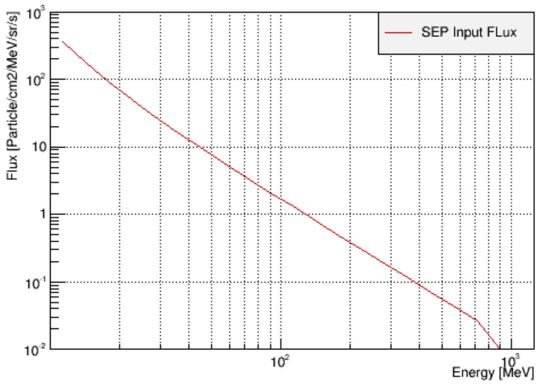

Figure II.4: SEP energy spectrum.

The conditions of how the particles are generated, as well as their type, quantity and energies are defined through a macro that is read by dMEREM just before the start of the run, which may be also provided by SPENVIS. This way the user does not have to modify anything inside dMEREM. Thus, the user is able to define the energy ranges to be generated, as long as it is contained in the input spectrum.

The soil's composition, also mentioned in section I, as well as its coordinates can be seen in table II.1, whereas the composition of the 20 atmospheric layers can be seen in table A.6.

II.1.2 dMEREM

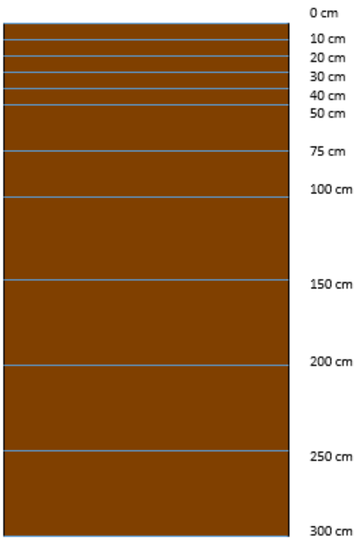

Figure II.5: A sketch of the position of all detectors within the Martian soil.

The detailed Martian Energetic Radiation Environment Model (dMEREM) is a Geant4 application, which enables a Monte Carlo analysis of the Martian radiation environment, providing a high fidelity simulation, not only of the environment, but also of the physical interactions between all particles considered, such as protons, gammas and heavy ions. A possible drawback of using such a detailed model is the time taken to perform these calculations. The engineering Martian Energetic Radiation Environment Model (eMEREM) is quicker, since it is based on the FLUKA radiation transport program, relying on a set of pre-computed response functions to compute the interaction of particles with the geometry, hence requiring fewer computation time [30]. Although this is an advantage over dMEREM, it lacks in precision. Hence there is a tradeoff between time and precision. Both were developed under ESA's MarsREM Project, also involving LIP (Laboratório de Instrumentação e Física Experimental de Partículas).

dMEREM is composed by an atmosphere of 20 layers, each with its own density and composition, and same thickness (in g/cm^2), meaning that since the atmosphere's density is higher at lower altitudes, the lower layers will be thinner than the higher ones, in order to guarantee the same thickness. The atmosphere has a total depth of 14.6074 g/cm^2, it is 50 km high and the soil is 100 m deep, both 300 km wide. If the magnetic field is turned on, an additional layer of 100 km height is placed on top of the previous atmosphere, in order to take into account the larger variability in the trajectory of the particles, as well as an increase of 900 km of the soil's width. The model is depicted in Figure II.6.

Table II.1: Soil composition used for the simulations and its coordinates.

Latitude (°)	Longitude (°)	H_2O (%)	Fe_2O_3 (%)	SiO_2 (%)	Bulk (%)	FeS (%)	ρ (gcm^{-3})
-4.49	137.42	3.687	13.005	51.208	32.1	0	1.77855

dMEREM's structure

Belonging to one of the main classes, the Detector Construction is responsible for placing the atmosphere and soil volumes. This is where the characteristics of each layer are defined, such as composition, density, temperature and dimensions, as well as the position of the detector. The PrimaryGeneratorAction class is responsible for the generation of the primary particles, such as the type of particle, its starting position and direction. It has the feature of communicating with a macro. This makes the particle generation process more user friendly.

The class responsible for the physics to be used will be the PhysicsList. This concept of physics list comes from the fact that Geant4 does not cover all known processes and particles ranging the entire

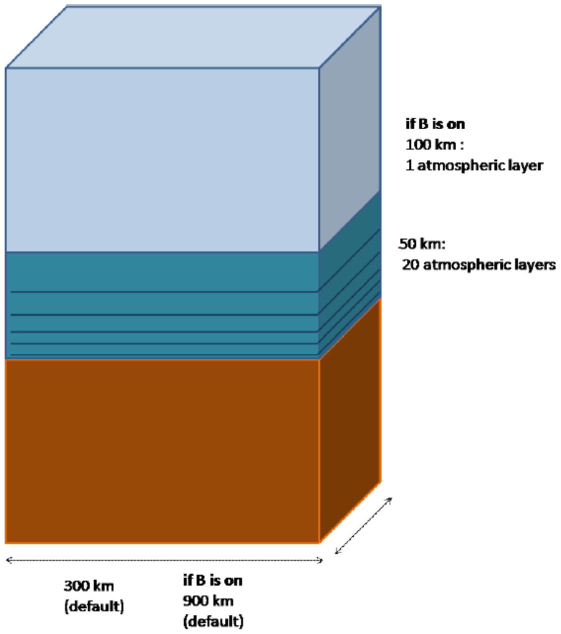

Figure II.6: Representation of the model's geometry.

energy domain from zero to the TeV scale. As an alternative, a combination of ideas and approaches is used to execute a simulation task [47]. This means that the user shall choose which models to use, for there are models that are competitive in the same energy region, where one works better for certain particles, while the other may be better for other species. Thus, models have to be combined in order to cover the desired energy range and particles the best as possible, in order to optimize the simulation speed.

The Event Action class represents an event, storing what happened, i.e. the deposited energy and LET in the region, as well as the change of position of the particles. This class allows the user to insert code at the beginning and end of an event.

The Run Action class is responsible for the making of the output file, which will show the desired results of the simulation. In this case, this file contains the energy bins' limits and their associated flux (downwards and upwards) for every particle shown in the results, whether it is a primary or secondary. It also displays the detector's depth in g/cm^2 as well as in m, the effective dose and the ambient dose equivalent deposited at the detector's layer. The Soil Model and Atmospheric Model classes are responsible for reading a possible input soil and atmospheric composition, respectively.

II.1.3 Output

The particle flux, both as a function of energy and LET, is measured in 12 different positions. dMEREM allows the user to place a single detector at a given altitude inside the atmosphere, as well as in a given depth, below the soil. The first is located logically at the surface of the Martian soil, while the last one is placed at a depth of 3 m, as depicted in Figure II.5, where the position of all 12 is shown. These 12 layers will provide a good insight about the profile of the radiation environment of the Martian soil within a lower depth.

Chapter III

Results

III.1 GCR

Table III.1 shows the conditions of generation for the different simulated scenarios, with the atmospere and soil compositions presented in tables A.6 and II.1, respectively. Thus, these simulations were performed for Gale Crater's soil composition. A cut of 100 keV on the generation of secondary particles was imposed, this means that no secondary particles with kinetic energy below that value will be created. A direct consequence of the 100 keV cut is the increase in the flux of lower energy protons, since without the cut they would form secondary particles with energy below this threshold, thus disappearing at higher energies. The deposited energy is the same as the no-cut scenario.

Table III.1: Table summarizing all simulations.

Type of Radiation	Energy range	Statistics used
GCR-proton (max & min)	10 MeV - 1 GeV	5M
	1 GeV - 100 GeV	500k
GCR-α (max & min)	10 MeV - 1 GeV	5M
	1 GeV - 100 GeV	250k

III.1.1 Primary particles

Protons

The input spectrum is presented in Figure III.1, for both solar minimum and maximum.

As seen in figure III.3, at the surface the flux increases until around 0.5 GeV and then it starts to decrease, presenting a similar trend of the spectrum given as input. The flux's peak is actually slightly shifted to the left (the energy of the peak is around 500 MeV, not reaching 1 GeV). This happens because the particles lose energy during their trajectory, due to the interactions with the Martian atmosphere. Moreover, the greater the particle's energy, the fewer the energy it shall lose (for the considered energy range). This phenomenon may be observed at lower depths (table A.1, A.2 and A.3), where a concentra-

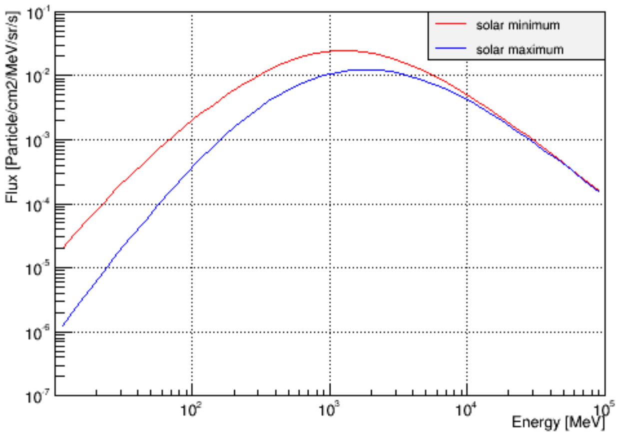

Figure III.1: proton GCR input spectrum.

tion of particles is registered, due to a 'migration'. Protons around 1 GeV lose very little energy, while the lower energy protons lose more energy, consequently being 'stored' at lower energies. Comparing the proton flux at the surface to the input spectrum, one concludes that the Martian atmosphere is not negligible, since interactions of the primary particles with the latter are quite significant (for their flux is cut by a factor between 10 and 10^4, depending on the energy range, for both solar activity levels). Figure III.2 shows the range of protons in carbon dioxide (major component of the Martian atmosphere) as a function of their kinetic energy, computed from the National Institute of Standards and Technology (NIST) site [48]. According to this figure, only protons with a kinetic energy above roughly 125 MeV

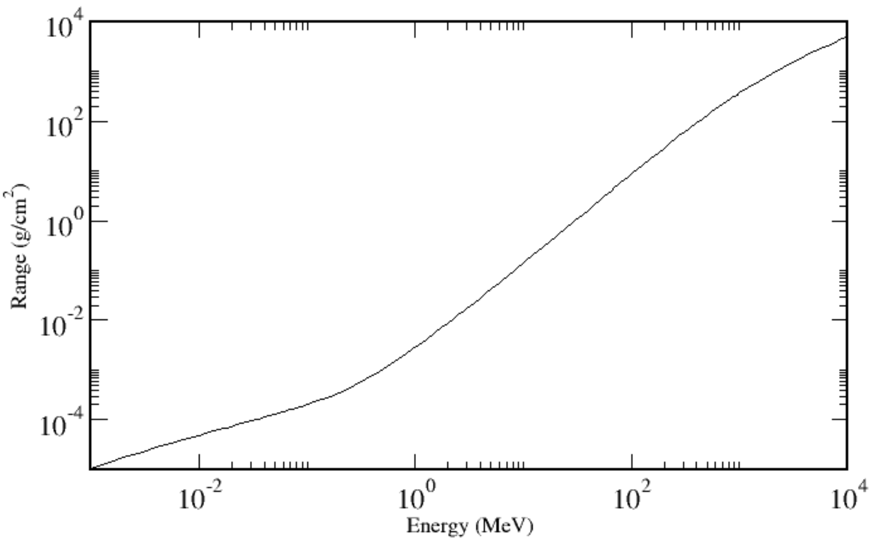

Figure III.2: Range of protons as a function of energy in carbone dioxide.

reach the surface (the atmosphere has a 14.6074 g/cm^2 thickness).

The flux of primary particles decreases slowly while going deeper inside the soil. This is expected due to the increase of the shielding provided by the soil, gradually absorbing those primary protons and originating secondary particles. The attenuation is almost the same, whether on solar activity minimum or maximum, as it is shown for 1 m deep in the soil. Actually, on a more thorough level, observation of the latter figure, as well as of the ones at higher depths, show us that for the lower energies the flux is slightly higher for the solar activity minimum scenario, as expected (due to the solar modulation). The flux at all studied depths are in section A.2.

Correlating the initial flux of the particles as a function of energy with this reduced Bethe-Bloch equation, one confirms the energy shifts of the flux peaks, which is shown in figure III.4 During this journey

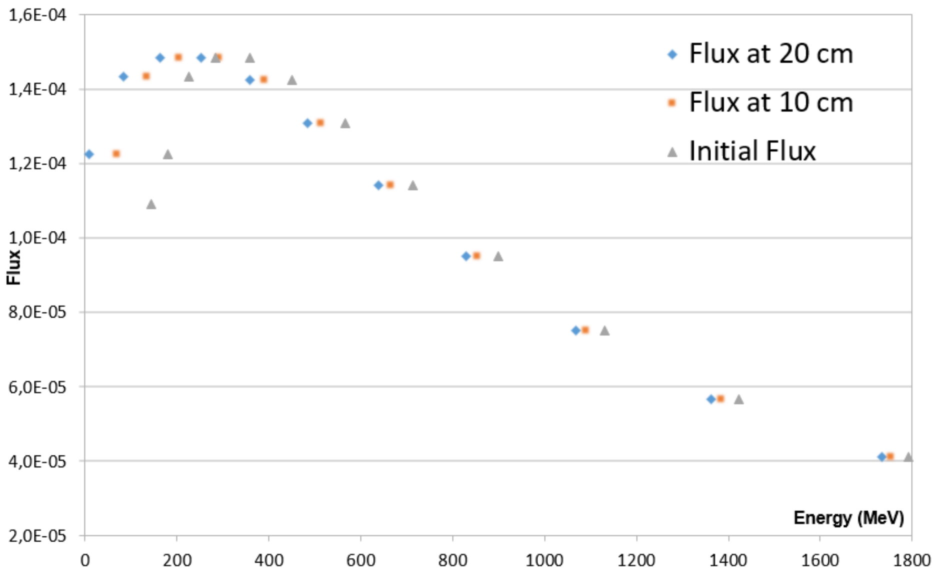

Figure III.4: Particle fluxes, with arbitrary units, as a function of soil depth computed with the reduced Bethe-Bloch equation.

throughout the atmosphere, these protons lose their energy, creating secondary particles, namely neutrons, photons and electrons, with the former dominating the majority of the spectrum. These particles (the ones that actually reach the surface) will interact with the soil, giving rise to even more particles. While these particles produced in the atmosphere will be attenuated with the increase in soil depth, more particles will be created, due to the interaction of all particles with the soil, whether they are primary protons or secondary particles that were created in the meantime. The overall spectra are presented in the next section. Figure III.5 shows the range, in g/cm^2, of protons as a function of energy, in a material with nearly the same density as the considered soil (1.85 g/cm^3 instead of 1.78 g/cm^3), computed from the National Institute of Standards and Technology (NIST) site [48].. To convert into the desired units, one must divide this range by the density. Table III.2 shows the range of protons, in cm, as a function of their energy. Protons with energy below $\lesssim$ 50 MeV are absorbed in the first centimeter of the ground. Just in order to reach the 10 cm underground layer, a proton has to reach the surface with a kinetic energy of around 150 MeV, and 250 MeV to reach the second layer of 20 cm. This helps on the understanding of the energy shift in these spectra as the particles go deeper into the soil.

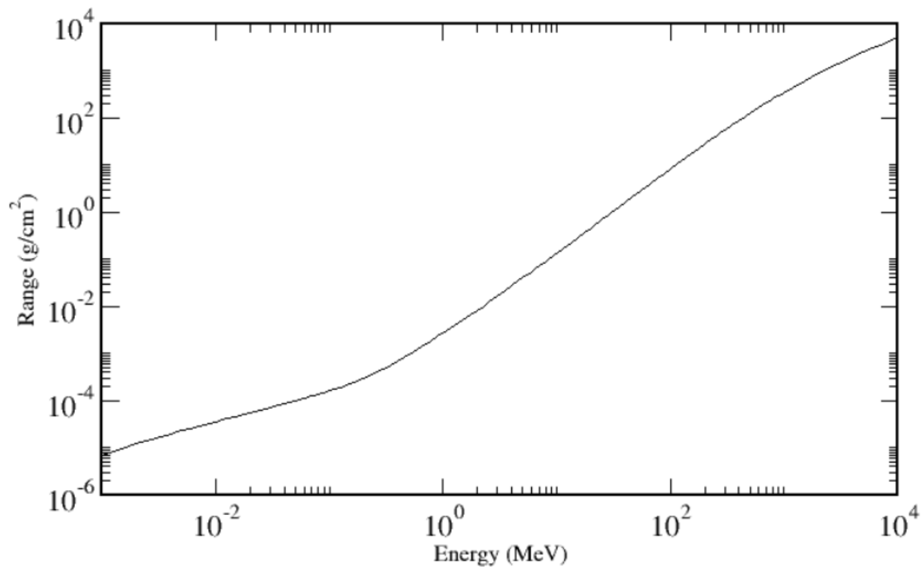

Figure III.5: Proton range in a material with a similar density as the Martian soil (bone (ICRU)).

Ekin (MeV)	**Range (cm)**
1	1,5 $\times 10^{-3}$
10	0,1
50	1,3
100	4,5
500	67,8
1 000	188,8
5 000	1339,5
10 000	2735,7

Table III.2: Proton range in bone (ICRU).

Depth	Solar minimum	Solar maximum

Surface

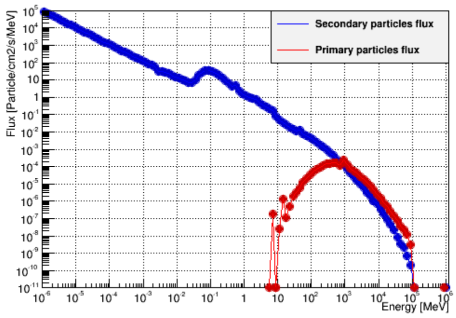

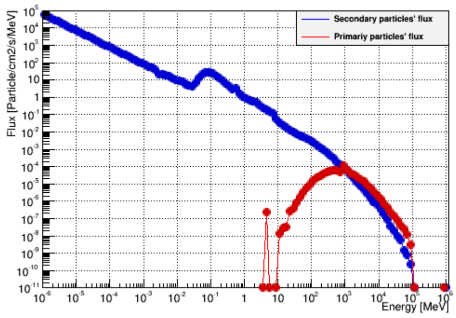

1 m

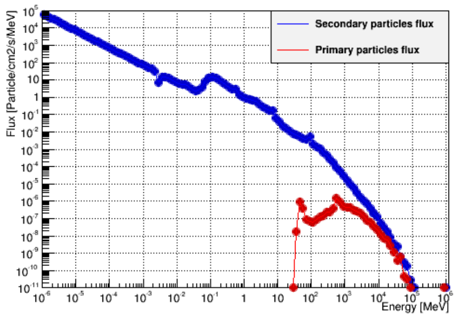

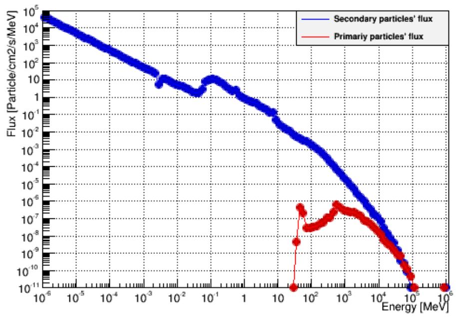

2 m

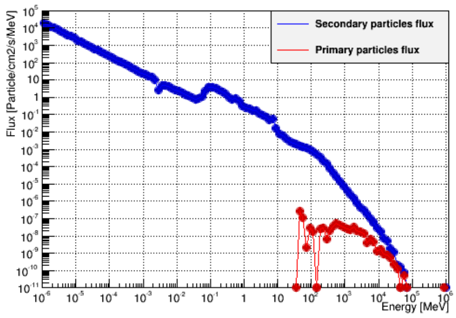

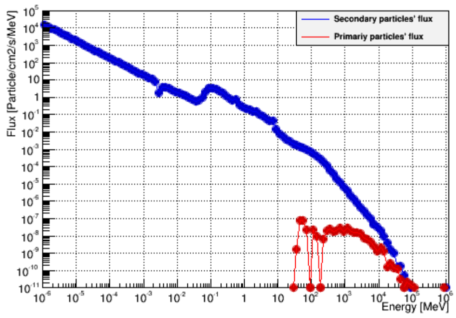

3 m

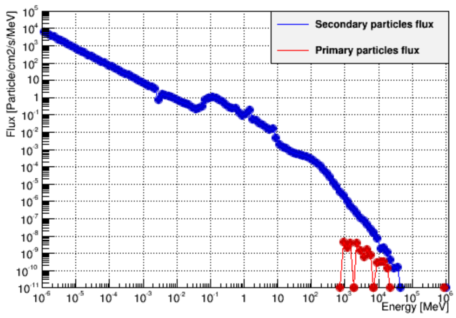

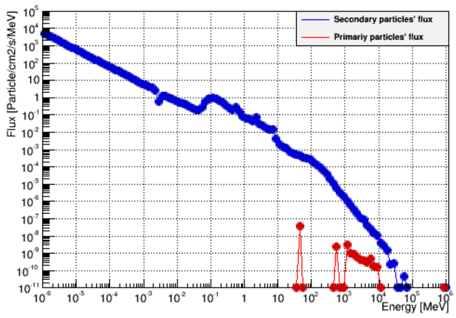

Figure III.3: Primary and secondary particle fluxes at different depths on solar activity minimum and maximum, for protons.

Alpha particles

In this section, alpha particles will be presented as primary particles. The input spectrum, both corresponding to solar minimum and maximum, can be seen in Figure III.6.

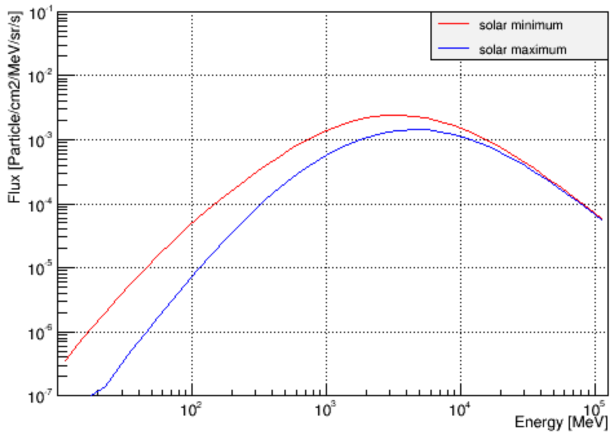

Figure III.6: proton GCR input spectrum.

Similarly to the protons, at the surface α particles' flux follow the trend of the input spectrum, with the flux peak being slightly shifted to the left, as one would expect, since the particles lost some of their energy traversing the atmosphere, as the figures corresponding to the surface at figure III.9 show, where the maximum intensity of the α spectrum at solar minimum is around 3.5 GeV and at maximum around 5 GeV, while the maximum intensity of the detected spectrum is located at 2 GeV and 3 GeV respectively. In both solar scenarios, only α particles above 100 MeV arrive the soil, contrasting with the earlier case, where protons of 10 MeV reach the ground. Figure III.7 is a plot of the range of α particles in carbone dioxide, taken from NIST. It shows that in order for a particle to traverse 14 g/cm^2 of this material, it shall have an initial kinetic energy of 500 MeV. The primary particles are almost completely

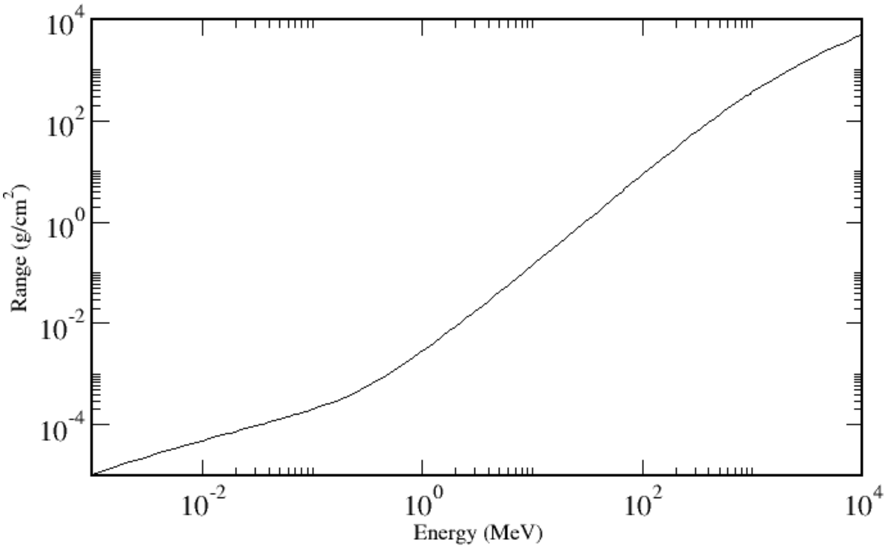

Figure III.7: Range of protons as a function of energy in carbone dioxide.

absorbed in the first centimeters of the soil. Since α particles have twice the charge than protons, they will lose energy on an earlier stage, since, according Bethe-Bloch equation, the energy loss of a particle is proportional to its charge squared. At a depth of 50 cm there is almost no primary flux. It is seen that at solar activity maximum, these primary particles persist at higher depths. This can be explained by observing both spectra at the surface, where one can notice that at the solar maximum scenario there is slightly a greater flux of high energetic particles, which potentially penetrate deeper into the ground. The flux at all studied depths are in section A.2.

Figure III.8 is a plot of α particles in bone (similar density as the considered Martian soil) and table III.3 shows some values, indicating that, in order for them to travel a few centimeters into the ground, they shall have some hundreds of MeV of kinetic energy. Figure III.9 corroborates these values, since the primary α flux decreases rapidly with depth.

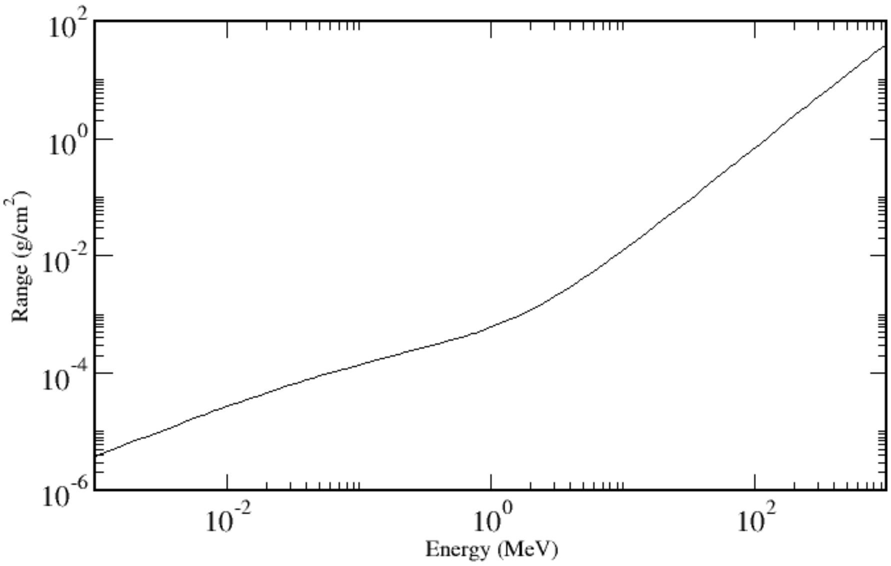

Figure III.8: Alpha range in a material with a similar density as the Martian soil (bone (ICRU)).

Ekin (MeV)	**Range (cm)**
10	$6{,}7\times10^{-3}$
100	$3{,}8\ \times10^{-1}$
150	0,8
200	1,4
300	2,7
500	6,7
1000	20,3
1 000	41,0

Table III.3: Alpha range in bone (ICRU).

Depth	Solar minimum	Solar maximum
Surface	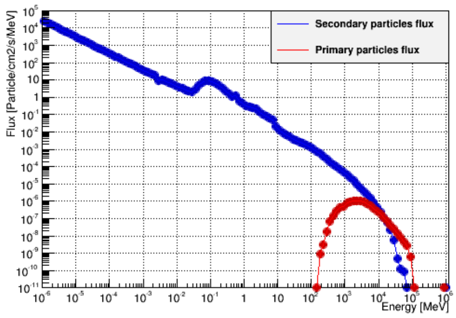	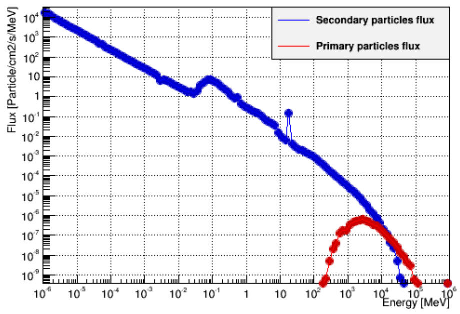
50 cm	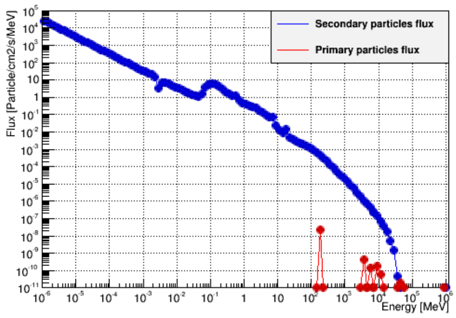	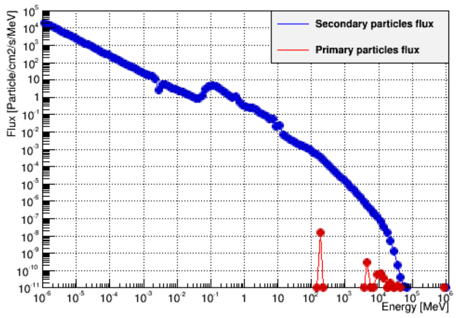
150 cm	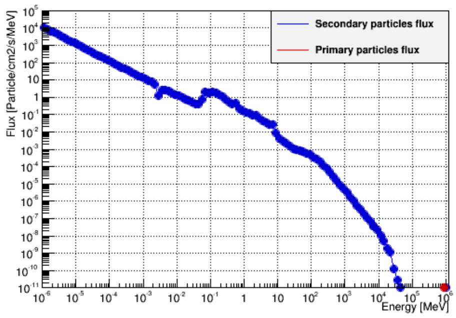	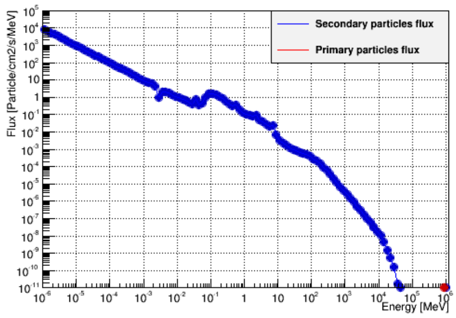

Figure III.9: Primary and secondary particle fluxes at different depths on solar activity minimum and maximum, for α particles.

III.1.2 Spectral analysis

Protons

There are secondary particles with energies around the eV being created, not only in the atmosphere, but also due to interaction of the primary particles with the soil. As one can see in figure III.10 at the surface, up to $\simeq$ 10 keV, the majority of these particles correspond to (thermal) neutrons. The reaction responsible for neutron production, as well as some other particles, is due to the interaction of the cosmic rays with the nuclei of the atmosphere through spallation [22]. A fast neutron (kinetic energy above 20 MeV) loses its energy mostly through elastic scatterings, where it will be slowing down. Remember that in an elastic scattering collision between a particle and a nucleus, the energy lost by the former corresponds to the kinetic energy of the nucleus' recoil, contrasting with an inelastic collision where the nucleus absorbs part of the particle's energy and is left in an excited state, which causes it to emit some kind of radiation to bring it back down to a stable or ground state. As the neutron loses its energy, it will undergo several random elastic collisions, increasing the probability of it to be captured. This generally happens when it reaches thermal energies ($\lesssim$ 0.1 MeV) giving rise to a (n,p), (n,2n), (n,α) or (n,γ) reaction, with the latter contributing to the formation of γ radiation. Just in order to introduce this simple notation, (n,p) is a reaction in which a neutron interacts with a nucleus and a proton is created.
Electrons are also created, which generate *Bremsstrahlung* photons. This also contributes to the formation of γ radiation. Gamma rays are also created from the radioactive decay of radioactive species and from nuclear interactions between the primary particles and the surface materials. The more energetic γ rays arise from the secondary neutrons, due to the inelastic scattering and neutron capture reactions [21]. Some elements like potassium, uranium, and thorium are naturally radioactive and emit gamma rays as they decay, but all elements can be excited by collisions with cosmic rays to produce this kind of radiation [49].
Comparing tables III.3 with III.10, one concludes that the protons reaching the surface are mostly primary particles, with the exception on energies below $\simeq$ 10 MeV, clearly dominated by secondary protons generated due to the interaction of the cosmic radiation with the atmosphere.

Depth	Solar minimum	Solar maximum

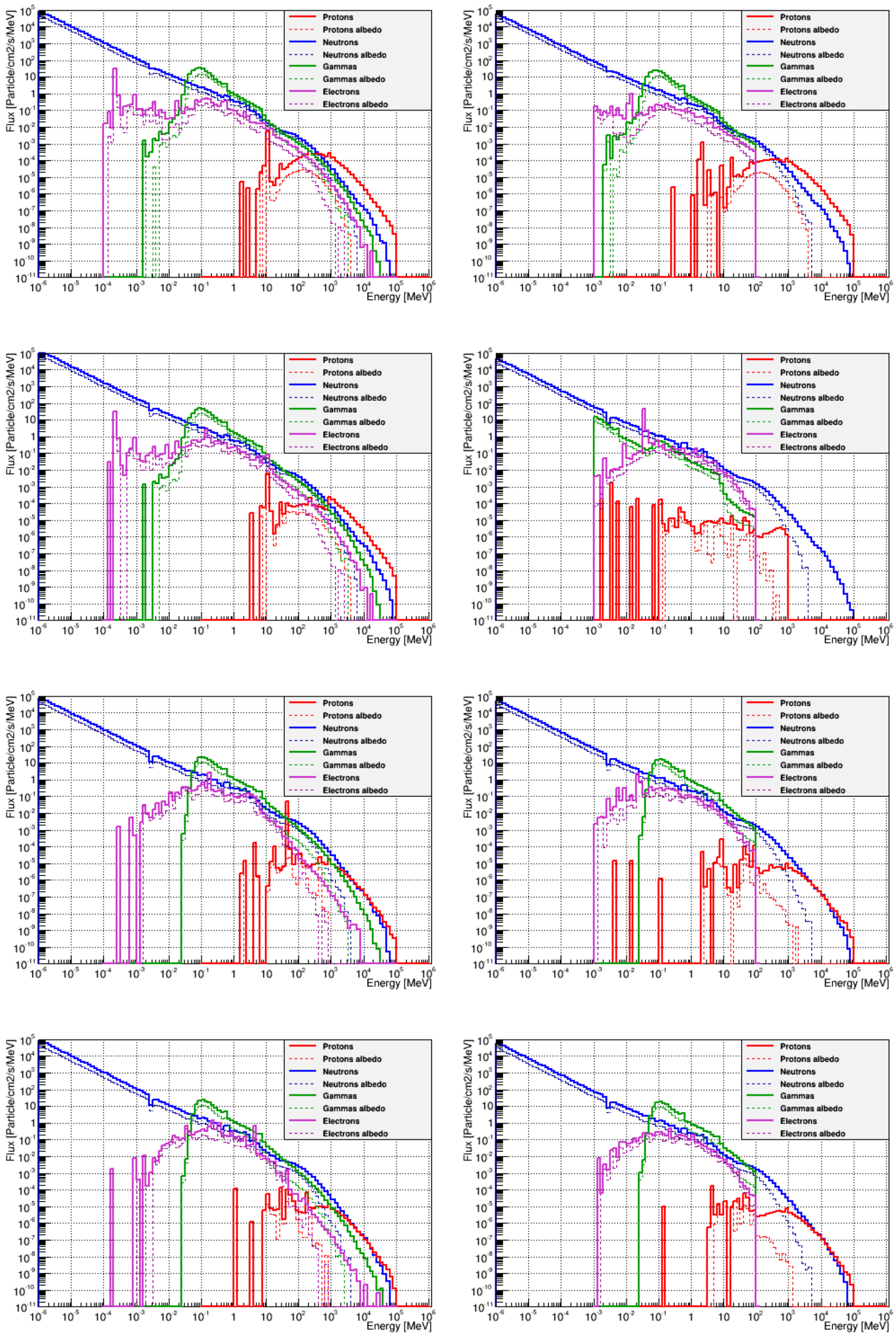

Surface

10 cm

20 cm

30 cm

Figure III.10: A detailed view over all particle fluxes on solar activity minimum and maximum at different depths for and input of proton GCR particles.

Depth	Solar minimum	Solar maximum

40 cm

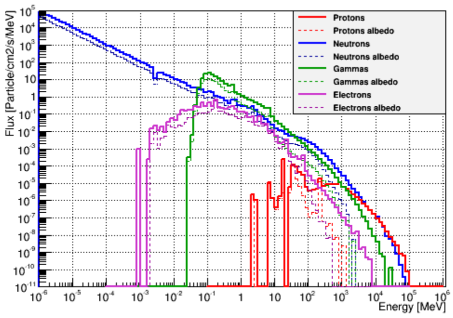

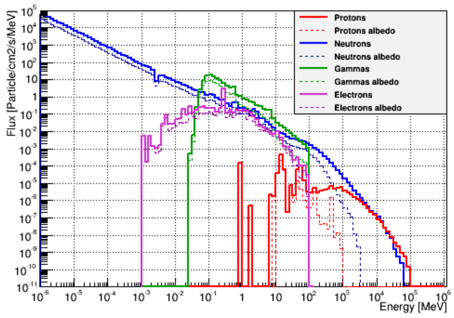

50 cm

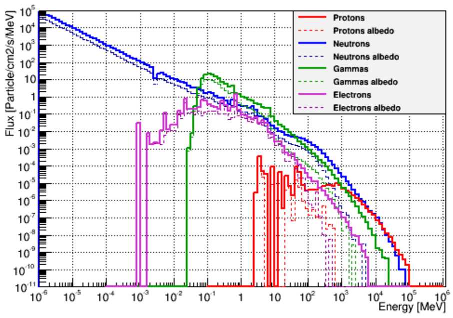

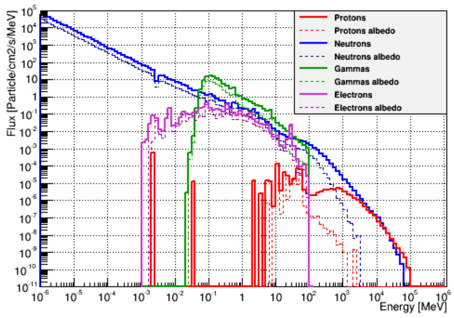

75 cm

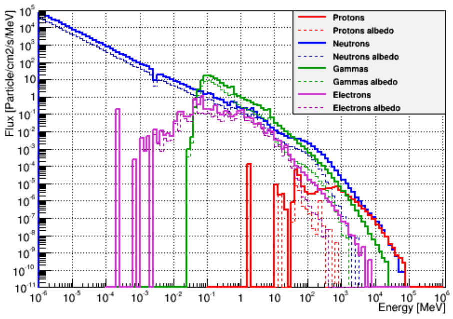

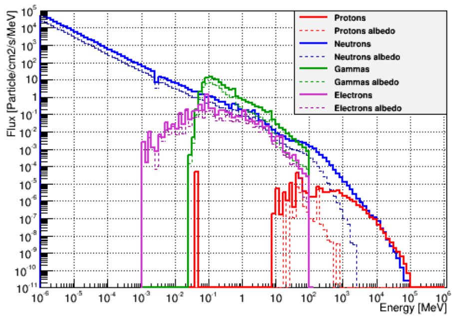

100 cm

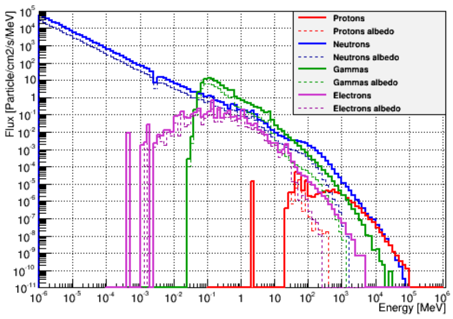

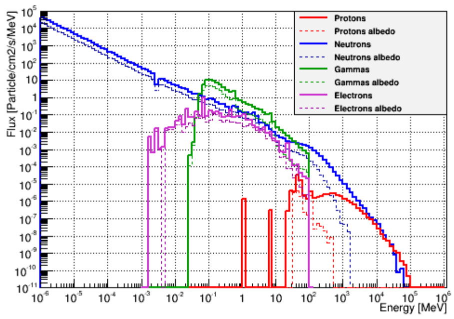

Figure III.11: A detailed view over all particle fluxes on solar activity minimum and maximum at different depths for and input of proton GCR particles.

Depth	Solar minimum	Solar maximum
150 cm	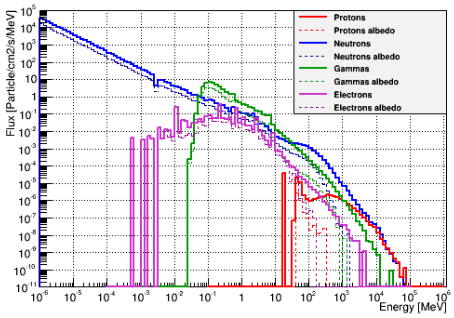	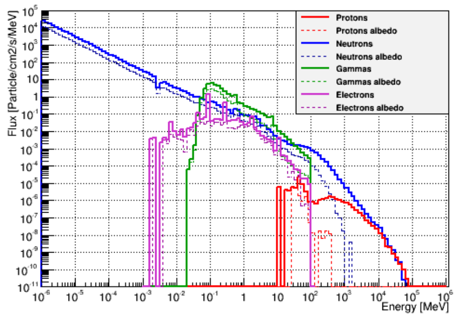
200 cm	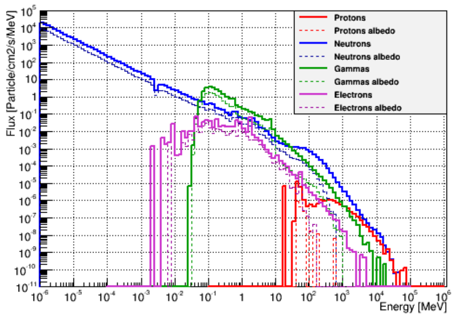	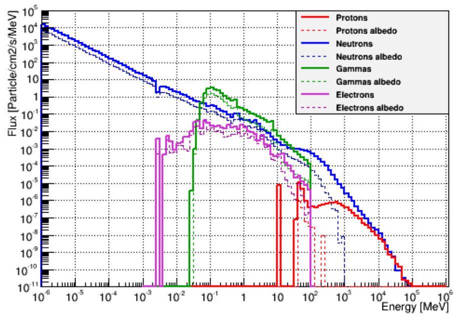
250 cm	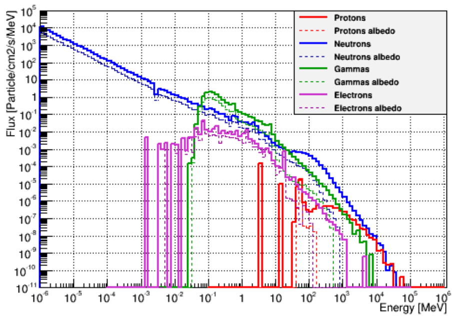	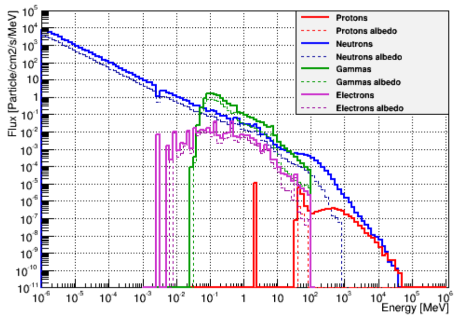
300 cm	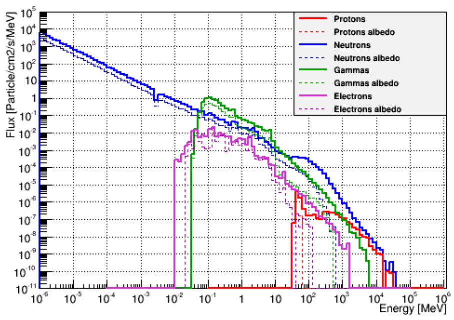	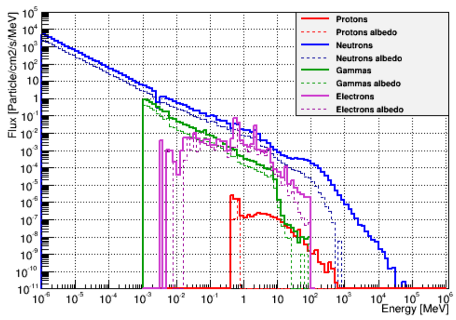

Figure III.12: A detailed view over all particle fluxes on solar activity minimum and maximum at different depths for and input of proton GCR particles.

Alpha particles

A more detailed view of the flux of each secondary particle is shown below.

Depth	Solar minimum	Solar maximum
Surface	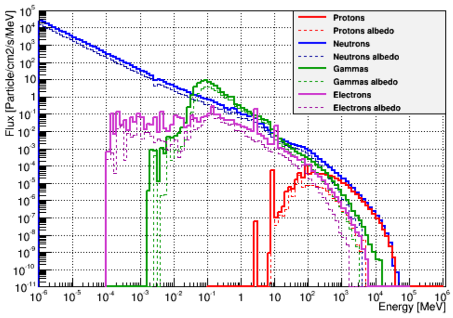	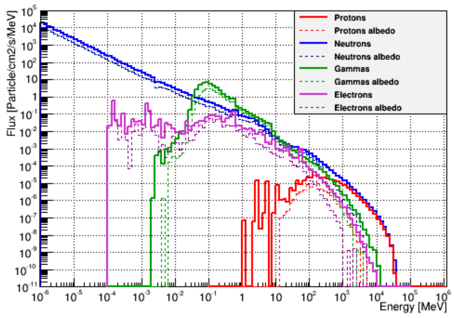
10 cm	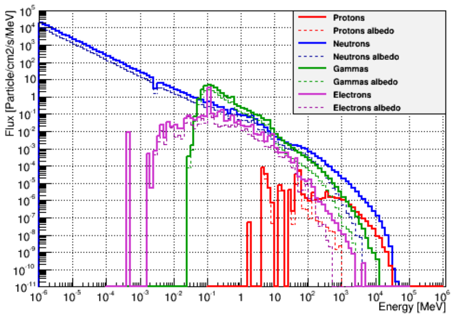	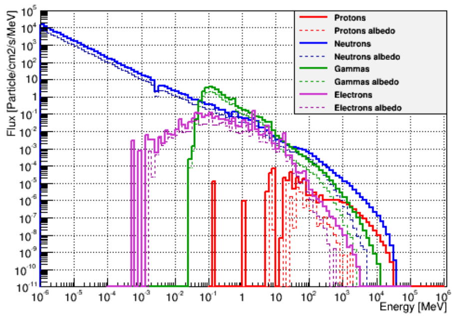
20 cm	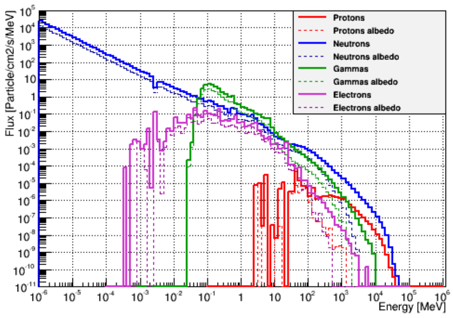	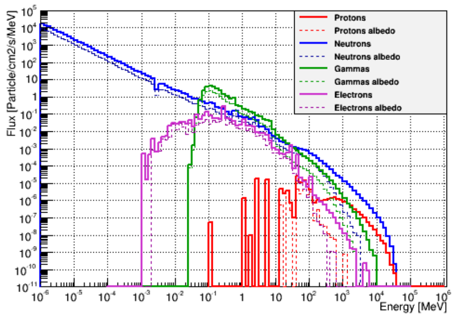
30 cm	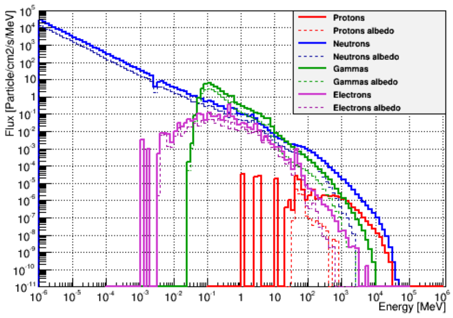	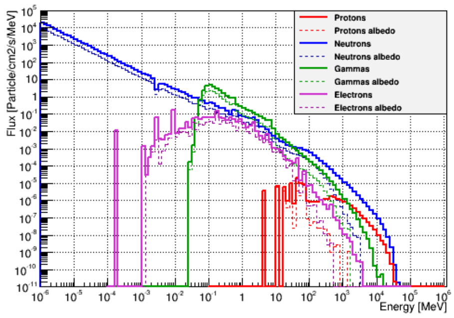

Figure III.13: A detailed view over all particle fluxes on solar activity minimum and maximum at different depths for and input of α GCR particles.

Depth	Solar minimum	Solar maximum
40 cm	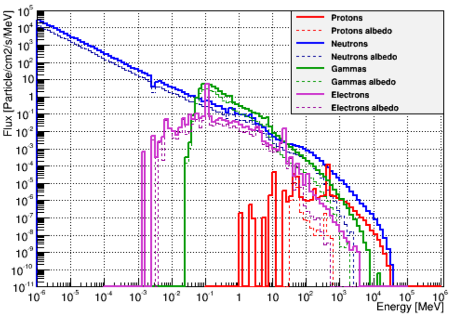	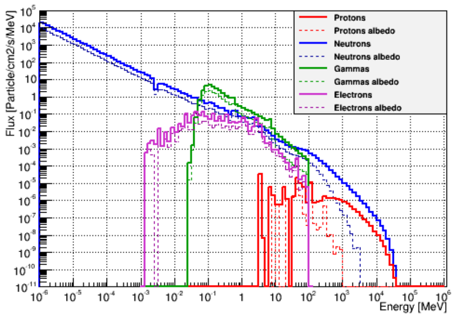
50 cm	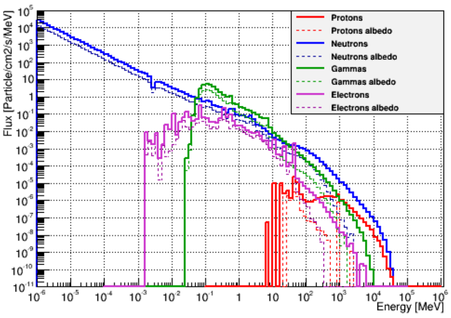	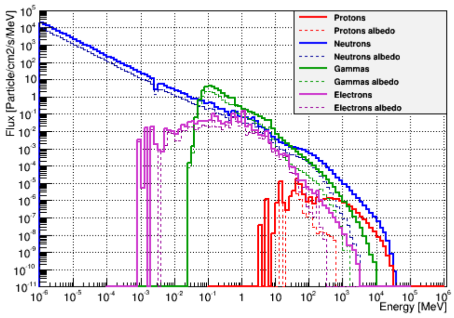
75 cm	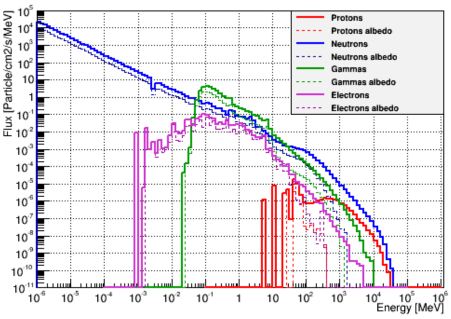	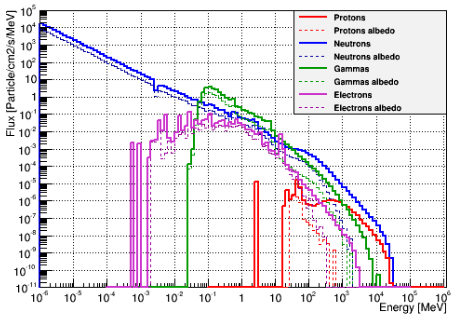
100 cm	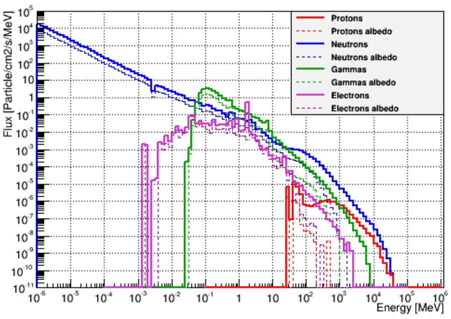	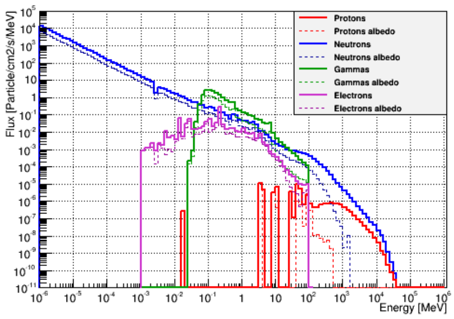

Figure III.14: A detailed view over all particle fluxes on solar activity minimum and maximum at different depths for and input of α GCR particles.

Depth	Solar minimum	Solar maximum
150 cm	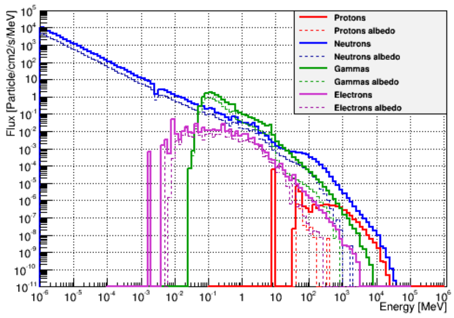	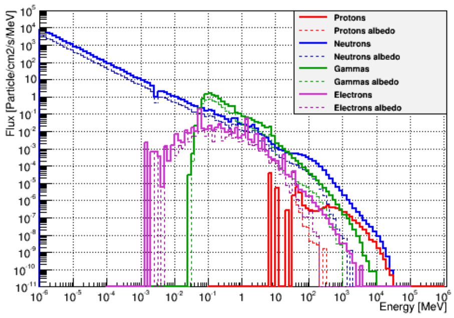
200 cm	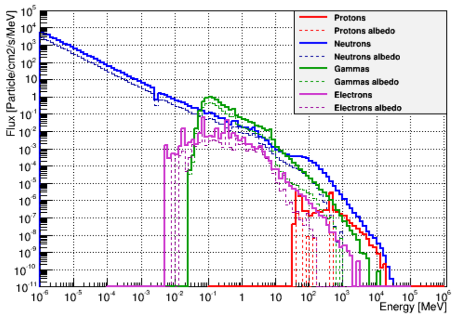	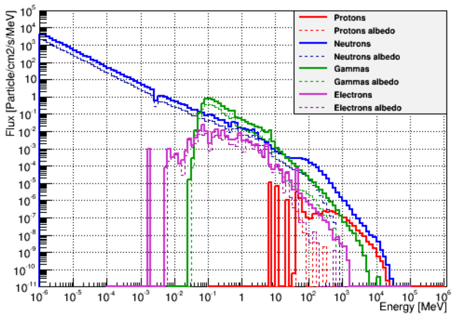
250 cm	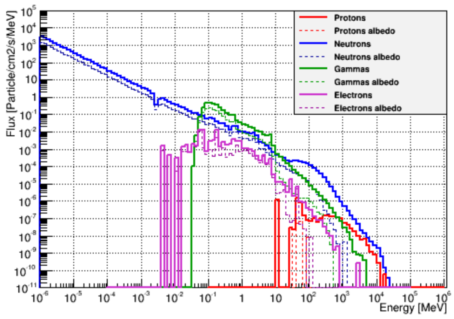	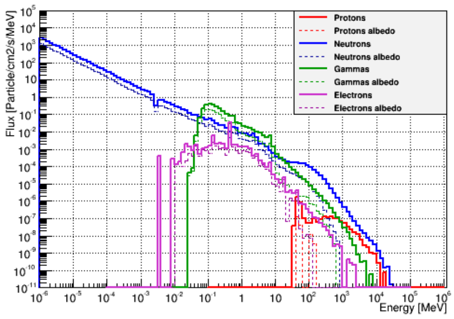
300 cm	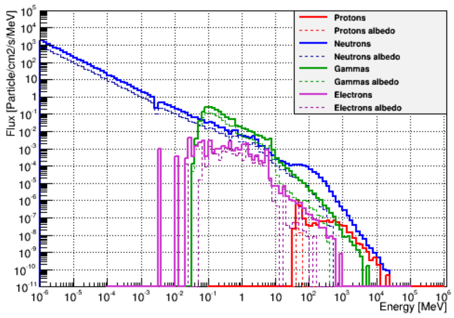	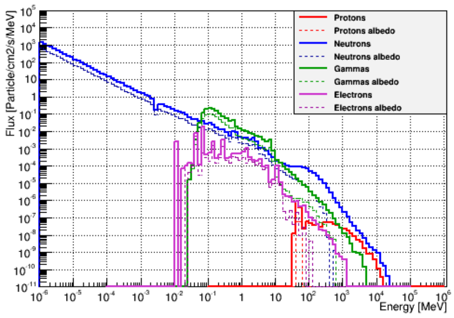

Figure III.15: A detailed view over all particle fluxes on solar activity minimum and maximum at different depths for and input of α GCR particles.

III.1.3 LET

Protons

Observing Figures III.17 and III.18, it can be seen that the greater the LET, the smaller the particle flux. This can be explained because high energy particles deposit less energy in the materials. This is explained by the Bethe-Bloch equation (figure I.14, where the $\beta\gamma$ of the protons generated in this simulation is between 0.15 and 11.62). A decrease of higher LET flux is expected, since as we go deeper into the soil, only the more energetic particles will survive, thus leading to lower LET. Comparing these LET fluxes to the LET in the bone (ICRU) [50], which has a similar density (1.85 g/cm^3) than the soil, we see that the order of magnitude is the same, within the energy range considered, since it goes from 1.85×10^{-3} to 4.2×10^{-2} MeV cm^2/mg, as represented in Figure III.16 (units are MeV cm^2/g, whereas in this thesis MeV cm^2/mg are used).

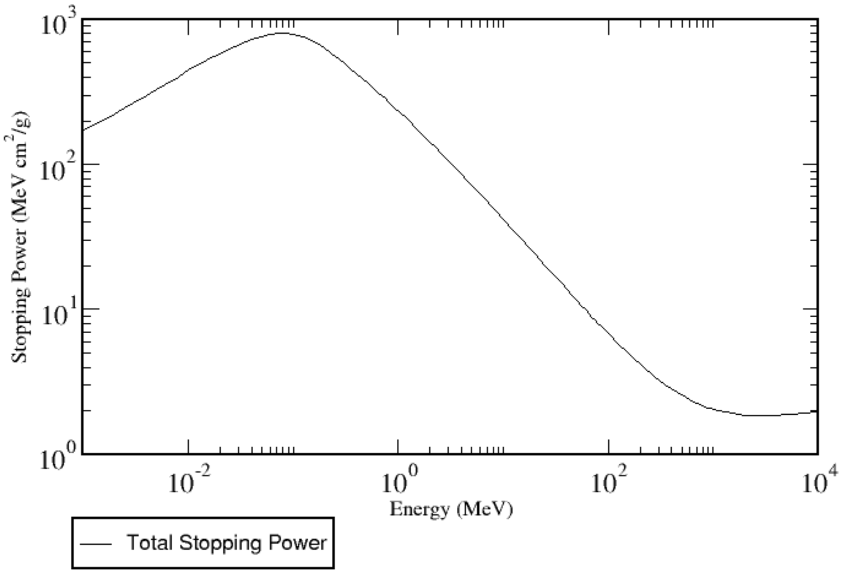

Figure III.16: Total stopping power of protons in bone (ICRU) [50].

To compare these LET values with their respective RBE, one must convert the presented units to keV/μm, which is rather straightforward, and is shown in equation III.1.

$$
\begin{aligned}
& 1\text{MeV cm}^2/\text{mg} \times \rho_{H_2O} = 1\text{MeV cm}^2/\text{mg} \times 10^3\text{mg/cm}^3 = \\
= \; & 10^3\text{MeV/cm} = 100\text{keV}/\mu\text{m} \qquad \text{(III.1)}
\end{aligned}
$$

The worst case LET scenario corresponds to 100 keV/μm (see section I), which corresponds to 1 MeV cm^2/mg. During the solar minimum, as seen in Figures III.17(a) and III.18(a), this value of LET is only reached at the first centimeters below the surface. Although the RBE maximum is reached with LET values of 1 MeV cm^2/mg, RBE starts to increase with LET values from 0.1 MeV cm^2/mg. Despite these flux values being relatively low, they are not negligible down to $\simeq 2$ m underground. At 2,5 m LET barely reaches 0.1 MeV cm^2/mg, so the respective RBE value remains at $\simeq 1$. One must have in mind that

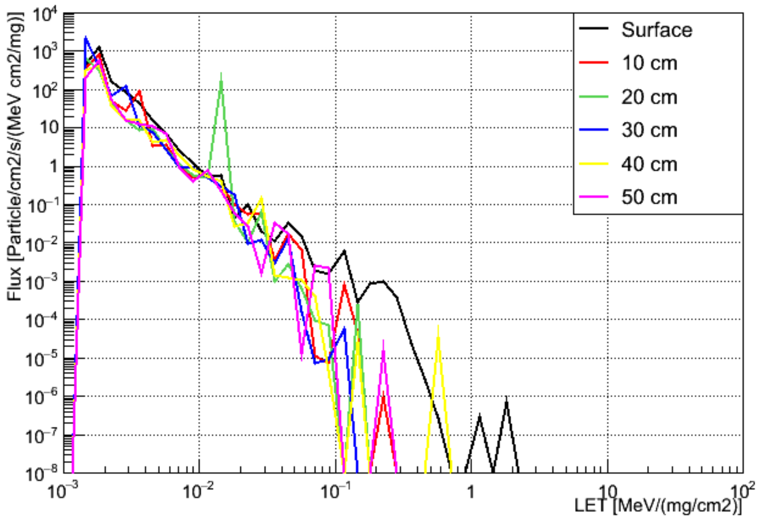

(a)

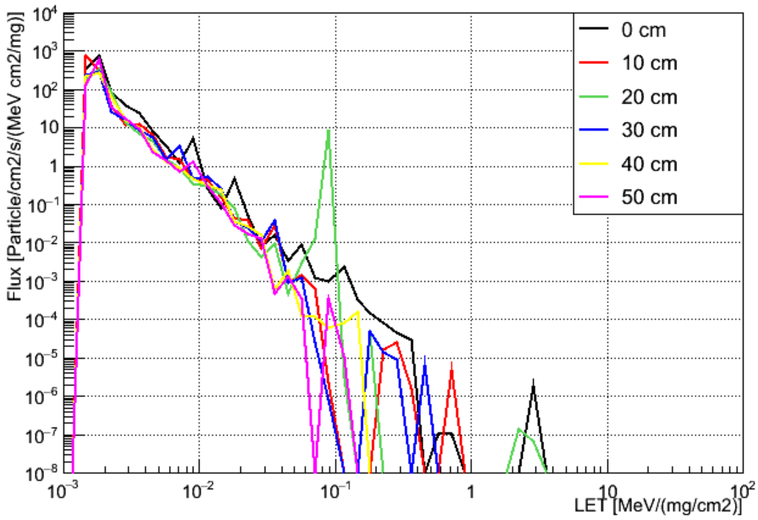

(b)

Figure III.17: LET from the surface to a 50 cm depth, on both solar activity minimum (a) and maximum (b).

since few events were detected in this region, the statistical uncertainty is higher than in the low-LET region where the flux is higher.

During the solar maximum, as seen in Figures III.17(b) and III.18(b), a fall in flux is registered. Both in solar minimum and maximum, the LET flux reaches a maximum at 10^{-3} MeV cm^2/mg, or 0.1 keV/μm (RBE $\simeq 1$), starting to decrease with energy as one would expect according to Curiosity's measurements (I.22).

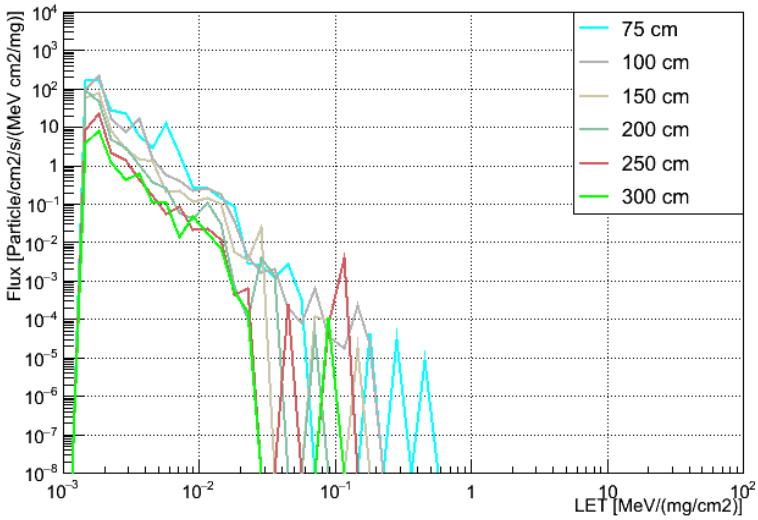

(a)

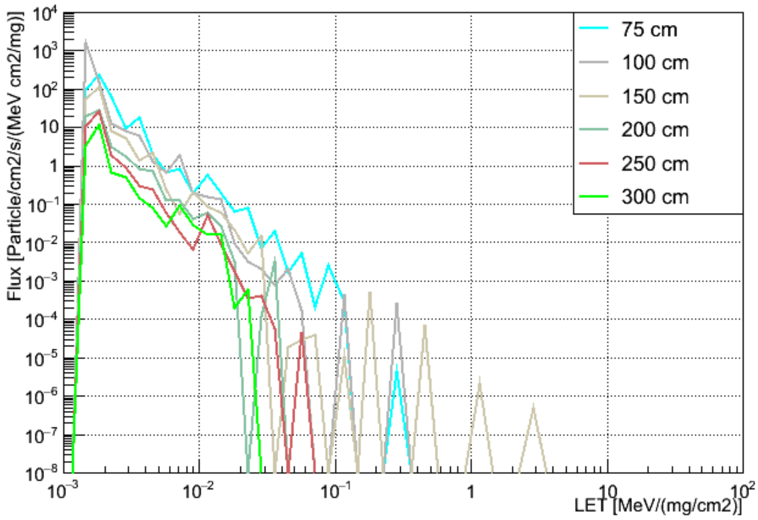

(b)

Figure III.18: LET from a 75 cm to a 3 m depth, on both solar activity minimum (a) and maximum (b).

Alpha particles

Observing Figures III.19 and III.20, and having in mind that RBE starts to increase to higher values for LET values between 0.1 MeV cm^2/mg and $\simeq$1 MeV cm^2/mg, it is possible to conclude that, for both solar activity levels, in the first 2 m of the soil, some occurrences of this hazardous LET were registered. For larger depths, hazardous LET was not detected.

Similarly to protons, a fall in flux is registered for solar activity maximum as well. Comparing these LET values with the proton-like GCR, α particles seem to be less hazardous, since above 10 keV/μm their flux is almost negligible, although, again, one must bear in mind that in this region the statistical uncertainty is higher.

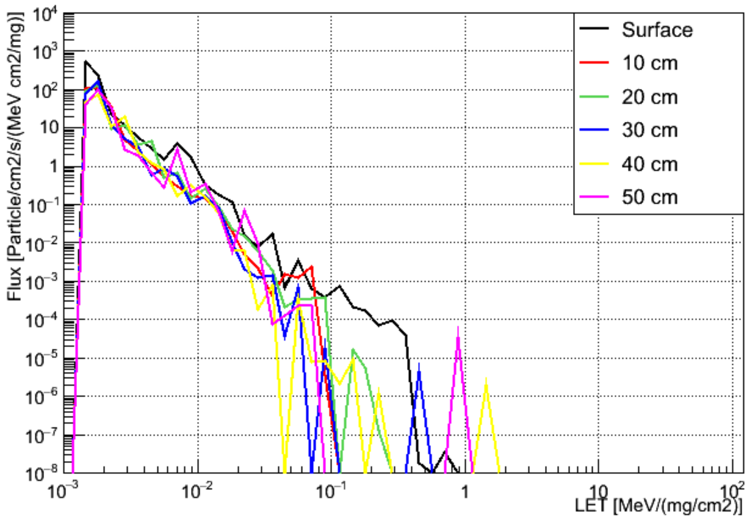

(a)

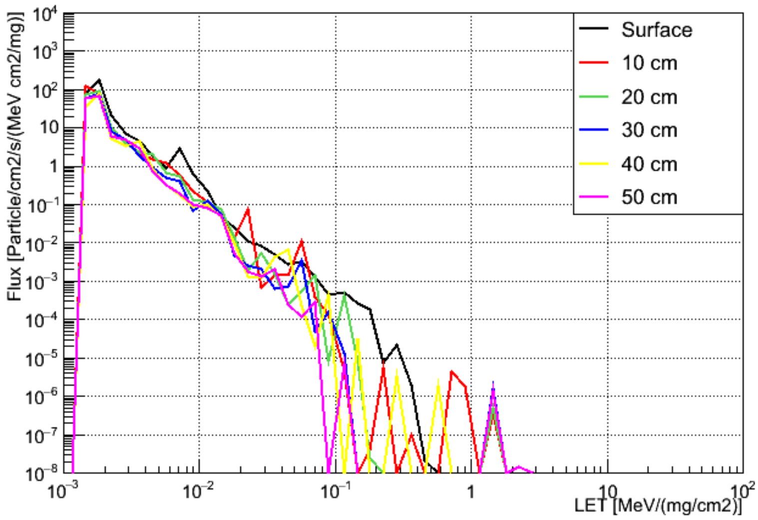

(b)

Figure III.19: LET from the surface to a 50cm depth, on both solar activity minimum (a) and maximum (b).

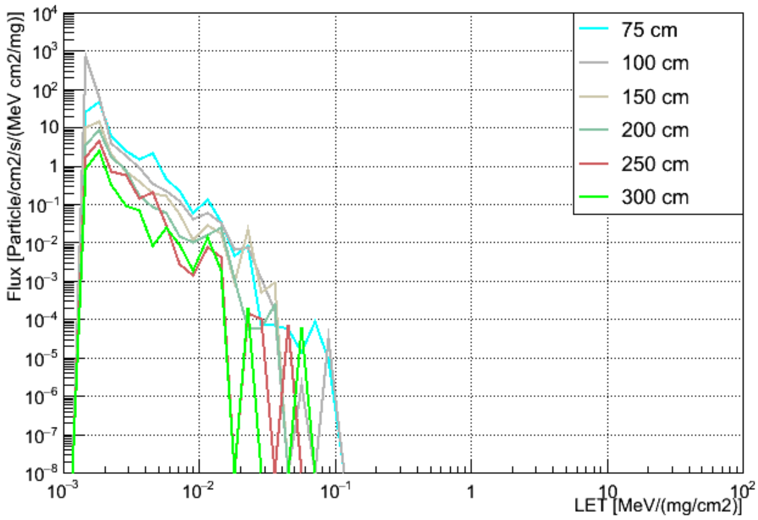

(a)

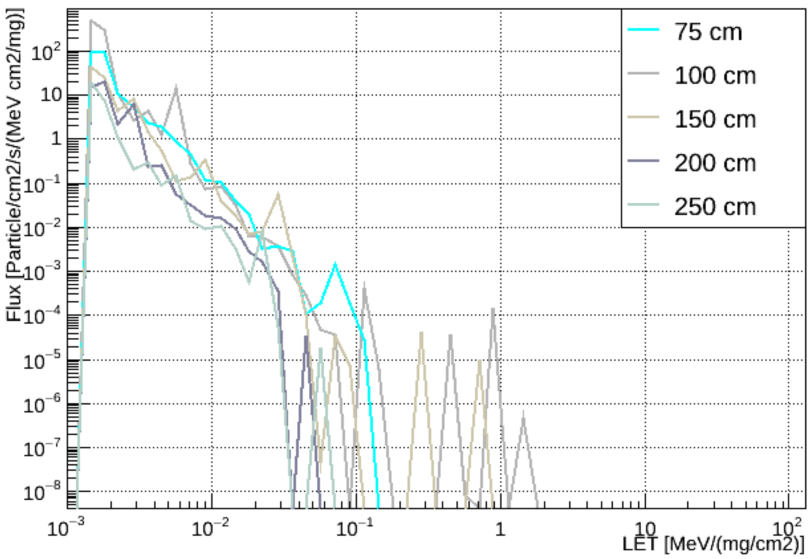

(b)

Figure III.20: LET from a 75 cm to a 3 m, on both solar activity minimum (a) and maximum (b).

Since the relative biologic effectiveness of the LET starts to increase around 10 keV/μm I.20, the urge to integrate all these LET fluxes above this value arises. Table III.4 shows the particles per cm^2 per second ($\times$0,01) as a function of depth, for protons and alpha particles, both at solar minimum and maximum, that were detected above this LET threshold. As expected, the flux decreases with the soil depth and, in general, the contribution due to protons is higher than the contribution due to alpha particles. For the lower centimeters, these fluxes are not negligible, since roughly 8 particles are expected to interact with 1 m^2 at 10 cm below the surface for solar minimum. The statistical uncertainty for the surface values is 18% and for the remaining depths, since the statistics have low significance, their errors are hard to estimate, but shall be around 50% (estimated with available statistics). The values for a 250 cm depth are notoriously too high and are domained by their large statistical uncertainty, thus should

Table III.4: Integrated flux of LET values above 10 keV/μm for all scenarios. The statistical uncertainty for the surface values is 18% and for the remaining depths, since the statistics have low significance, their errors are hard to estimate, but shall be around 50% (estimated with available statistics).

	Solar minimum (particle/cm^2/s $\times$ 0,01)			Solar maximum (particle/cm^2/s $\times$ 0,01)		
Depth (cm)	$\text{Flux}_{\text{Protons}}$	$\text{Flux}_{\text{Alphas}}$	Total	$\text{Flux}_{\text{Protons}}$	$\text{Flux}_{\text{Alphas}}$	Total
0	0,88	0,13	1,01	0,31	0,10	0,41
10	0,08	0	0,08	0,01	0	0,01
20	0,02	0	0,03	0,01	0,04	0,05
30	0,01	0	0,01	0,01	0	0,01
40	0,01	0	0,01	0,02	0	0,03
50	0	0	0,01	0	0	0
75	0,01	0	0	0,03	0,03	0,06
100	0,03	0	0,02	0,07	0	0,07
150	0	0	0	0,06	0	0,06
200	0	0	0	0	0	0
250	$<$0,4033	0	$<$0,4033	0	0	0
300	0	0	0	0	0	0

clearly be closer to zero. The SEP are not presented in this table since almost no occurrence of LET above the referred threshold was detected, as can be seen in the next section.

III.2 SEP

The input spectrum is presented in figure III.21.

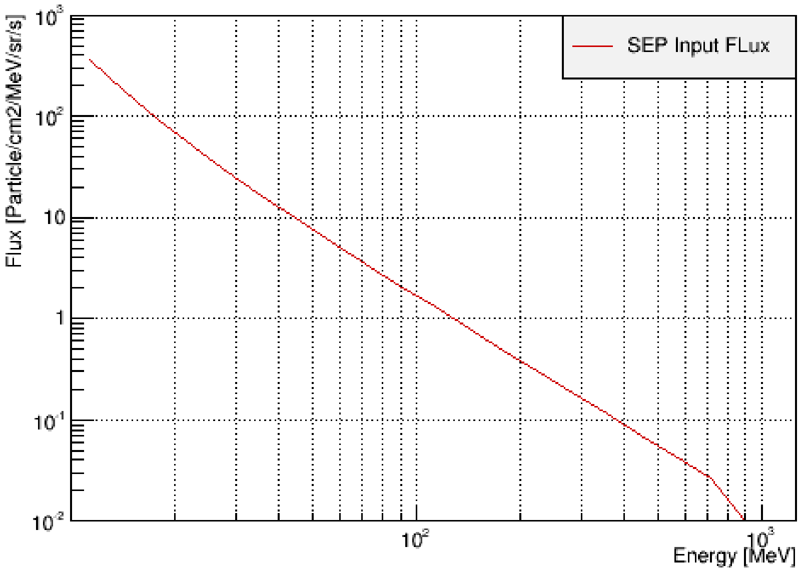

Figure III.21: SEP energy spectrum.

III.2.1 Primary and secondary particles

Observing Figure III.23(a), one concludes that after 50 cm of soil depth almost no SEP events are detected, and after 1 m no event is detected. Looking at the full particle spectrum at the surface, Figure III.22(b), it can be seen that the neutron flux remains dominant until $\simeq$ 10 keV, giving rise to the formation of γ. Although in a less dominant way, electrons are also formed, being responsible for the formation of that γ radiation. The flux at all studied depths are in section A.3.

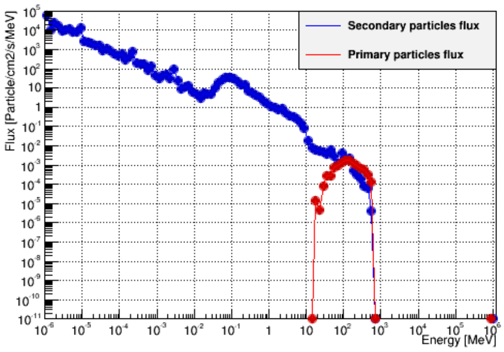

(a)

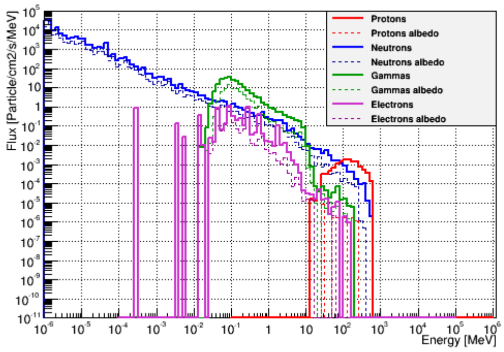

(b)

Figure III.22: Primary and secondary particle flux (a) and all particles' flux (b), both at the surface.

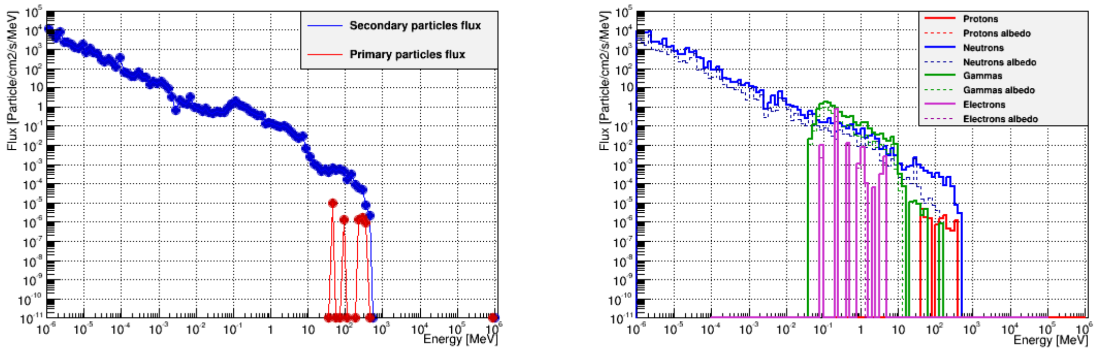

(a) (b)

Figure III.23: Primary and secondary particle flux (a) and all particles' flux (b), both at 50 cm deep.

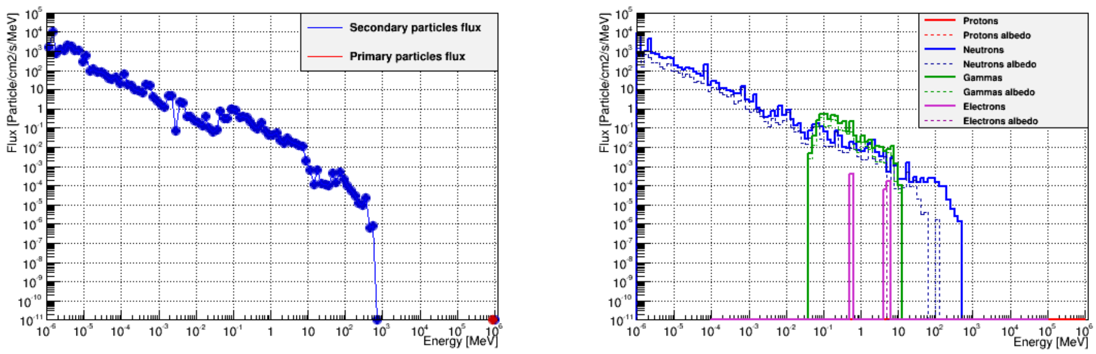

(a) (b)

Figure III.24: Primary and secondary particle flux (a) and all particles' flux (b), both at 1 m deep.

III.2.2 LET

Observing Figure III.25(a), which correspond to the first 50 cm of the soil depth, and comparing it to the LET of protons or α particles, whether on solar maximum or minimum, one concludes that SEP events have few impact or no impact at medium-high LET, since it only reaches 0.1 MeV cm^2/mg (10 keV/μm) at the surface. Underground, its values are below 0.02 MeV cm^2/mg. Looking at figure Figure III.25(b), one sees that up to 2 m deep, no traces of LET are detected. Only a depth of 200 cm is shown because at the last two layers (250 and 300 cm) no LET was measured.

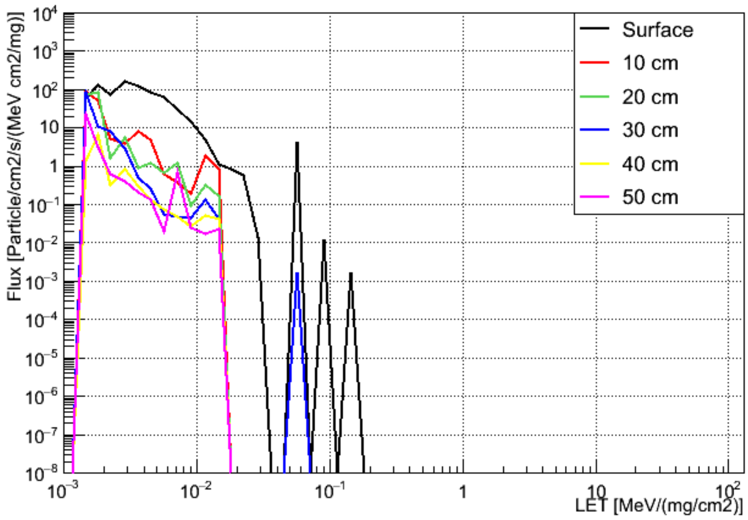

(a)

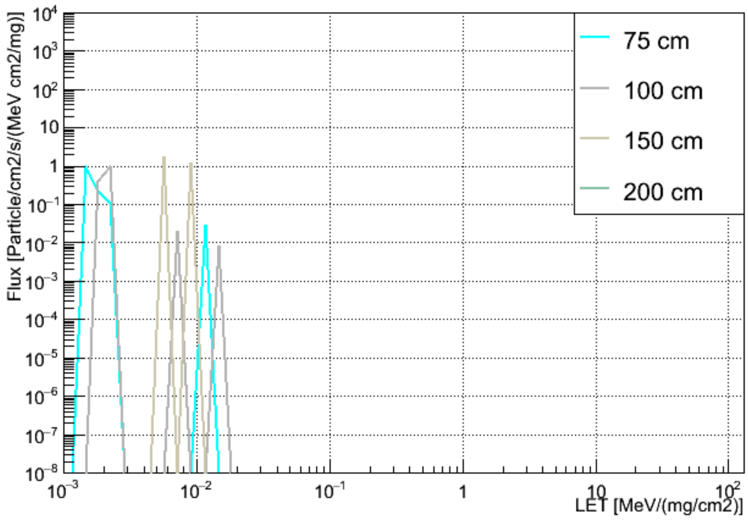

(b)

Figure III.25: LET due to solar event particles at different soil depths.

III.3 Validation with Curiosity

Curiosity's LET measurements constitute the state of the art of the Martian surface LET, presented in figure III.26. In order to compare this spectrum with dMEREM's proton and alpha spectra added, one

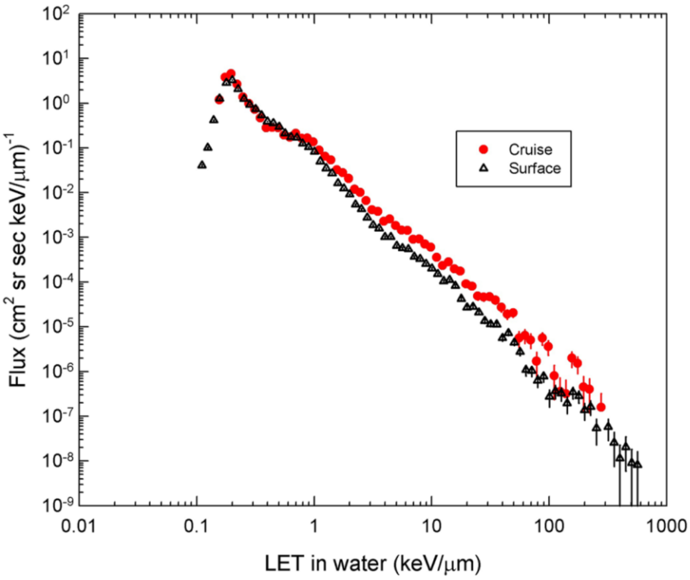

Figure III.26: LET spectrum comparison between the measurement during the cruise journey inside the MSL spacecraft (red) and the surface of Mars (black).

must convert the presented flux units into the units used in this thesis, which is given by equation III.2. So, a factor of 34.56 π must be applied to the last figure in order to be compatible with this thesis.

$$
\begin{aligned}
& 1 \text{ cm}^{-2} \text{ s}^{-1} \text{ keV}^{-1} \text{ sr}^{-1} \ \mu\text{m} = 10^3 \text{ cm}^{-2} \text{ s}^{-1} \text{ MeV}^{-1} \text{ sr}^{-1} \ \mu\text{m} = \\
= \ & 10^3 \text{ cm}^{-2} \text{ s}^{-1} \text{ MeV}^{-1} \ \mu\text{m sr}^{-1} 10^3 \text{ mg cm}^{-3} = 10^2 \text{ cm}^{-2} \text{ s}^{-1} \text{ MeV}^{-1} \text{ cm}^{-2} \text{ mg sr}^{-1} = \\
= \ & 0,1681 \times 100 \text{ cm}^{-2} \text{ s}^{-1} \text{ MeV}^{-1} \text{ cm}^{-2} \text{ mg} \qquad \text{(III.2)}
\end{aligned}
$$

Figure III.27 shows both spectra superimposed in the same graph. In both cases the flux spans across the same LET values, and the flux measured by Curiosity is similar to the one computed by dMEREM, apart from the greater values. As mentioned earlier, in this regime few events were detected, meaning that the statistical uncertainty becomes higher, explaining the divergence in these high-LET results. In this thesis only protons and alpha particles were simulated. Other elements like Carbon and Oxygen are known for having a non-negligible contribution to the LET. Curiosity's detector's amplitude is smaller, since the geometry factor is 0,17 cm^{2}sr [51] with an area of 1,92 cm^2 [14], corresponding to a half field of view (FOV) angle of only 9,63° (0,1681 rad). Whereas in the case of this thesis, the simulated half FOV is 90°. Since the flux depends on $\cos^2(\theta)$, with θ being the particle's incident angle measured from the vertical, the flux computed by dMEREM is lower than it would have been if computed with the same FOV as Curiosity, since larger angles are taken into account. The computed LET values seem to be compatible with the ones measured by Curiosity, except for the low LET region.

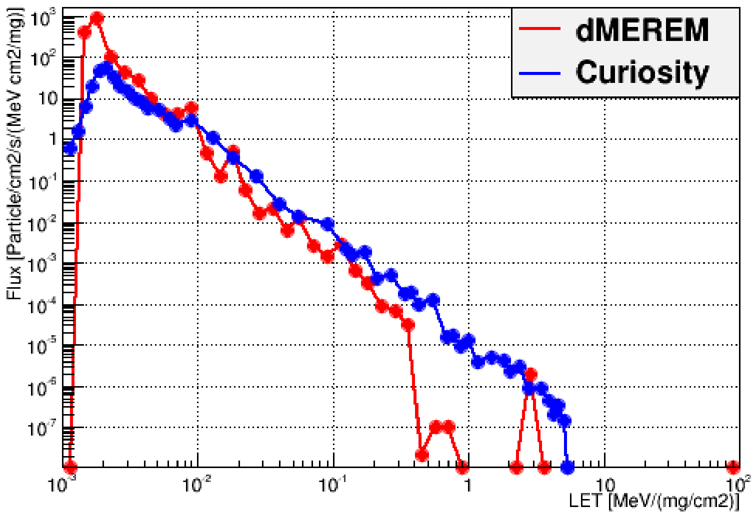

Figure III.27: Comparison of Curiosity's in situ LET spectrum measurements with the one computed by dMEREM.

Chapter IV

Conclusions

Clearly the best approach for avoiding radiation damage in a cell is to avoid that damage in the first place, hence the evolution of UV-absorbing pigment in the human skin, acting as a defense against UV damage. In the GCR case, it is possible to conclude that the protons travel farther into the Martian soil than the α particles, for the latter cease after 150 cm of regolith soil. This is somewhat expected due to their higher charge, since, according to Bethe-Bloch formula (equation I.5), they will lose more energy per unit length, which is corroborated by the increase in LET.

The damage in biologic materials increases with the RBE, which increases with LET from values bigger than 10 keV/μm, or 0.1 MeV cm^2/mg, according to figure I.20, in section I. According to table III.4, non-hazardous LET is reached at $\simeq$ 150 cm depths, in the case of protons and α particles, for both solar minimum and maximum. Although the low LET particles are associated with low RBE and cause little damage to the DNA, their fluxes are much higher than in the last case, going up to roughly 6 orders of magnitude over the flux registered at 10 keV/μm.

The SEP are quickly absorbed in the Martian soil, which is somewhat expected due to their low energies, when compared to the GCR. Even at the surface, the LET barely reaches the hazardous region.

The Curiosity results for the measured LET are in reasonable agreement with the ones presented in this thesis for the LET at the surface of Mars. However, there are discrepancies to be understood that may be related to the acceptance of the real detector being smaller than the simulated one (covering only a specific part of the angular distribution of the particle arriving the surface) and also the fact that in this work only protons and α particles were simulated, while heavier ions reaching the Martian surface would contribute to the higher LET region. These differences should be better understood in a future analysis.

Bibliography

[1] URL https://astrobiology.nasa.gov/about-astrobiology.

[2] URL https://geant4.web.cern.ch/geant4/.

[3] URL https://commons.wikimedia.org/wiki/File:DAGATA-Detektor_Monte_Carlo_Simulation_with_Geant4.png.

[4] URL http://www.space.com/16385-curiosity-rover-mars-science-laboratory.html.

[5] URL http://planetarynames.wr.usgs.gov/nomenclature/Feature/2071.

[6] . URL http://exploration.esa.int/mars/46048-programme-overview/.

[7] . URL http://exploration.esa.int/mars/47852-entry-descent-and-landing-demonstrator-module/.

[8] G. Gronoff et al. Computation of cosmic ray ionization and dose at mars. i: A comparison of HZETRN and planetocosmics for proton and alpha particles. *Space Research*, 55:7:1799–1805, 2015. doi: 10.1016/j.asr.2015.01.028.

[9] Ralf Moeller et al. Journal of the ICRU, vol 10 no 2. *Oxford University Press*, 2010. doi: 10.1093/jicru/ndq019.

[10] C. Baumstark-Khan and R. Facius. *17- Life under Conditions of Ionizing Radiation.*

[11] National Research Council of the National Academies. *Managing Space Radiation Risk in the New Era of Space Exploration.* National Academies Press, Washington D.C.

[12] P. Gonçalves et al. Overview of energetic particle hazards during prospective manned missions to mars. *Planetary and Space Science*, 63-64, 2011.

[13] P. Gonçalves et al. Characterization of the particle radiation environment at three potential landing sites on mars using esa's merem models. *Icarus*, 218:723–734, March 2011. doi: 10.1016/j.icarus.2011.04.004.

[14] Hassler et al. Mars' surface radiation environment measured with the mars science laboratory's curiosity rover. *Science*, 2013. ISSN 0036-8075. doi: 10.1126/science.1244797. URL http://science.sciencemag.org/content/early/2013/12/05/science.1244797.

[15] R.G. Harrison et al. Vertical profile measurements of lower troposphere ionisation. *Journal of Atmospheric and Solar-Terrestrial Physics*, 119:203–210, 2014. doi: 10.1016/j.jastp.2014.08.006.

[16] Edward W. Cliver. History of research on solar energetic particle (SEP) events: the evolving paradigm. *International Astronomical Union*, (257), 2009. doi: 10.1017/S1743921309029639.

[17] J.A. Sinclair et al. On the detectability of trace chemical species in the martian atmosphere using gas correlation filter radiometry. *Icarus*, 260, 2015.

[18] URL `http://nssdc.gsfc.nasa.gov/planetary/factsheet/marsfact.html`.

[19] Donald M. Hassler et al. Mars' surface radiation environment measured with the mars science laboratory's curiosity rover. *Science*, 343, 2014.

[20] G. De Angelisa et al. Modeling of the martian environment for radiation analysis. *Radiation Measurements*, 41, 2006.

[21] Larry G. Evans et al. Background lines in the mars odyssey 2001 gamma-ray detector. *SPIE*, 4784, January 2003. doi: 10.1117/12.455976.

[22] C. G. Tate et al. Water equivalent hydrogen estimates from the first 200 sols of Curiosity's traverse (Bradbury Landing to Yellowknife Bay): Results from the Dynamic Albedo of Neutrons (DAN) passive mode experiment. *Icarus*, 262:102–123, December 2015. doi: 10.1016/j.icarus.2015.09.002.

[23] URL `http://grs.lpl.arizona.edu/specials/Published_Maps_2008_with_Logos/`.

[24] C. Hardgrove et al. Effects of geochemical composition on neutron die-away measurements: Implications for mars science laboratory's dynamic albedo of neutrons experiment. *Nuclear Instruments and Methods in Physics Research Section A: Accelerators, Spectrometers, Detectors and Associated Equipment*, pages 442–455, 2011. doi: 10.1016/j.nima.2011.08.058.

[25] URL `http://mars.nasa.gov/allaboutmars/extreme/moons/`.

[26] Pascal Rosenblatt. The origin of the martian moons revisited. *The Astronomy and Astrophysics Review*, 19(1):1–26, 2011. ISSN 1432-0754. doi: 10.1007/s00159-011-0044-6. URL `http://dx.doi.org/10.1007/s00159-011-0044-6`.

[27] J. M. Ward A. J. Coates R. Dartnell, L. Desorgher. Modelling the surface and subsurface martian radiation environment: Implications for astrobiology. 2007. doi: 10.1029/2006GL027494.

[28] URL `https://www.euronuclear.org/info/encyclopedia/r/radiation-weight-factor.htm`.

[29] URL `https://www.euronuclear.org/info/encyclopedia/t/tissue-weight-factor.htm`.

[30] Patrícia Gonçalves et al. The MARSREM Project: Mars radiation environment models and active shielding studies for interplanetary missions.

[31] URL `https://www.euronuclear.org/info/encyclopedia/ambientdose.htm`.

[32] Fontenot et al. Ambient dose equivalent versus effective dose for quantifying stray radiation exposures to a patient receiving proton therapy for prostate cancer. *Nucl Technol*, 2009.

[33] URL `http://mars.nasa.gov/msl/mission/instruments/radiationdetectors/rad/`.

[34] Groom et al. Muon stopping power and range tables 10-MeV to 100-TeV. *Atom. Data Nucl. Data Tabl.*, 78:183–356, 2001. doi: 10.1006/adnd.2001.0861.

[35] US Nuclear Regulatory Commission, editor. *9 - Biological effects of radiation.*

[36] S. Jorge et al. Evidence of DNA double strand breaks formation in *Escherichia coli* bacteria exposed to alpha particles of different LET assessed by the SOS response. *Applied Radiation and Isotopes*, 71:66–70, December 2012. doi: 10.1016/j.apradiso.2012.05.007.

[37] R. Taleei et al. DSB repair model for mammalian cells in early S and G1 phases of the cell cycle: Application to damage induced by ionizing radiation of different quality. *Mutation Research/Genetic Toxicology and Environmental Mutagenesis*, 779:5–14, 2015. doi: 10.1016/j.mrgentox.2015.01.007.

[38] J. Karschau et al. A matter of life or death: Modeling DNA damage and repair in bacteria. *Biophysical Journal*, 100:814–821, February 2011. doi: 10.1016/j.bpj.2010.12.3713.

[39] URL `https://www.nobelprize.org/nobel_prizes/chemistry/laureates/2015/fig_ke_en_15_baseexcisionrepair.pdf`.

[40] C. Arena et al. Space radiation effects on plant and mammalian cells. *Acta Astronautica*, 104: 419–431, November 2014. doi: 10.1016/j.actaastro.2014.05.005.

[41] S. Moore et al. The repair of environmentally relevant DNA double strand breaks caused by high linear energy transfer irradiation - no simple task. *DNA Repair*, 17:64.73, May 2014. doi: 10.1016/j.dnarep.2014.01.014.

[42] Amato J Giaccia Eric J Hall. *Radiobiology for the radiologist.*

[43] Barendsen. Response of cultured cells, tumours and normal tissues to radiations of different linear energy transfer. *Curr Top Radiat*, 1968.

[44] Ralf Moeller et al. Astrobiological aspects of the mutagenesis of cosmic radiation on bacterial spores. *Astrobiology*, 10(5):509–521, June 2010. doi: 10.1089/ast.2009.0429.

[45] Richard William Harbron. Cancer risks from low dose exposure to ionising radiation: Is the linear no-threshold model still relevant? *Radiography*, 2011.

[46] URL `https://www.spenvis.oma.be/`.

[47] URL `https://geant4.web.cern.ch/geant4/UserDocumentation/UsersGuides/ForApplicationDeveloper`.

[48] URL `http://physics.nist.gov/PhysRefData/Star/Text/PSTAR.html`.

[49] URL `http://mars.nasa.gov/odyssey/mission/instruments/grs/`.

[50] URL `http://physics.nist.gov/PhysRefData/Star/Text/PSTAR.html`.

[51] B Ehresmann et al. Charged particle spectra obtained with the Mars Science Laboratory Radiation Assessment Detector (MSL/RAD) on the surface of Mars. *Journal of Geophysical Research*, pages 468–479, 2014. doi: 10.1002/2013JE004547.

[52] M.A. Shea D.F. Smart. *6- Galactic cosmic radiation and solar energetic particles.* Air Force Geophysical Laboratory.

Appendix A

Appendix

A.1 Input flux

A.1.1 GCR

protons

Energy (MeV)	part/cm^2/MeV/sr/s
0.1130 $\times 10^2$	0.7787 $\times 10^{-5}$
0.1422 $\times 10^2$	0.1091 $\times 10^{-4}$
0.1790 $\times 10^2$	0.1501 $\times 10^{-4}$
0.2254 $\times 10^2$	0.2028 $\times 10^{-4}$
0.2837 $\times 10^2$	0.2688 $\times 10^{-4}$
0.3572 $\times 10^2$	0.3494 $\times 10^{-4}$
0.4497 $\times 10^2$	0.4448 $\times 10^{-4}$
0.5661 $\times 10^2$	0.5549 $\times 10^{-4}$
0.7126 $\times 10^2$	0.6779 $\times 10^{-4}$
0.8972 $\times 10^2$	0.8111 $\times 10^{-4}$
0.1129 $\times 10^3$	0.9506 $\times 10^{-4}$
0.1422 $\times 10^3$	0.1091 $\times 10^{-3}$
0.1790 $\times 10^3$	0.1225 $\times 10^{-3}$
0.2254 $\times 10^3$	0.1343 $\times 10^{-3}$
0.2837 $\times 10^3$	0.1434 $\times 10^{-3}$
0.3572 $\times 10^3$	0.1485 $\times 10^{-3}$
0.4496 $\times 10^3$	0.1485 $\times 10^{-3}$
0.5661 $\times 10^3$	0.1425 $\times 10^{-3}$
0.7126 $\times 10^3$	0.1307 $\times 10^{-3}$
0.8972 $\times 10^3$	0.1142 $\times 10^{-3}$
0.1130 $\times 10^4$	0.9497 $\times 10^{-4}$
0.1422 $\times 10^4$	0.7516 $\times 10^{-4}$
0.1790 $\times 10^4$	0.5674 $\times 10^{-4}$
0.2254 $\times 10^4$	0.4099 $\times 10^{-4}$
0.2837 $\times 10^4$	0.2843 $\times 10^{-4}$
0.3572 $\times 10^4$	0.1899 $\times 10^{-4}$
0.4496 $\times 10^4$	0.1226 $\times 10^{-4}$
0.5661 $\times 10^4$	0.7684 $\times 10^{-5}$
0.7126 $\times 10^4$	0.4686 $\times 10^{-5}$
0.8972 $\times 10^4$	0.2792 $\times 10^{-5}$
0.1130 $\times 10^5$	0.1631 $\times 10^{-5}$
0.1422 $\times 10^5$	0.9364 $\times 10^{-6}$
0.1790 $\times 10^5$	0.5301 $\times 10^{-6}$
0.2254 $\times 10^5$	0.2966 $\times 10^{-6}$
0.2837 $\times 10^5$	0.1644 $\times 10^{-6}$
0.3572 $\times 10^5$	0.9036 $\times 10^{-7}$
0.4496 $\times 10^5$	0.4936 $\times 10^{-7}$
0.5661 $\times 10^5$	0.2682 $\times 10^{-7}$
0.7126 $\times 10^5$	0.1451 $\times 10^{-7}$
0.8972 $\times 10^5$	0.7826 $\times 10^{-8}$

Table A.1: proton-like GCR input fluxes as function of the kinetic energy, on solar activity minimum.

Energy (MeV)	part/cm^2/MeV/sr/s
1.1295 $\times 10^1$	4.8685 $\times 10^{-7}$
1.4219 $\times 10^1$	7.4675 $\times 10^{-7}$
1.7901 $\times 10^1$	1.1334 $\times 10^{-6}$
2.2536 $\times 10^1$	1.7004 $\times 10^{-6}$
2.8371 $\times 10^1$	2.5191 $\times 10^{-6}$
3.5717 $\times 10^1$	3.6803 $\times 10^{-6}$
4.4965 $\times 10^1$	5.2948 $\times 10^{-6}$
5.6607 $\times 10^1$	7.4891 $\times 10^{-6}$
7.1264 $\times 10^1$	1.0394 $\times 10^{-5}$
8.9716 $\times 10^1$	1.4124 $\times 10^{-5}$
1.1295 $\times 10^2$	1.8741 $\times 10^{-5}$
1.4219 $\times 10^2$	2.4215 $\times 10^{-5}$
1.7901 $\times 10^2$	3.0365 $\times 10^{-5}$
2.2536 $\times 10^2$	3.6827 $\times 10^{-5}$
2.8371 $\times 10^2$	4.3045 $\times 10^{-5}$
3.5717 $\times 10^2$	4.8328 $\times 10^{-5}$
4.4965 $\times 10^2$	5.1965 $\times 10^{-5}$
5.6607 $\times 10^2$	5.3393 $\times 10^{-5}$
7.1264 $\times 10^2$	5.2351 $\times 10^{-5}$
8.9716 $\times 10^2$	4.8956 $\times 10^{-5}$
1.1295 $\times 10^3$	4.3675 $\times 10^{-5}$
1.4219 $\times 10^3$	3.7203 $\times 10^{-5}$
1.7901 $\times 10^3$	3.0292 $\times 10^{-5}$
2.2536 $\times 10^3$	2.3604 $\times 10^{-5}$
2.8371 $\times 10^3$	1.7622 $\times 10^{-5}$
3.5717 $\times 10^3$	1.2622 $\times 10^{-5}$
4.4965 $\times 10^3$	8.6877 $\times 10^{-6}$
5.6607 $\times 10^3$	5.7608 $\times 10^{-6}$
7.1264 $\times 10^3$	3.6918 $\times 10^{-6}$
8.9716 $\times 10^3$	2.2949 $\times 10^{-6}$
1.1295 $\times 10^4$	1.3891 $\times 10^{-6}$
1.4219 $\times 10^4$	8.2190 $\times 10^{-7}$
1.7901 $\times 10^4$	4.7699 $\times 10^{-7}$
2.2536 $\times 10^4$	2.7238 $\times 10^{-7}$
2.8371 $\times 10^4$	1.5347 $\times 10^{-7}$
3.5717 $\times 10^4$	8.5520 $\times 10^{-8}$
4.4965 $\times 10^4$	4.7228 $\times 10^{-8}$
5.6607 $\times 10^4$	2.5891 $\times 10^{-8}$
7.1264 $\times 10^4$	1.4110 $\times 10^{-8}$
8.9716 $\times 10^4$	7.6526 $\times 10^{-9}$
1.1295 $\times 10^5$	4.1346 $\times 10^{-9}$
1.4219 $\times 10^5$	2.2270 $\times 10^{-9}$
1.7901 $\times 10^5$	1.1965 $\times 10^{-9}$
2.2536 $\times 10^5$	6.4162 $\times 10^{-10}$
2.8371 $\times 10^5$	3.4351 $\times 10^{-10}$
3.5717 $\times 10^5$	1.8368 $\times 10^{-10}$
4.4965 $\times 10^5$	9.8120 $\times 10^{-11}$
5.6607 $\times 10^5$	5.2372 $\times 10^{-11}$
7.1264 $\times 10^5$	2.7936 $\times 10^{-11}$
8.9716 $\times 10^5$	1.4894 $\times 10^{-11}$

Table A.2: proton-like GCR input fluxes as function of the kinetic energy, on solar activity maximum.

Alpha

Energy (MeV)	part/cm^2/MeV/sr/s
1.1295 $\times 10^{1}$	1.3576 $\times 10^{-7}$
1.4219 $\times 10^{1}$	1.9619 $\times 10^{-7}$
1.7901 $\times 10^{1}$	2.7887 $\times 10^{-7}$
2.2536 $\times 10^{1}$	3.8954 $\times 10^{-7}$
2.8371 $\times 10^{1}$	5.3438 $\times 10^{-7}$
3.5717 $\times 10^{1}$	7.1943 $\times 10^{-7}$
4.4965 $\times 10^{1}$	9.5005 $\times 10^{-7}$
5.6607 $\times 10^{1}$	1.2302 $\times 10^{-6}$
7.1264 $\times 10^{1}$	1.5616 $\times 10^{-6}$
8.9716 $\times 10^{1}$	1.9433 $\times 10^{-6}$
1.1295 $\times 10^{2}$	2.3713 $\times 10^{-6}$
1.4219 $\times 10^{2}$	2.8385 $\times 10^{-6}$
1.7901 $\times 10^{2}$	3.3351 $\times 10^{-6}$
2.2536 $\times 10^{2}$	3.8484 $\times 10^{-6}$
2.8371 $\times 10^{2}$	4.3630 $\times 10^{-6}$
3.5717 $\times 10^{2}$	4.8595 $\times 10^{-6}$
4.4965 $\times 10^{2}$	5.3127 $\times 10^{-6}$
5.6607 $\times 10^{2}$	5.6894 $\times 10^{-6}$
7.1264 $\times 10^{2}$	5.9485 $\times 10^{-6}$
8.9716 $\times 10^{2}$	6.0453 $\times 10^{-6}$
1.1295 $\times 10^{3}$	5.9430 $\times 10^{-6}$
1.4219 $\times 10^{3}$	5.6263 $\times 10^{-6}$
1.7901 $\times 10^{3}$	5.1128 $\times 10^{-6}$
2.2536 $\times 10^{3}$	4.4521 $\times 10^{-6}$
2.8371 $\times 10^{3}$	3.7135 $\times 10^{-6}$
3.5717 $\times 10^{3}$	2.9682 $\times 10^{-6}$
4.4965 $\times 10^{3}$	2.2753 $\times 10^{-6}$
5.6607 $\times 10^{3}$	1.6743 $\times 10^{-6}$
7.1264 $\times 10^{3}$	1.1844 $\times 10^{-6}$
8.9716 $\times 10^{3}$	8.0692 $\times 10^{-7}$
1.1295 $\times 10^{4}$	5.3076 $\times 10^{-7}$
1.4219 $\times 10^{4}$	3.3803 $\times 10^{-7}$
1.7901 $\times 10^{4}$	2.0912 $\times 10^{-7}$
2.2536 $\times 10^{4}$	1.2608 $\times 10^{-7}$
2.8371 $\times 10^{4}$	7.4332 $\times 10^{-8}$
3.5717 $\times 10^{4}$	4.2987 $\times 10^{-8}$
4.4965 $\times 10^{4}$	2.4457 $\times 10^{-8}$
5.6607 $\times 10^{4}$	1.3725 $\times 10^{-8}$
7.1264 $\times 10^{4}$	7.6154 $\times 10^{-9}$
8.9716 $\times 10^{4}$	4.1860 $\times 10^{-9}$
1.1295 $\times 10^{5}$	2.2833 $\times 10^{-9}$
1.4219 $\times 10^{5}$	1.2377 $\times 10^{-9}$
1.7901 $\times 10^{5}$	6.6757 $\times 10^{-10}$
2.2536 $\times 10^{5}$	3.5858 $\times 10^{-10}$
2.8371 $\times 10^{5}$	1.9198 $\times 10^{-10}$
3.5717 $\times 10^{5}$	1.0251 $\times 10^{-10}$
4.4965 $\times 10^{5}$	5.4622 $\times 10^{-11}$
5.6607 $\times 10^{5}$	2.9056 $\times 10^{-11}$
7.1264 $\times 10^{5}$	1.5436 $\times 10^{-11}$
8.9716 $\times 10^{5}$	8.1911 $\times 10^{-12}$

Table A.3: α-like GCR input fluxes as function of the kinetic energy, on solar activity minimum.

Energy (MeV)	part/cm^2/MeV/sr/s
1.1295 $\times 10^{1}$	7.0913 $\times 10^{-9}$
1.4219 $\times 10^{1}$	1.1173 $\times 10^{-8}$
1.7901 $\times 10^{1}$	1.7424 $\times 10^{-8}$
2.2536 $\times 10^{1}$	2.6873 $\times 10^{-8}$
2.8371 $\times 10^{1}$	4.0952 $\times 10^{-8}$
3.5717 $\times 10^{1}$	6.1612 $\times 10^{-8}$
4.4965 $\times 10^{1}$	9.1429 $\times 10^{-8}$
5.6607 $\times 10^{1}$	1.3369 $\times 10^{-7}$
7.1264 $\times 10^{1}$	1.9243 $\times 10^{-7}$
8.9716 $\times 10^{1}$	2.7235 $\times 10^{-7}$
1.1295 $\times 10^{2}$	3.7854 $\times 10^{-7}$
1.4219 $\times 10^{2}$	5.1598 $\times 10^{-7}$
1.7901 $\times 10^{2}$	6.8871 $\times 10^{-7}$
2.2536 $\times 10^{2}$	8.9857 $\times 10^{-7}$
2.8371 $\times 10^{2}$	1.1437 $\times 10^{-6}$
3.5717 $\times 10^{2}$	1.4168 $\times 10^{-6}$
4.4965 $\times 10^{2}$	1.7042 $\times 10^{-6}$
5.6607 $\times 10^{2}$	1.9852 $\times 10^{-6}$
7.1264 $\times 10^{2}$	2.2340 $\times 10^{-6}$
8.9716 $\times 10^{2}$	2.4230 $\times 10^{-6}$
1.1295 $\times 10^{3}$	2.5286 $\times 10^{-6}$
1.4219 $\times 10^{3}$	2.5357 $\times 10^{-6}$
1.7901 $\times 10^{3}$	2.4420 $\times 10^{-6}$
2.2536 $\times 10^{3}$	2.2576 $\times 10^{-6}$
2.8371 $\times 10^{3}$	2.0033 $\times 10^{-6}$
3.5717 $\times 10^{3}$	1.7055 $\times 10^{-6}$
4.4965 $\times 10^{3}$	1.3923 $\times 10^{-6}$
5.6607 $\times 10^{3}$	1.0893 $\times 10^{-6}$
7.1264 $\times 10^{3}$	8.1670 $\times 10^{-7}$
8.9716 $\times 10^{3}$	5.8715 $\times 10^{-7}$
1.1295 $\times 10^{4}$	4.0545 $\times 10^{-7}$
1.4219 $\times 10^{4}$	2.6961 $\times 10^{-7}$
1.7901 $\times 10^{4}$	1.7321 $\times 10^{-7}$
2.2536 $\times 10^{4}$	1.0788 $\times 10^{-7}$
2.8371 $\times 10^{4}$	6.5393 $\times 10^{-8}$
3.5717 $\times 10^{4}$	3.8713 $\times 10^{-8}$
4.4965 $\times 10^{4}$	2.2460 $\times 10^{-8}$
5.6607 $\times 10^{4}$	1.2810 $\times 10^{-8}$
7.1264 $\times 10^{4}$	7.2031 $\times 10^{-9}$
8.9716 $\times 10^{4}$	4.0026 $\times 10^{-9}$
1.1295 $\times 10^{5}$	2.2027 $\times 10^{-9}$
1.4219 $\times 10^{5}$	1.2026 $\times 10^{-9}$
1.7901 $\times 10^{5}$	6.5237 $\times 10^{-10}$
2.2536 $\times 10^{5}$	3.5204 $\times 10^{-10}$
2.8371 $\times 10^{5}$	1.8918 $\times 10^{-10}$
3.5717 $\times 10^{5}$	1.0132 $\times 10^{-10}$
4.4965 $\times 10^{5}$	5.4116 $\times 10^{-11}$
5.6607 $\times 10^{5}$	2.8842 $\times 10^{-11}$
7.1264 $\times 10^{5}$	1.5345 $\times 10^{-11}$
8.9716 $\times 10^{5}$	8.1528 $\times 10^{-12}$

Table A.4: α-like GCR input fluxes as function of the kinetic energy, on solar activity maximum.

A.1.2 SEP

Table A.5: SEP input fluxes as function of the kinetic energy.

Energy (MeV)	part/cm^2/MeV/sr/s
1.1295×10^{1}	1.3778×10^{2}
1.4219×10^{1}	5.4667×10^{1}
1.7901×10^{1}	2.2622×10^{1}
2.2536×10^{1}	9.7778
2.8371×10^{1}	4.3733
3.5717×10^{1}	2.0089
4.4965×10^{1}	9.4222×10^{-1}
5.6607×10^{1}	4.4889×10^{-1}
7.1264×10^{1}	2.1511×10^{-1}
8.9716×10^{1}	1.0400×10^{-1}
1.1295×10^{2}	5.0222×10^{-2}
1.4219×10^{2}	2.4533×10^{-2}
1.7901×10^{2}	1.1956×10^{-2}
2.2536×10^{2}	5.8222×10^{-3}
2.8371×10^{2}	2.8533×10^{-3}
3.5717×10^{2}	1.3956×10^{-3}
4.4965×10^{2}	6.8000×10^{-4}
5.6607×10^{2}	3.3378×10^{-4}
7.1264×10^{2}	1.6311×10^{-4}
8.9716×10^{2}	0
1.1295×10^{3}	0
1.4219×10^{3}	0
1.7901×10^{3}	0
2.2536×10^{3}	0
2.8371×10^{3}	0
3.5717×10^{3}	0
4.4965×10^{3}	0
5.6607×10^{3}	0
7.1264×10^{3}	0
8.9716×10^{3}	0
1.1295×10^{4}	0
1.4219×10^{4}	0
1.7901×10^{4}	0
2.2536×10^{4}	0
2.8371×10^{4}	0
3.5717×10^{4}	0
4.4965×10^{4}	0
5.6607×10^{4}	0
7.1264×10^{4}	0
8.9716×10^{4}	0
1.1295×10^{5}	0
1.4219×10^{5}	0
1.7901×10^{5}	0
2.2536×10^{5}	0
2.8371×10^{5}	0
3.5717×10^{5}	0
4.4965×10^{5}	0
5.6607×10^{5}	0
7.1264×10^{5}	0
8.9716×10^{5}	0

A.2 proton-like GCR

A.2.1 Primary particles

Depth	Solar minimum	Solar maximum
Surface	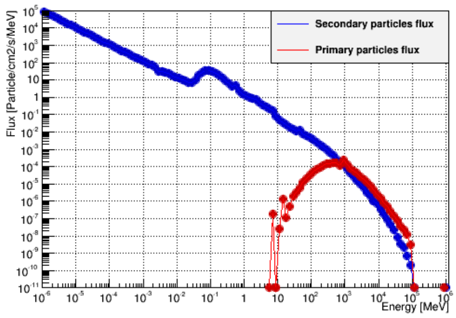	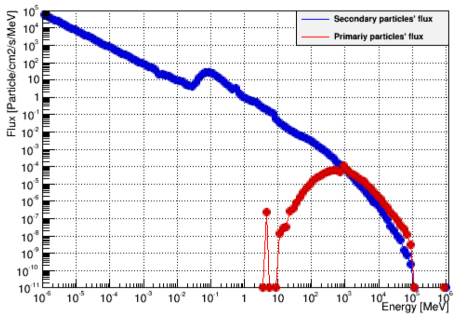
10 cm	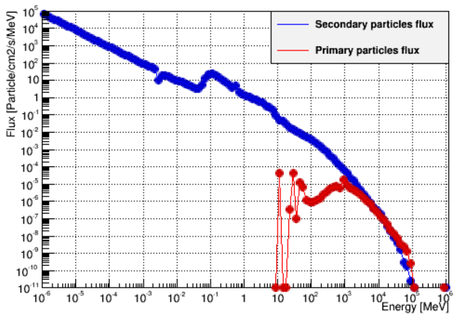	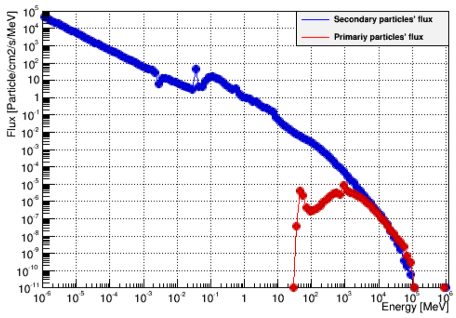
20 cm	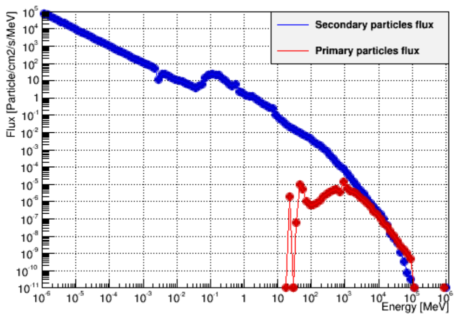	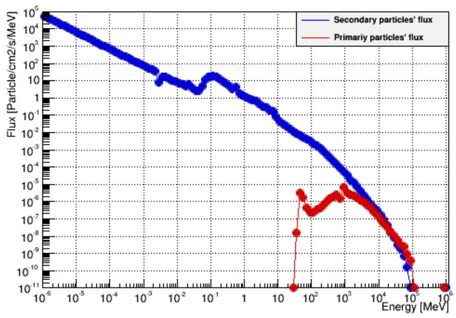
30 cm	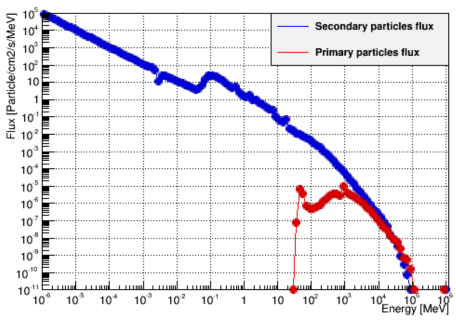	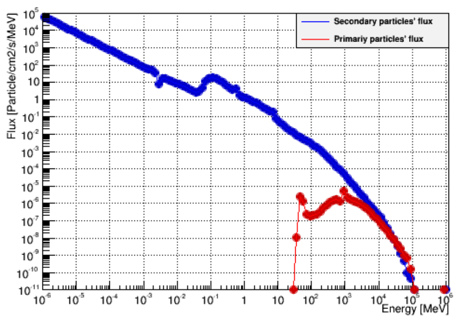

Figure A.1: Proton-like GCR primary and secondary particle fluxes at different depths on solar activity minimum and maximum.

Depth	Solar minimum	Solar maximum
40 cm	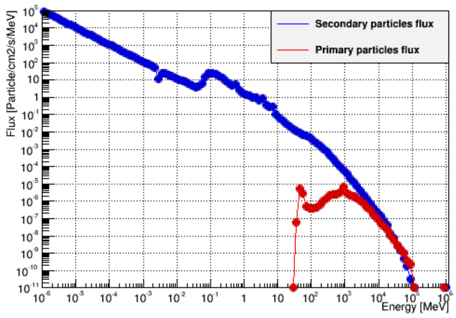	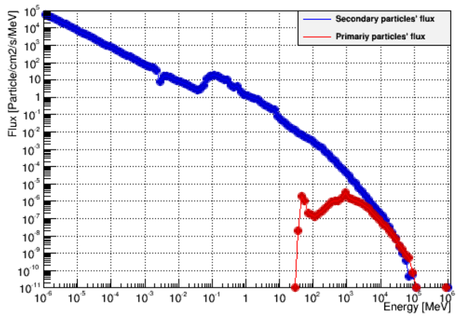
50 cm	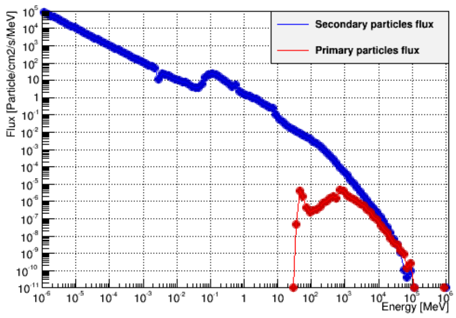	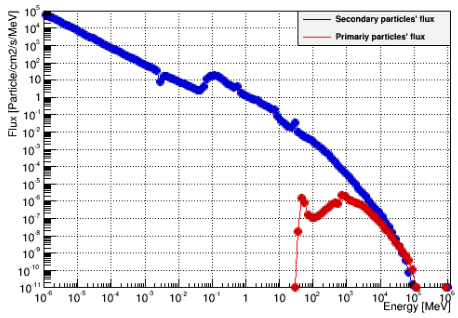
75 cm	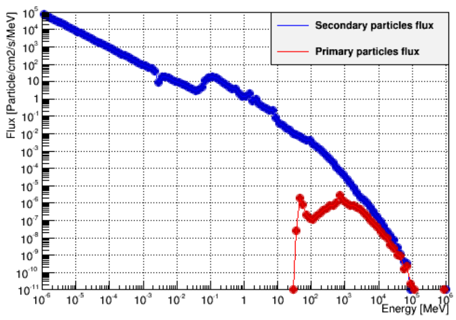	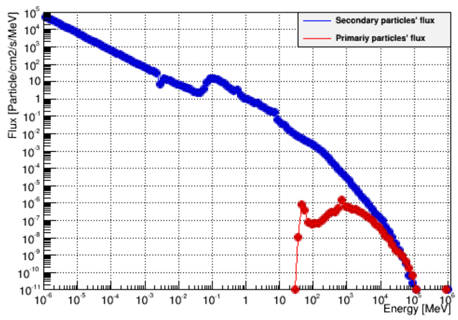
100 cm	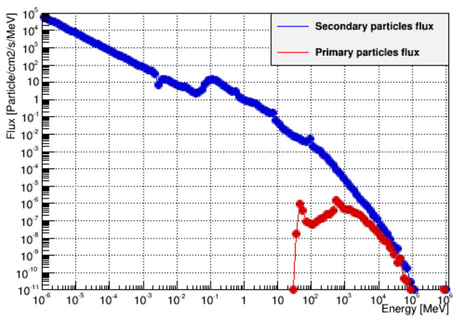	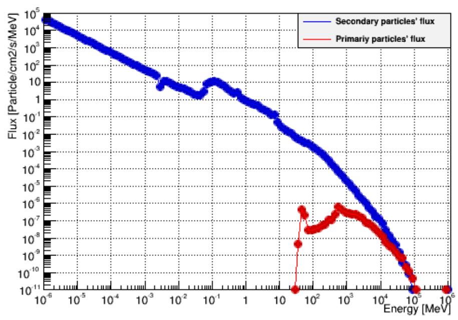

Figure A.2: Proton-like GCR primary and secondary particle fluxes at different depths on solar activity minimum and maximum.

Depth	Solar minimum	Solar maximum
150 cm	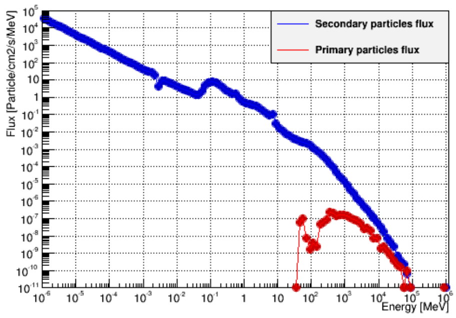	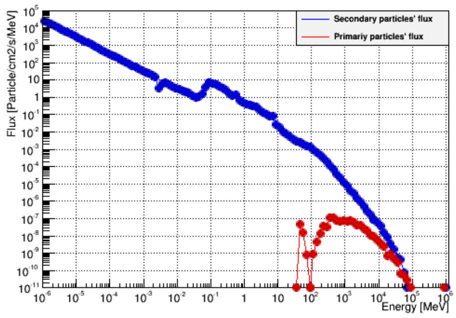
200 cm	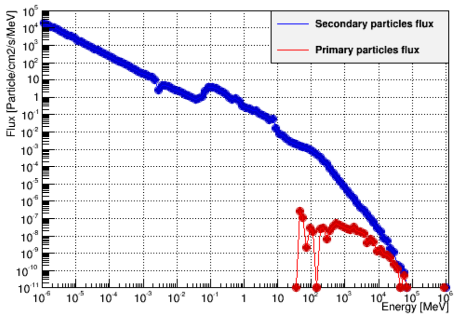	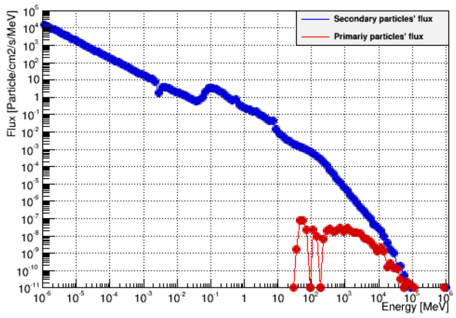
250 cm	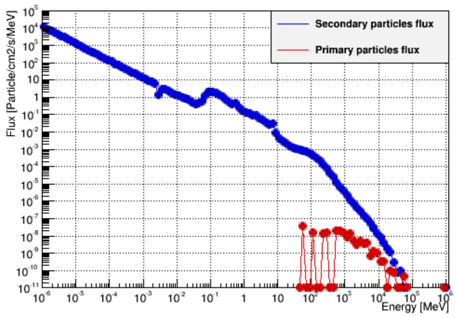	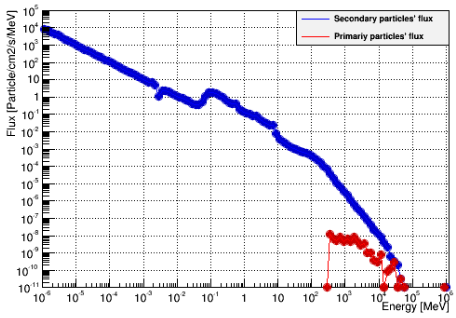
300 cm	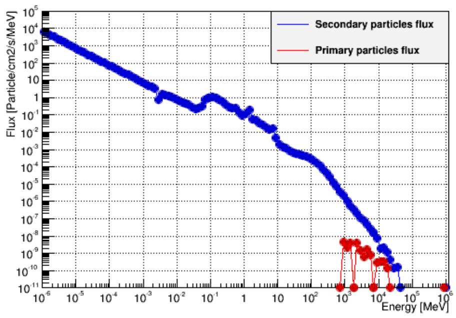	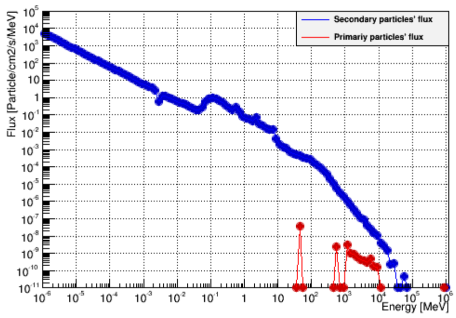

Figure A.3: Proton-like GCR primary and secondary particle fluxes at different depths on solar activity minimum and maximum.

A.2.2 All particles

Depth	Solar minimum	Solar maximum
Surface	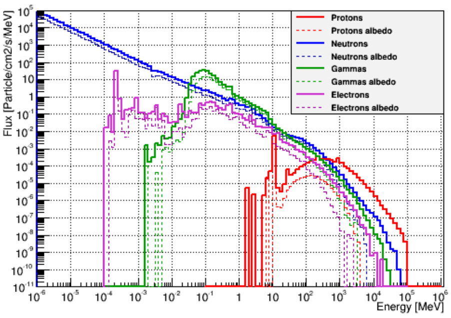	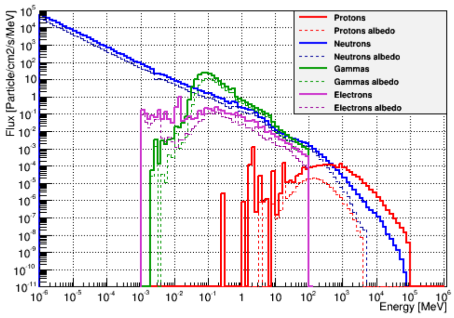
10 cm	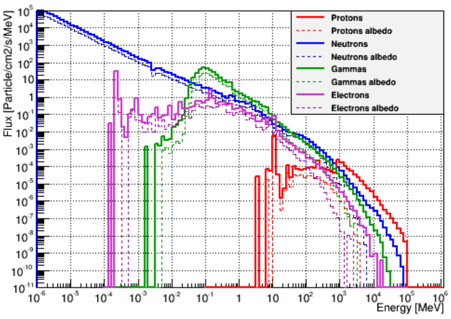	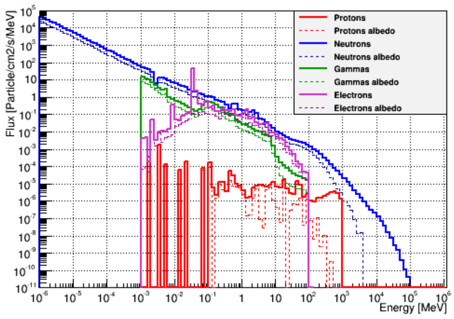
20 cm	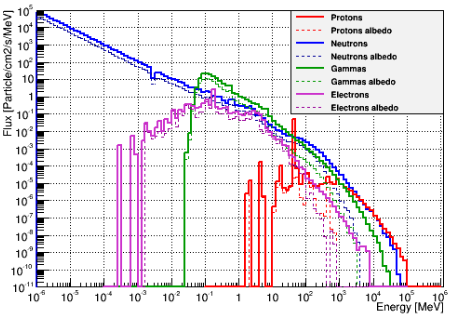	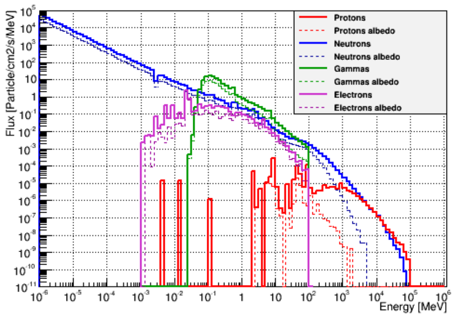
30 cm	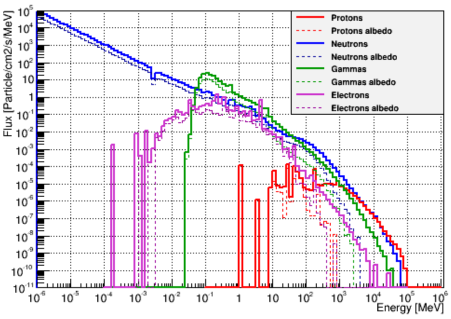	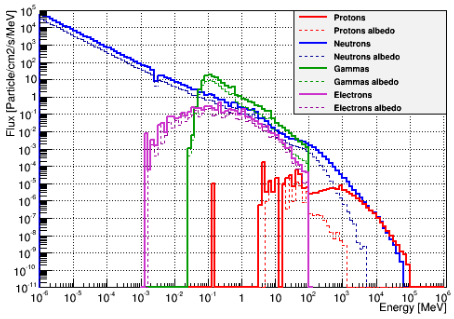

Figure A.4: A detailed view over all particle fluxes on solar activity minimum and maximum at different depths for and input of proton GCR particles.

Depth	Solar minimum	Solar maximum
40 cm	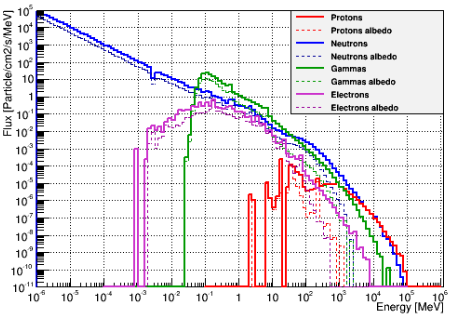	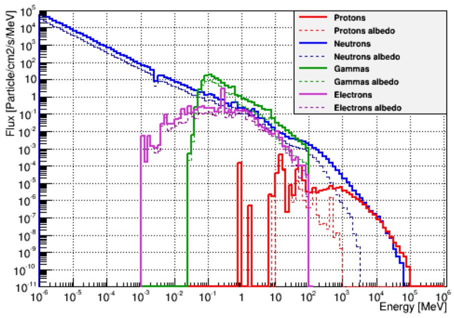
50 cm	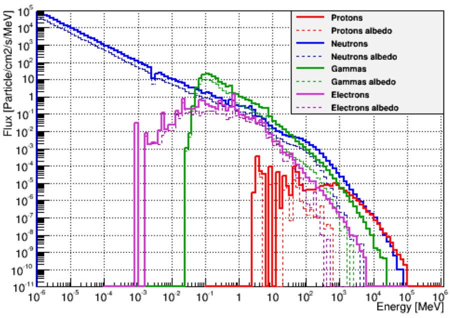	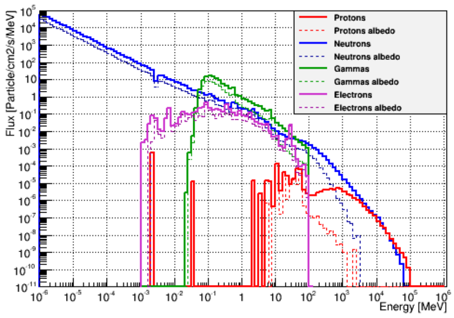
75 cm	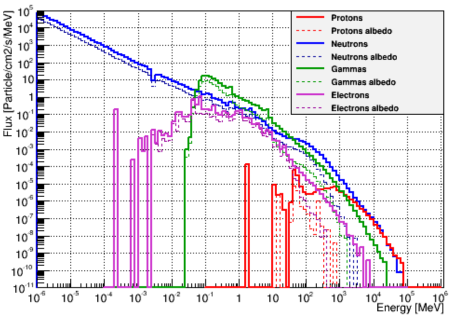	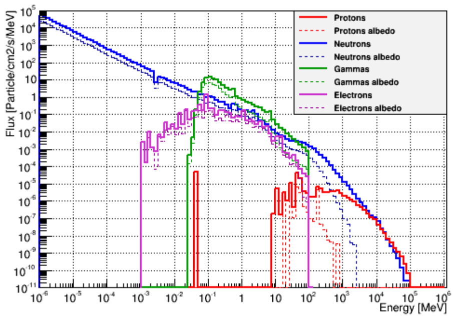
100 cm	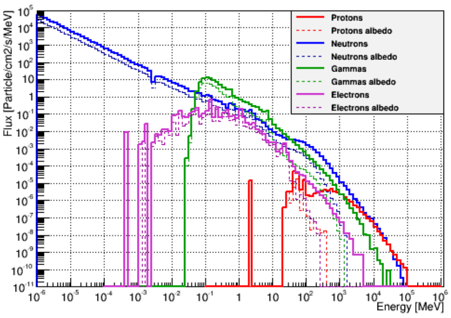	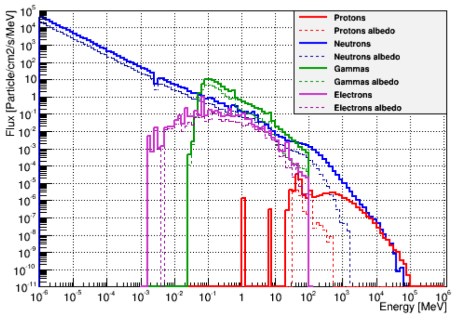

Figure A.5: A detailed view over all particle fluxes on solar activity minimum and maximum at different depths for and input of proton GCR particles.

Depth	Solar minimum	Solar maximum

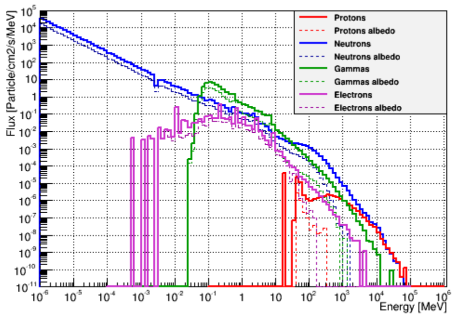

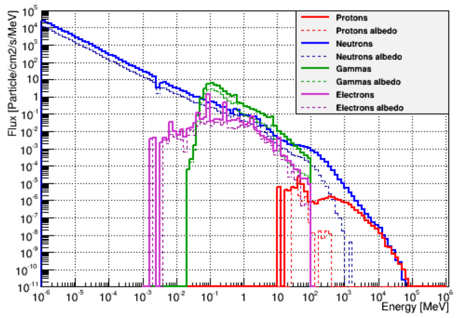

150 cm

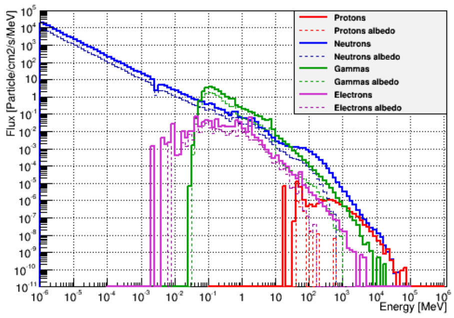

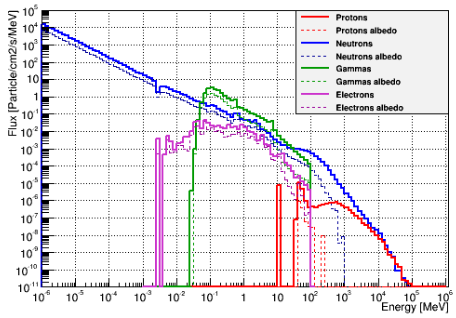

200 cm

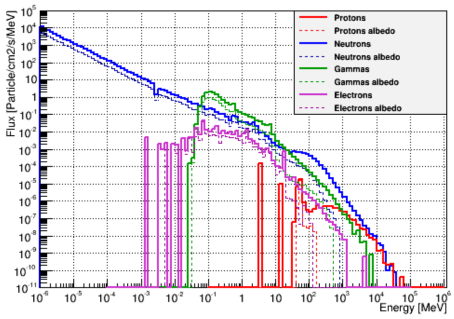

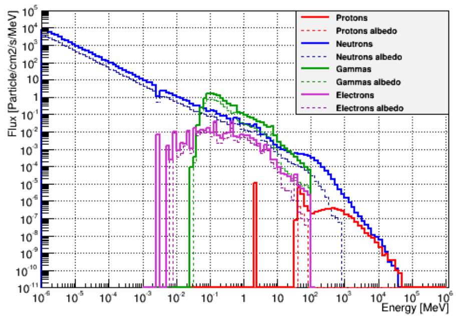

250 cm

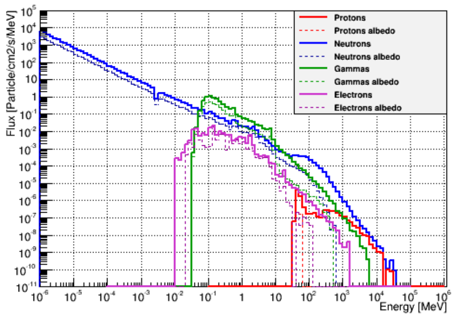

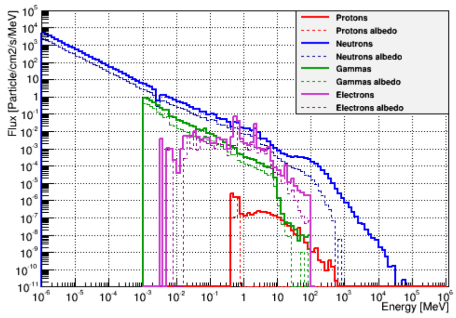

300 cm

Figure A.6: A detailed view over all particle fluxes on solar activity minimum and maximum at different depths for and input of proton GCR particles.

A.2.3 Alpha particles

Primary particles

Depth	Solar minimum	Solar maximum
Surface	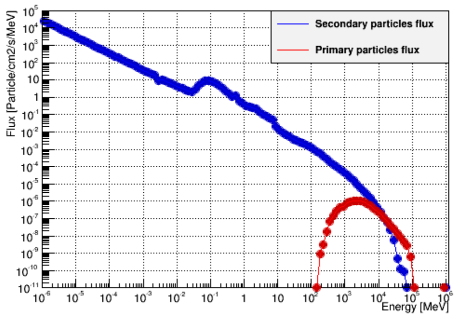	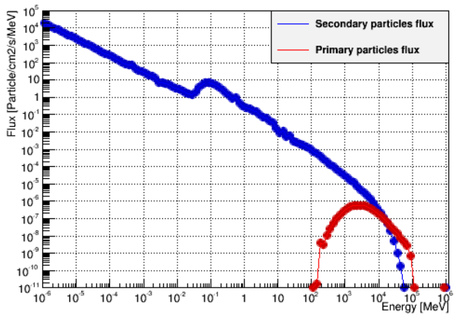
10 cm	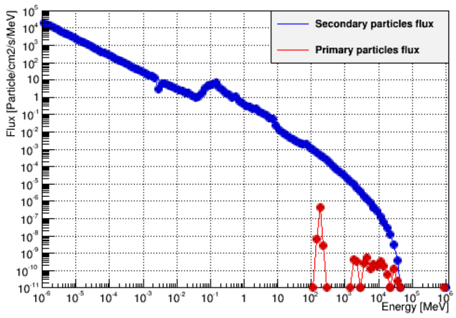	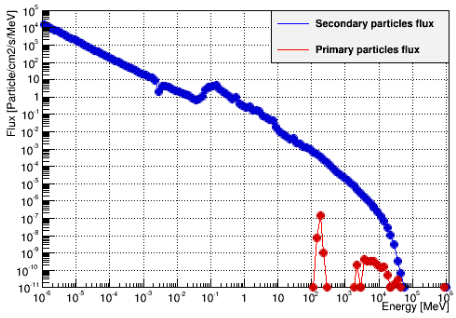
20 cm	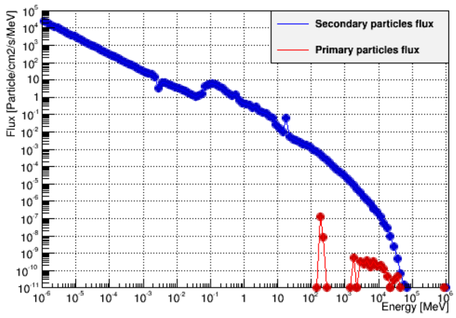	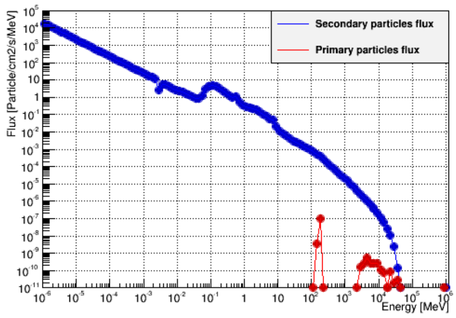
30 cm	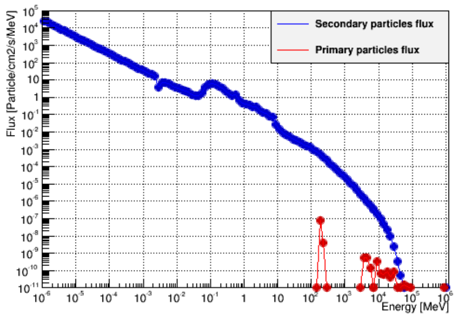	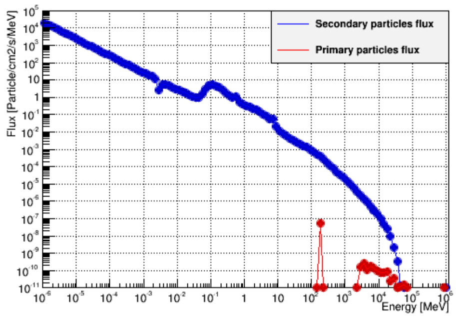

Figure A.7: Primary and secondary particle fluxes at different depths on solar activity minimum and maximum for and input of α-like GCR particles.

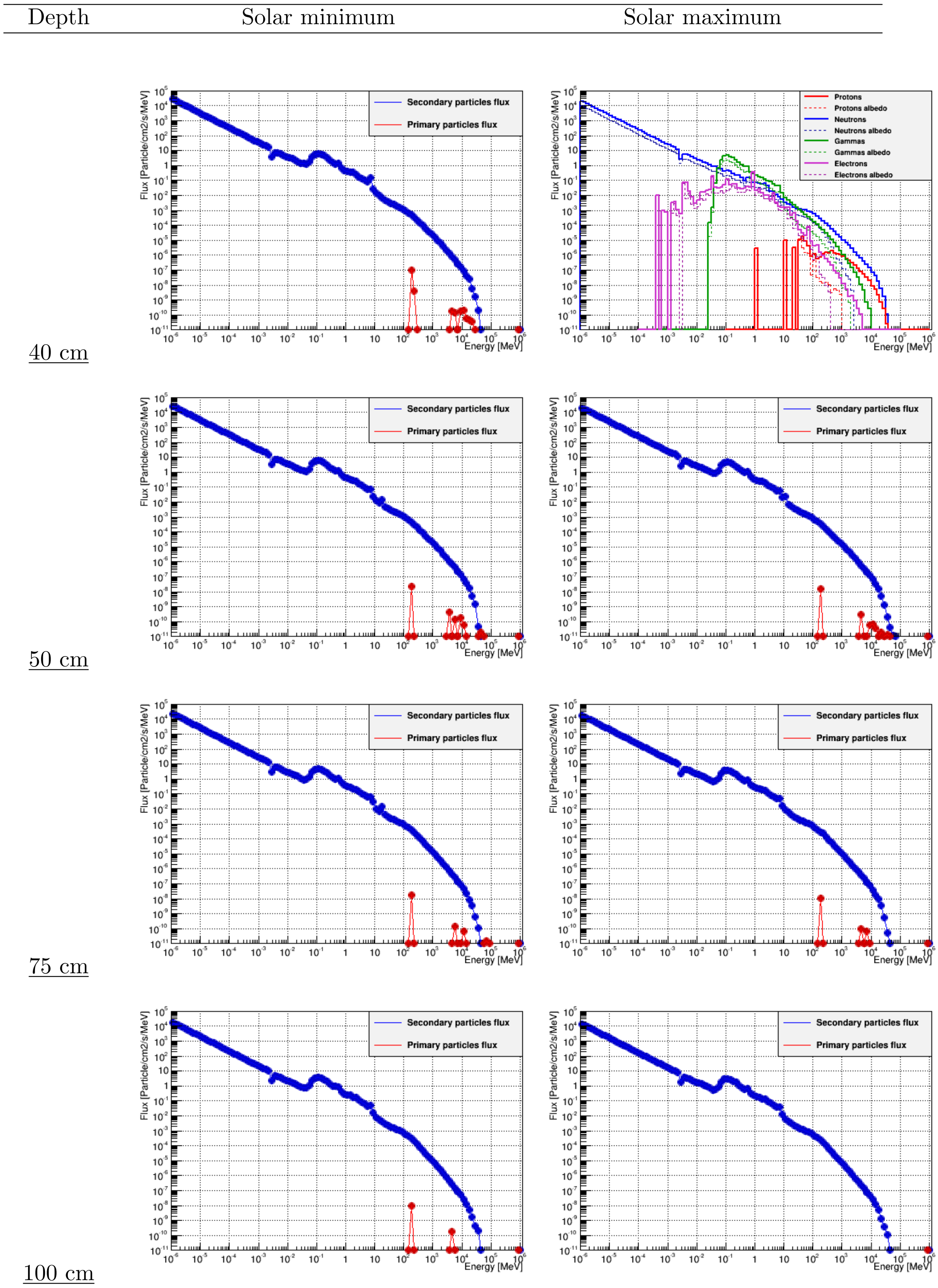

Figure A.8: Primary and secondary particle fluxes at different depths on solar activity minimum and maximum for and input of α-like GCR particles.

Depth	Solar minimum	Solar maximum
150 cm		
200 cm		
250 cm		
300 cm		

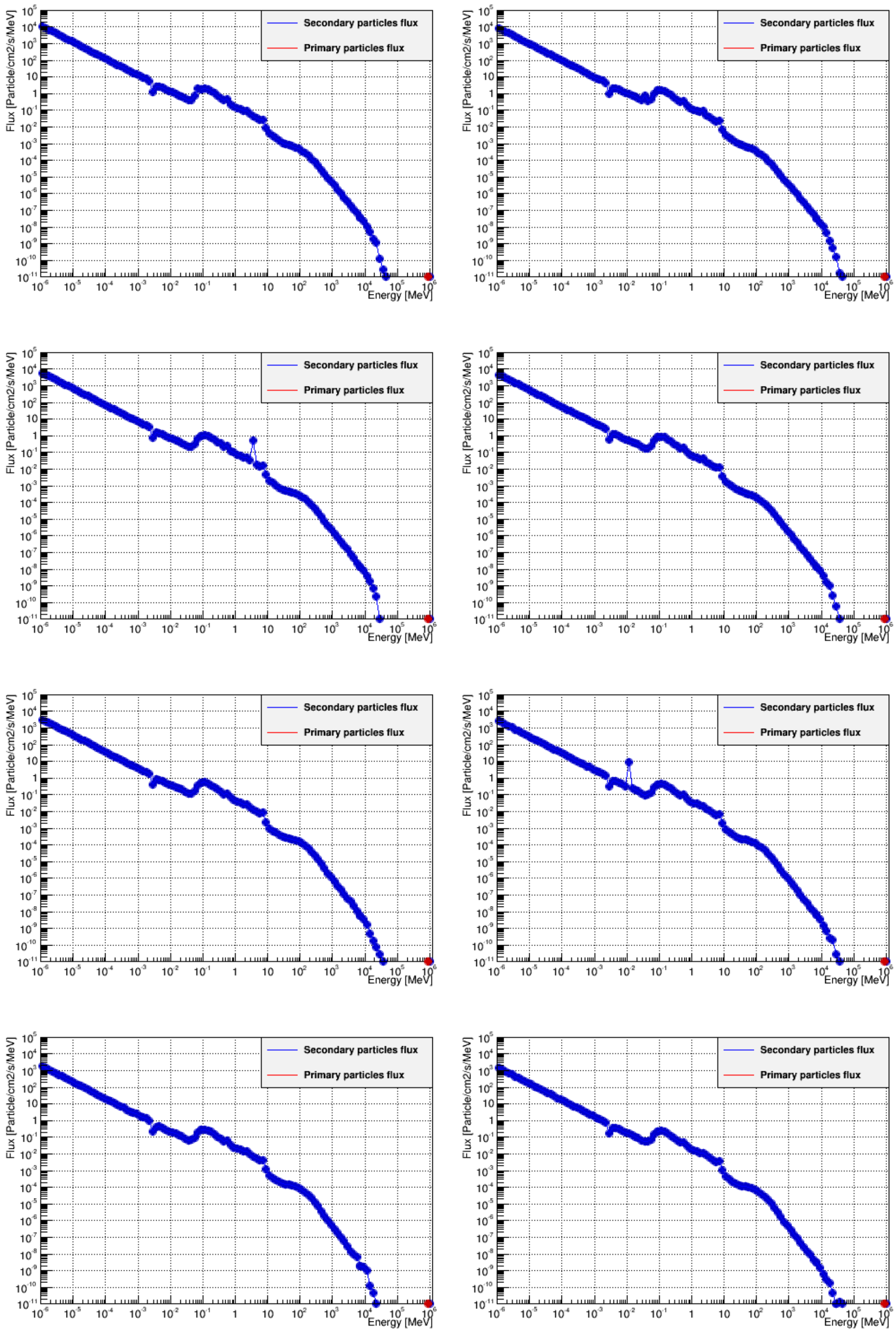

Figure A.9: Primary and secondary particle fluxes at different depths on solar activity minimum and maximum for and input of α-like GCR particles.

A.2.4 All particles

Depth	Solar minimum	Solar maximum

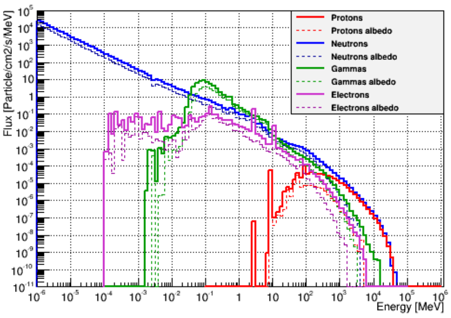

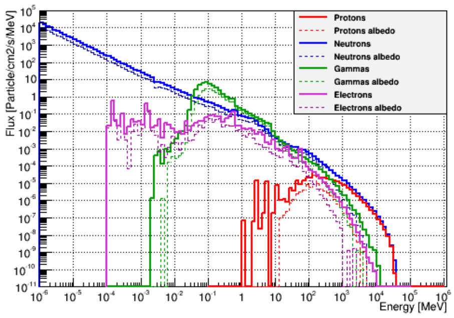

Surface

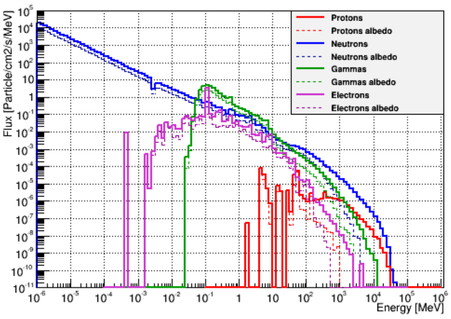

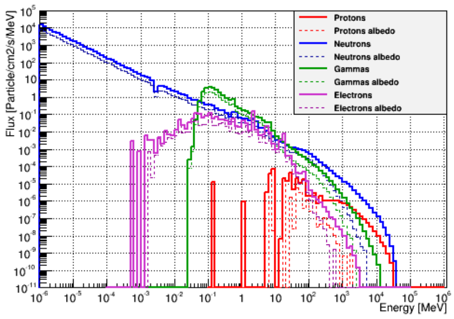

10 cm

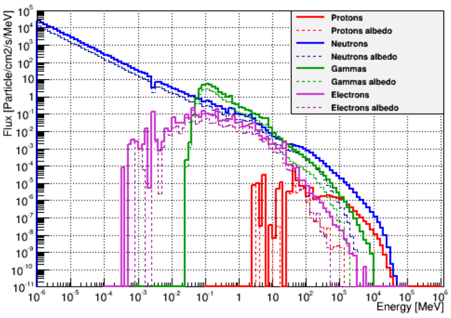

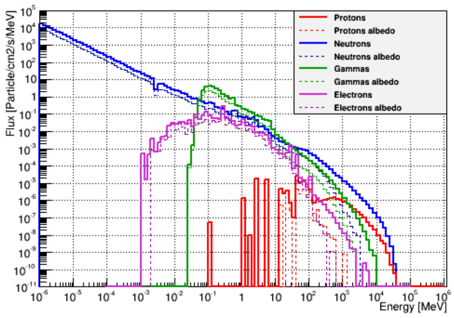

20 cm

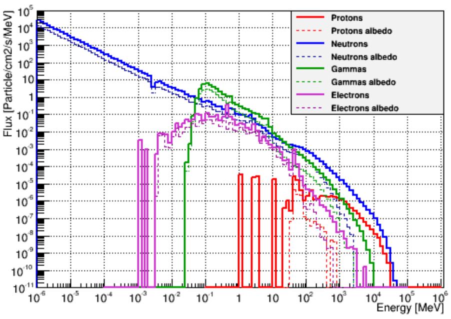

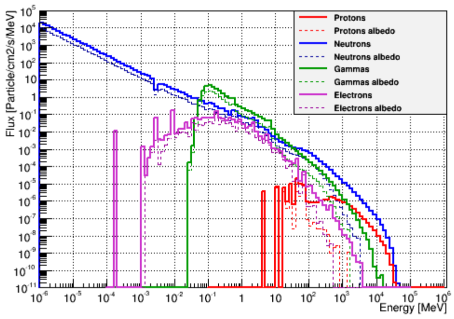

30 cm

Figure A.10: A detailed view over all particle fluxes on solar activity minimum and maximum at different depths for and input of α GCR particles.

Depth	Solar minimum	Solar maximum
40 cm	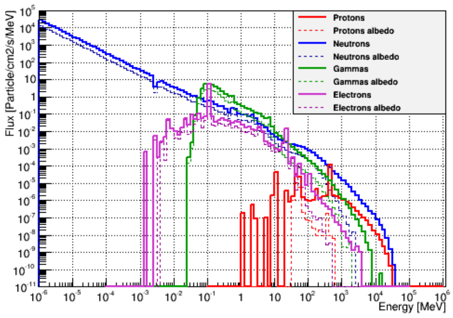	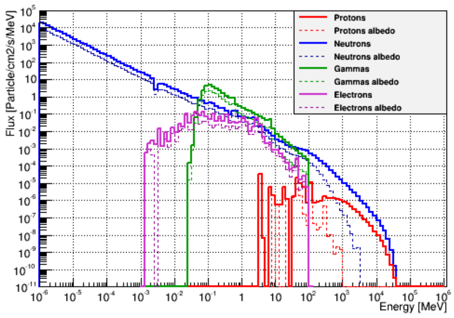
50 cm	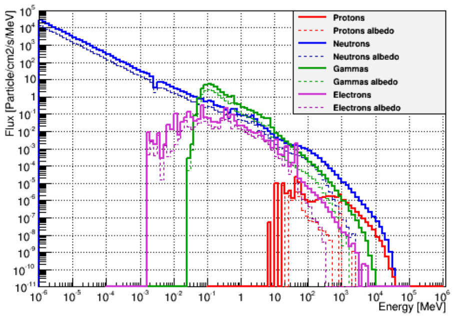	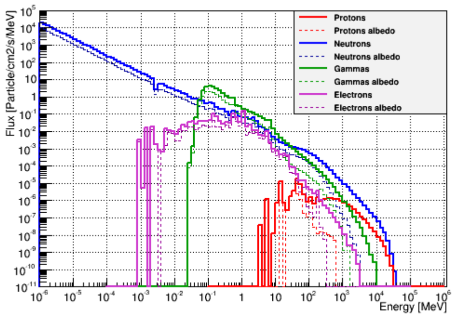
75 cm	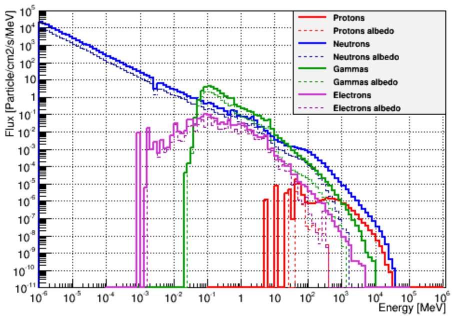	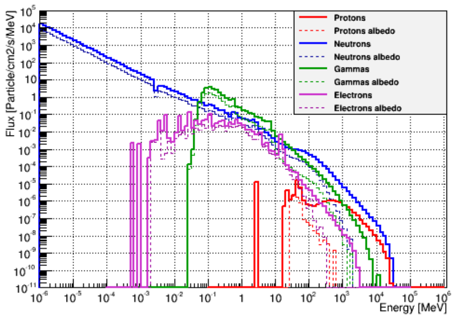
100 cm	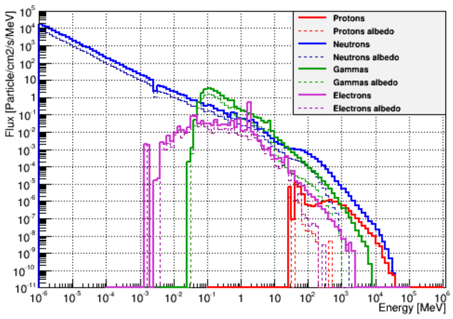	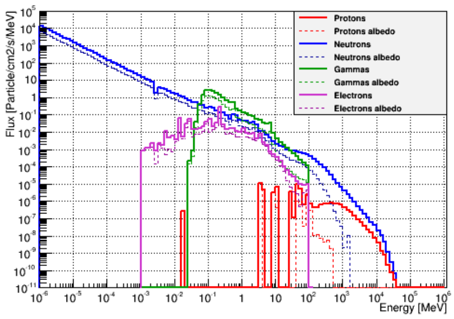

Figure A.11: A detailed view over all particle fluxes on solar activity minimum and maximum at different depths for and input of α GCR particles.

Depth	Solar minimum	Solar maximum
150 cm	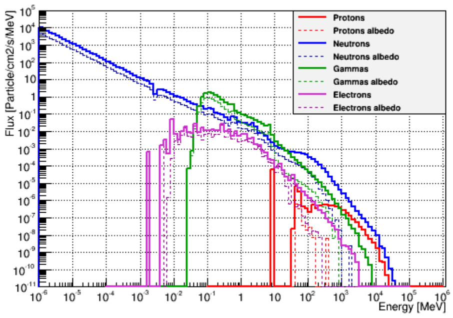	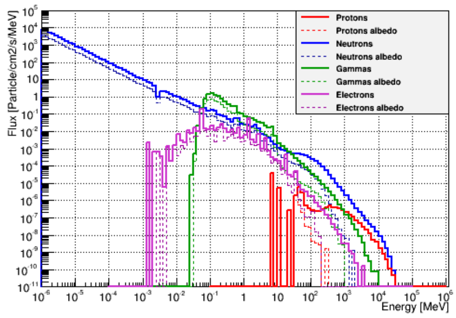
200 cm	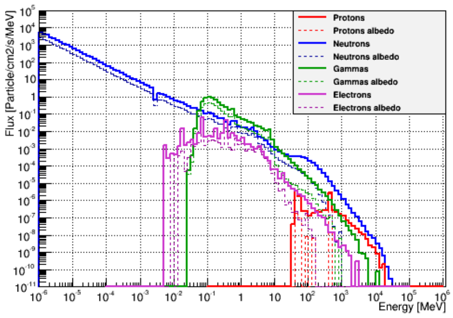	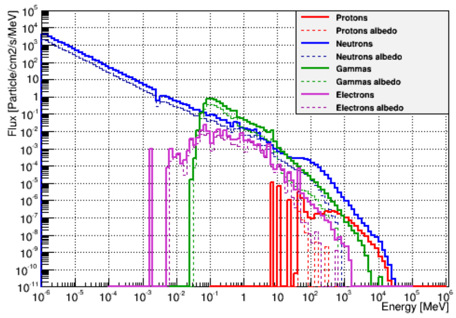
250 cm	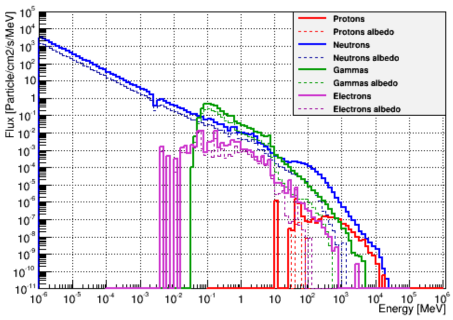	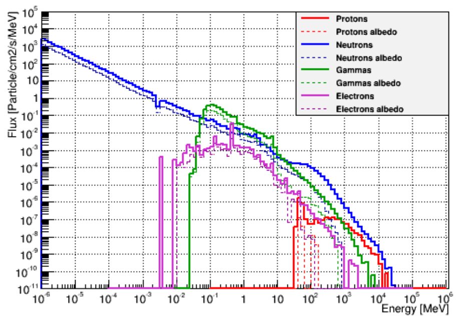
300 cm	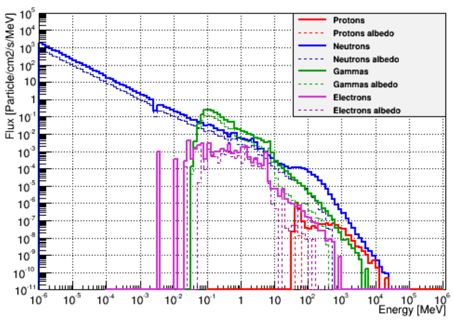	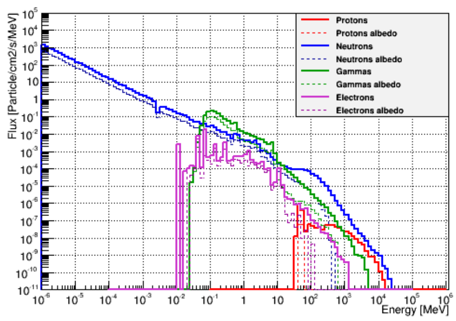

Figure A.12: A detailed view over all particle fluxes on solar activity minimum and maximum at different depths for and input of α GCR particles.

A.3 SEP events

Depth	Solar minimum	Solar maximum
Surface	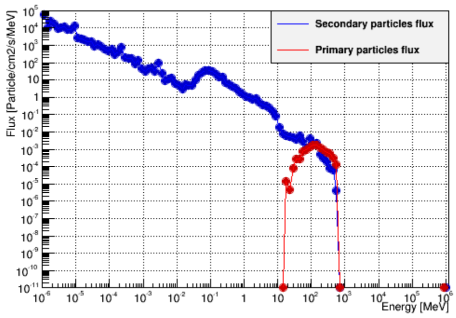	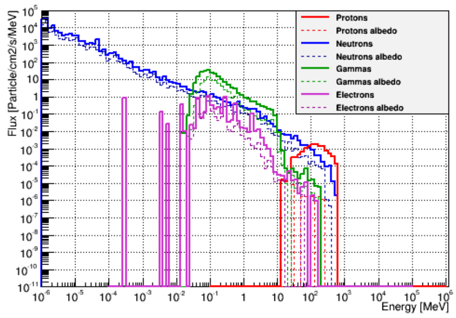
10 cm	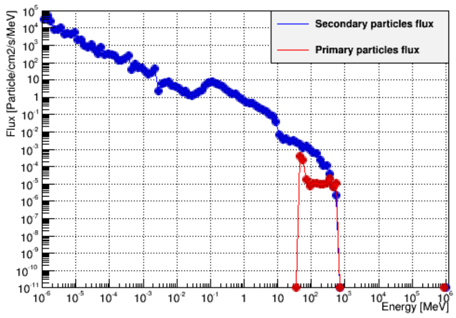	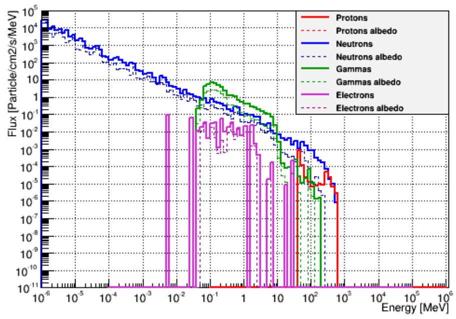
20 cm	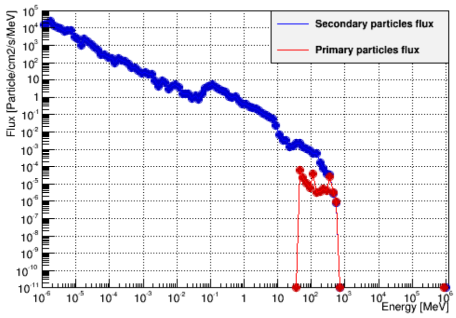	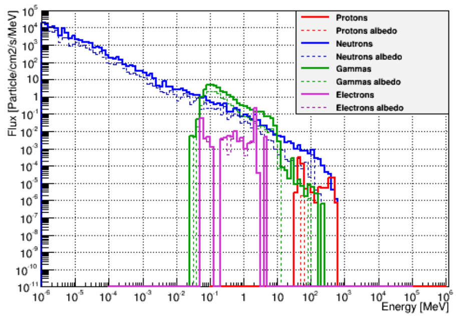
30 cm	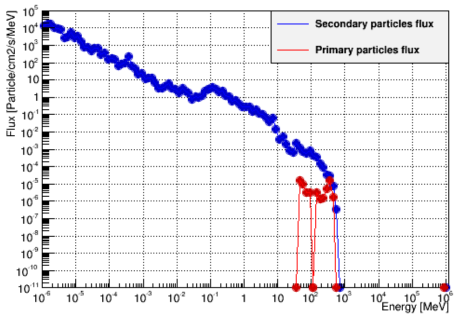	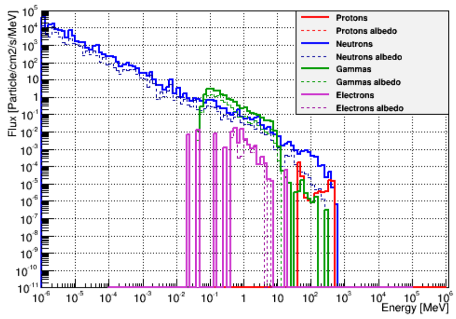

Figure A.13: A detailed view over all particle fluxes on solar activity minimum and maximum at different depths for and input of SEP events.

Depth	Solar minimum	Solar maximum

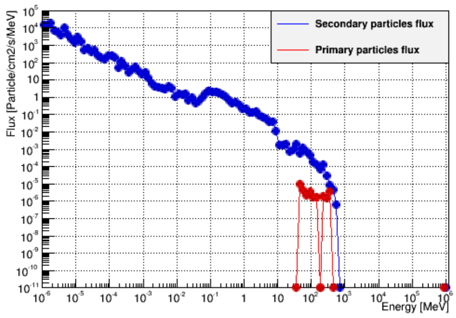

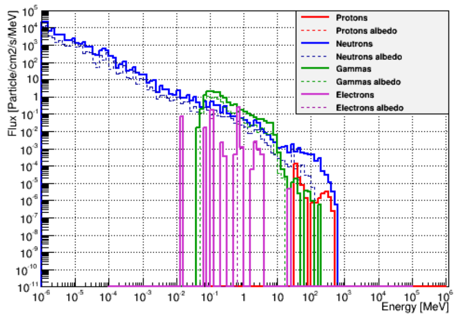

40 cm

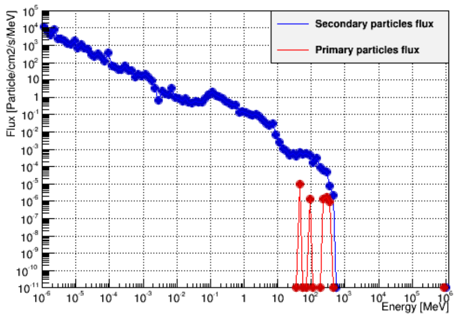

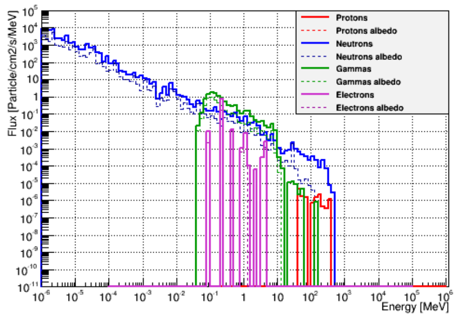

50 cm

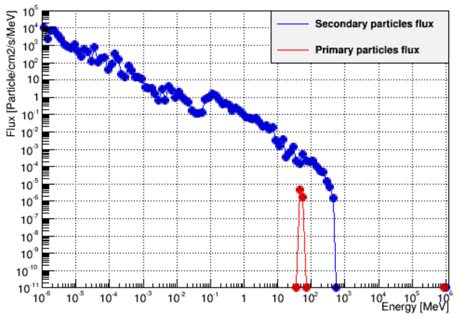

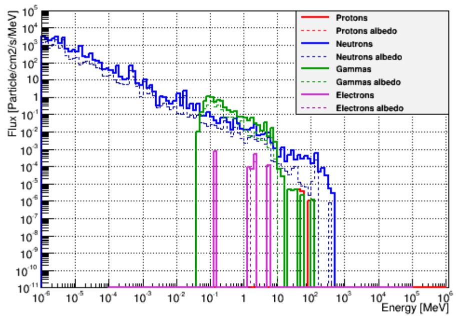

75 cm

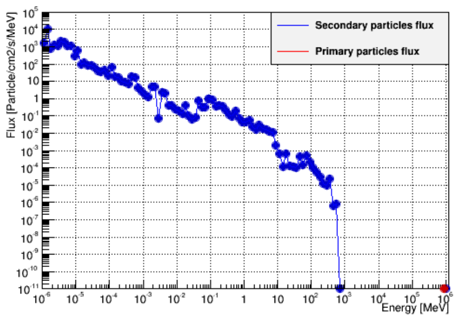

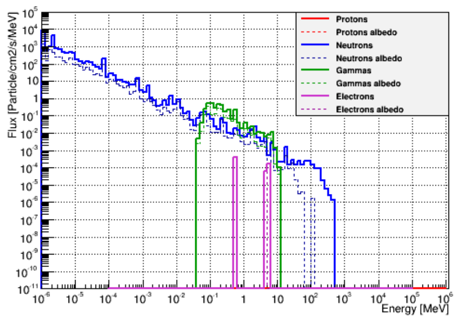

100 cm

Figure A.14: A detailed view over all particle fluxes on solar activity minimum and maximum at different depths for and input of SEP events.

Depth	Solar minimum	Solar maximum

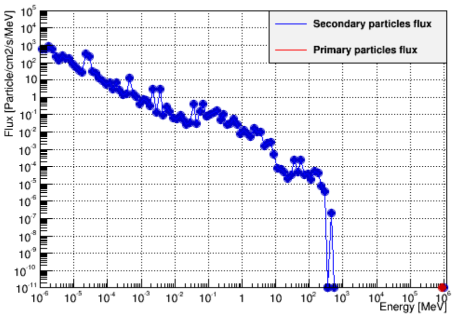

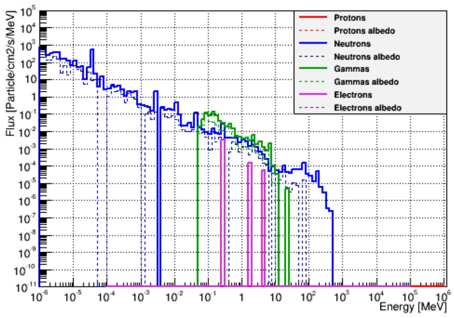

150 cm

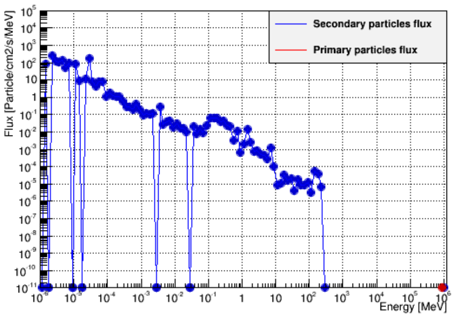

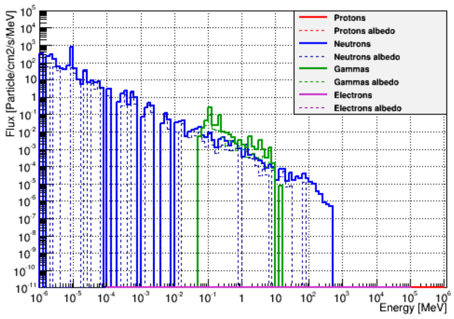

200 cm

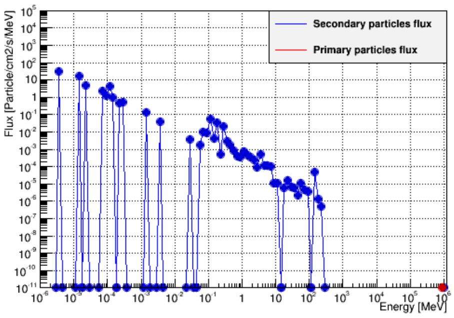

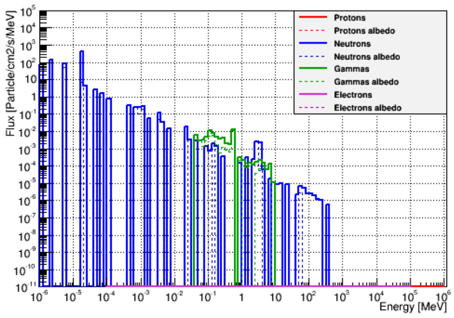

250 cm

Figure A.15: A detailed view over all particle fluxes on solar activity minimum and maximum at different depths for and input of SEP events.

Table A.6: Composition of each atmosphere's layer.

Height(km)	density (gcm^{-3})	Atmospheric temperature (K)	CO (%)	CO_2 (%)	H_2 (%)	H_2O (%)	H_2O_v(%)	N_2 (%)	O_2 (%)
0.01	0.01562	204.1	0.000925	0.9415	0.00002027	0	0.000343	0.03489	0
0.02	0.01549	205.6	0.000925	0.9415	0.00002027	0	0.0003451	0.03489	0
0.05	0.01499	211.9	0.0009249	0.9415	0.00002026	0	0.0003534	0.03488	0
0.12	0.01452	217.4	0.0009241	0.9416	0.00002025	0	0.0003539	0.03486	0
0.25	0.0141	221.2	0.0009228	0.9416	0.00002023	0	0.0003517	0.03482	0
0.5	0.01359	224.6	0.0009216	0.9417	0.00002021	0	0.0003525	0.03478	0
1.0	0.0129	226.8	0.0009225	0.9416	0.00002022	0	0.0003585	0.03481	0
2.0	0.01185	226.5	0.00093	0.9412	0.00002036	0	0.0003665	0.03504	0
3.2	0.01078	224.9	0.0009374	0.9409	0.00002048	0	0.0003696	0.03525	0
5.0	0.009387	221.5	0.0009423	0.9407	0.00002056	0	0.0003725	0.03539	0
7.0	0.00803	216.8	0.000943	0.9406	0.00002057	0	0.0003749	0.0354	0
10.0	0.006343	208.2	0.0009394	0.9408	0.00002051	0	0.0003762	0.03531	0
14.0	0.004583	198.2	0.0009349	0.941	0.00002046	0.000004121	0.0003749	0.0352	0
18.0	0.003262	190.1	0.000931	0.9412	0.00002043	0.0001123	0.0002558	0.03513	0
22.0	0.002257	183.7	0.0009228	0.9416	0.00002033	0.0001359	0.0001578	0.03495	0
27.0	0.001371	177.8	0.0009086	0.9423	0.00002014	0.00008174	0.00008802	0.03458	0
32.0	0.0008065	172.9	0.0008948	0.943	0.00001992	0.00001255	0.00005223	0.03417	0
38.0	0.0004261	166.8	0.0008876	0.9437	0.0000197	0	0.0000146	0.03378	0
44.0	0.0002207	160.4	0.0008895	0.9443	0.00001947	0	0.00000237	0.03342	0.0000006736
50.0	0.0001114	155.2	0.0009105	0.9449	0.00001924	0	0.0000002836	0.03304	0.000006119